UNIVERSIDAD DE CHILE
FACULTAD DE CIENCIAS FÍSICAS Y MATEMÁTICAS
DEPARTAMENTO DE ASTRONOMÍA

GAS-PHASE METALLICITY OF LOCAL ANALOGS OF HIGH-z GALAXIES: A NEW CALIBRATION FOR CHEMICAL ABUNDANCES IN THE DISTANT UNIVERSE

TESIS PARA OPTAR AL GRADO DE
MAGÍSTER EN CIENCIAS, MENCIÓN ASTRONOMÍA

BENJAMÍN ALEXIS NAVARRETE RIVAS

PROFESOR GUÍA:
VALENTINO GONZALEZ CORVALÁN

MIEMBROS DE LA COMISIÓN:
GUILLERMO BLANC MENDIBERRI
RICARDO MUÑOZ VIDAL
FUYAN BIAN

SANTIAGO DE CHILE
2024

METALICIDAD DE LA FASE GASEOSA DE ANÁLOGOS LOCALES DE GALAXIAS A ALTO z: UNA NUEVA CALIBRACIÓN PARA ABUNDANCIAS QUÍMICAS EN EL UNIVERSO DISTANTE

Los estudios del contenido metálico del gas de las galaxias son fundamentales para comprender cómo evolucionan las galaxias a través del tiempo cósmico. La relación entre la metalicidad y las propiedades globales de las galaxias, como la masa estelar y la tasa de formación estelar, proporcionan información valiosa sobre qué procesos regulan el enriquecimiento de las galaxias. Estos estudios han sido extensos en el Universo local, sin embargo, los intentos de aplicar estudios similares a alto z están llenos de dificultades observacionales.

A partir de espectros ópticos de regiones HII locales y nebulosas planetarias, puede estimarse la metalicidad en fase gaseosa utilizando el "método directo". Las fuentes a mayor-z ven sus líneas de emisión más tenues y desplazadas a las bandas infrarrojas, donde la absorción atmosférica dificulta la observación desde tierra. Antes del telescopio espacial James Webb, los estudios de metalicidad tenían que basarse en estimaciones realizadas con unas pocas líneas brillantes detectadas y en relaciones teóricas como las relaciones temperatura-temperatura o calibraciones empíricas de razones entre líneas de emission fuertes. Para estudiar estas relaciones utilizamos análogos locales de galaxias de alto z como laboratorio ideal del Universo temprano.

Los análogos locales de este trabajo se seleccionaron en función de su posición en el diagrama BPT para cumplir las condiciones de ionización del medio interestelar de galaxias a $z \sim 2.3$. Utilizamos espectros de resolución moderada de 18 análogos recogidos con el espectrógrafo Magellan Echelle montado en el telescopio Baade de 6.5 m instalado en el Observatorio Las Campanas. Tras medir y corregir los flujos de las líneas de emisión, utilizamos el método directo para estimar la densidad, temperatura y metalicidad de la fase gaseosa de los análogos locales. Finalmente, investigamos las relaciones de temperatura y las calibraciones de metalicidad dadas por nuestros análogos.

Encontramos que nuestros análogos se desvían a altas metalicidades de la relación teórica $T_e[\text{O II}]$ vs $T_e[\text{O III}]$ ampliamente utilizada, mostrando una pendiente menos pronunciada y una dispersión menor. Presentamos nuevas calibraciones para 12 relaciones de líneas de emisión en el rango $7.8 < 12 + \log(\text{O/H}) < 8.6$. Nuestras relaciones se desvían de las calibraciones basadas en regiones HII locales, otros análogos locales y modelos de fotoionización, sugiriendo posibles subestimaciones de hasta 0.3 dex en el régimen de alta metalicidad. Además, estos resultados concuerdan notablemente con nuevas calibraciones exploradas hasta $z = 9$ que establecen un buen punto de referencia para nuevos estudios de metalicidad en el Universo temprano con el telescopio espacial James Webb.

GAS-PHASE METALLICITY OF LOCAL ANALOGS OF HIGH-z GALAXIES: A NEW CALIBRATION FOR CHEMICAL ABUNDANCES IN THE DISTANT UNIVERSE

Studies of the metal content of the gas in galaxies are fundamental to understand how galaxies evolve through cosmic time. The relation between metallicity and global properties of galaxies such as the stellar mass and star formation rate provide valuable insights into what processes regulate the enrichment of galaxies. These studies have been extensive in the local Universe, however, attempts of applying similar studies at high-z are full of observational difficulties.

From optical spectra of local HII regions and planetary nebulae, the gas-phase metallicity can be estimated using the "direct method". Sources at higher-z see their emission lines dimmer and shifted to the infrared bands where the atmospheric absorption difficult the observation from the ground. Before the James Webb Space Telescope, studies of metallicity had to rely on estimations made with a few detected bright lines and theoretical relations such as the temperature-temperature relations or empirical calibrations of strong emission line ratios. To study these relations we used local analogs of high-z galaxies as an ideal laboratory of the early Universe.

Local analogs in this work were selected based on their position in the BPT diagram to meet the ionization conditions of the ISM of galaxies at $z \sim 2.3$. We used moderate resolution spectra of 18 analogs gathered with the Magellan Echelle Spectrograph mounted on the ground-based 6.5m Baade telescope at Las Campanas Observatory. After measurement and correction of the emission line fluxes, we used the direct method to estimate the density, temperature, and metallicity of the gas-phase of the local analogs. Finally, we investigate the temperature relations and calibrations of metallicity given by our analogs.

We found that our analogs deviate at high metallicities from the widely used theoretical T_e[O II] vs T_e[O III] relation, showing a shallower slope and a lower scatter. We present new calibrations for 12 emission line ratios in the range $7.8 < 12 + \log(\mathrm{O/H}) < 8.6$. Our relations deviate from calibrations based on local HII regions, other local analogs, and photoionization models, suggesting possible underestimations up to 0.3 dex in the high-metallicity regime. Furthermore, these results remarkably agree with new calibrations explored up to $z = 9$ which set a good benchmark for new metallicity studies in the early Universe with the James Webb Space Telescope.

Para todos los miembros de mi familia.
Mis padres, hermanos y mascotas:
Nini, Cacique, Mao, Peluche, Pirata y Kira.

Agradecimientos

Me gustaría comenzar agradeciendo a los académicos miembros del comité: Guillermo Blanc, Fuyan Bian, y Ricardo Muñoz, que con sus comentarios me ayudaron a aprender más sobre mi propio tema de estudio e hicieron posible mi defensa. Agradecimientos especiales al profesor Valentino González, quien fue mi supervisor durante el magíster y el mayor responsable de mi crecimiento académico. Fue quien más me ayudó a avanzar en mi camino a convertirme un astrónomo profesional. Le agradezco sus años de experiencia y consejos que me dieron las herramientas para constituir mi perfil académico. Por último, quisiera agradecer a profesores que tuvieron un impacto en mi desarrollo profesional como lo fueron el profesor Luis Campusano y Walter Max-Moerbeck que siempre me apoyaron y velaron por el bien de mi paso por la carrera.

Agradecimientos a mi familia que fue una parte importante en este proceso. Gracias a mi madre María Rivas, quien desde el primer día siempre dió todo su apoyo para asegurar mi éxito académico. A mi padre, Daniel Navarrete, quien me entrega todos sus años de cariño y apoyo incluso estando lejos de nosotros. Gracias a mis hermanos Constanza, Jesús y Joaquín Navarrete, quienes siempre me animaron y me hicieron sentir que no estaba solo en ninguna etapa de la vida.

Quisiera agradecer a todos mis queridos amigos, especialmente a Edgardo, Gabriel, Juan Pablo, Silvio, Boris y Lucciano. Su amistad, compañía y apoyo fueron cruciales para mantenerme en este camino, motivarme, y seguir en este proceso. Agradezco a todos mis amigos del Cerro Calán, quienes hicieron de mi paso por el magíster una experiencia muy buena cada día que pasaba, especialmente a Paula, quien siempre apoyó las iniciativas estudiantiles y me hizo crecer más como persona. Finalmente, agradezco a todos los funcionarios del Departamento de Astronomía de la U. de Chile, quienes a través de un rol silencioso, contribuyeron a que estudiantes como yo tengan todas las comodidades necesarias en Cerro Calán para poder realizar sus estudios con regularidad.

Table of Content

List of Tables

List of Figures

xi

xiii

Chapter 1

Introduction

Galaxy evolution is a branch of astronomy and astrophysics aimed at characterizing how galaxies evolve with cosmic time and what are the processes that drive the evolution. This area covers a wide range of scales ranging from cosmological, with studies of the spatial distribution of galaxies in the vast Universe, to the small scale physics of dust and gas particles in the interstellar medium. One of the biggest challenges in galaxy evolution is to constrain the elemental abundance of the gas in the interstellar medium (ISM). While we currently have a robust theoretical scheme to estimate the amount of metals in galaxies from emission line spectra (Osterbrock and Ferland, 2006), our observational capabilities have limited the characterization of metal abundances in high-z galaxies. In this work, we address the problem of estimating the chemical abundances of metals of the gas-phase of galaxies at $z \sim 2$ and beyond by making use of galaxies in the local Universe, providing a benchmark for elemental abundances of the interstellar gas in galaxies at high-z. For this, in the next few sections we present the relevant background, challenges, and the fundamentals of metallicity studies.

1.1 The Origin and Impact of Heavy Elements in the ISM

From the Big-Bang, the Universe started with a budget of atoms consisting mainly on hydrogen and helium. Stars begin to appear in the Universe when cold molecular gas clouds collapse by effect of gravity. Inside stars, hydrogen and helium fuel nuclear reactions that create heavier elements in a process called stellar nucleosynthesis (Hoyle, 1946). Elements with increasing atomic number up to iron are synthesized in the interior of stars and returned back to the ISM by stellar feedback. Type II supernovae events produced by the death of massive stars (M > 8 M$_\odot$) inject heavy elements to the ISM such as oxygen, neon, magnesium, and more. Carbon production is also dominated by this process while nitrogen is produced with a time lag by intermediate-mass stars (Henry et al., 2000). Oxygen and carbon are able to enhance nitrogen production through the CNO cycle in stars formed with recycled material

(Chiappini et al., 2003). Every generation of stars leaves its mark in the enrichment of the ISM and metallicity studies, therefore, shed light on how the stellar population of a galaxy evolves.

Metals and dust grains in the ISM can cool down hot gas to support further star-formation (Bovino et al., 2014, 2016). Among the proposed mechanisms for the origin of dust in galaxies there is grain growth from elemental abundances in the ISM, i.e., the creation of dust particles from heavy elements in the gas (e.g. Draine 2009). As well as dust, gas flows determine the enrichment of a galaxy. These flows can be traced by the fraction of metals produced and retained by unit stellar mass formed, which is defined as the *effective yield* in chemical enrichment models. The effective yield is sensitive to gas flows with different levels of enrichment (Edmunds, 1990) and adds complexity to the traditional closed box model (Talbot and Arnett, 1971). Galactic winds are another factor that can be traced by the metal content of a galaxy and it is very important to investigate the enrichment of the intergalactic medium (IGM) of galaxies through cosmic time (e.g. Kawata and Rauch 2007). Conversely, galaxies can accrete gas with different levels of enrichment from the IGM which also regulates the chemical budget of the ISM in galaxies. An example of this is the accretion of unenriched gas that can dilute the metal content of the galaxy (See Finlator and Davé 2008). This highlights the importance of measuring accurately the chemical budget of the gas in the ISM of galaxies. Which is what we address in the next sections.

1.2 How to Derive Elemental Abundances from Emission-Line Spectra

Among the variety of stars that can be formed by the collapse of a giant cold molecular gas cloud, we can find massive stars classified by their spectral features as O and B-type stars. These massive and young stars are very hot with effective temperatures of $T_{eff} \gtrsim 3 \times 10^4 K$ and they are able to produce a very hard radiation front (Osterbrock and Ferland, 2006). The energetic photons penetrate the ISM by ionizing the gas which is mainly composed by hydrogen, helium, and has a minor fraction of atoms with higher atomic number species in comparison, such as oxygen, carbon, nitrogen, etc. This process, called photoionization, effectively ionizes the hydrogen creating a cloud of free electrons that can further interact with ions through collisions and recombination (recapture of electrons). This cloud of gas ionized by massive stars are the so-called HII regions (Osterbrock and Ferland, 2006). HII regions exhibit recombination lines (RLs) and collisionally excited lines (CELs) in the optical range and in other wavebands such as the UV and IR. It is generally assumed that the physical conditions of HII regions are uniform in galaxies, but this has been proved to be a wrong assumption with findings of small scale variations (Mesa-Delgado and Esteban, 2010) and temperature inhomogeneities (Méndez-Delgado and García-Rojas, 2023). Such findings are

proposed to be responsible of the famous abundance discrepancy (AD; Peimbert 1967) where derivations of the metallicity of the gas using RLs and CELs give inconsistent results. This raises the need for alternatives to accurately calculate gas-phase chemical abundances.

HII regions are not uniform in terms of ionization. They have a structure defined by a differential ionization that depends on the radiation input of the star and the distribution of atomic species in the gas. The degree of ionization of atoms are different throughout the cloud and the extent of the regions that each species trace is defined by their Strömgren sphere (Strömgren, 1939). One way to describe the temperature of an HII region is dividing it into three ionization zones (Garnett, 1992). The innermost part of HII regions is strongly affected by the radiation of the star. The radiation is able to ionize most of the hydrogen and some atoms such as O^{2+}, He^+, Ne^{2+}, and more, creating a cloud of energetic electrons that excite atoms who later exhibit bright CELs observed in optical spectra. This is the denominated *high-ionization* or *high-excitation* zone. The outermost part of the HII region is the *low-ionization* zone where the radiation has lost some strength through the first layers of the gas and it is not able to ionize atoms at the same level than the high-ionization zone. The temperature of this zone is usually traced by ions of O^+ and N^+, and they are very sensitive to the density of electrons. It was assumed that a high and low-ionization zone were sufficient to model HII regions until Garnett (1992) introduced a third *intermediate-ionization* zone whose temperature is traced by S^{2+} and Ar^{2+} ions. Nowadays, the possibility of introducing a fourth extremely high ionization zone is being evaluated (Berg et al., 2021).

The abundance of elements can be determined from the intensity of RLs and CELs in the spectra of HII regions. The intensity of a line is directly related to the emission coefficient and the density of the ion species in question (Osterbrock and Ferland, 2006). Emission coefficients of RLs of elements have a temperature dependency that cancels when the ratios with respect to hydrogen RLs are taken. Nevertheless, their intensity highly depends on the amount of elements in the nebulae. As the level of metals compared to hydrogen is extremely low, these RLs are often not detected. On the other hand, using CELs is more practical as these lines are prominent in spectra of HII regions. The only disadvantage is that the strength of CELs depends on density and temperature. Therefore, CELs can be used to estimate chemical abundances as long as the physical conditions of the ISM are robustly calculated.

The problem of estimating abundances then, is linked to the problem of measuring the density and temperature of the ISM in galaxies. Luckily, these properties can be calculated from emission line ratios. Back in the 1940s the first methods were presented using ratios of emission lines to calculate electron temperatures from the [O III] line (Menzel et al., 1941) and densities from the [O II] doublet (Aller et al., 1949). The relative strength of CELs with large wavelength separation and of the same atomic species are sensitive to the temperature. For example, the temperature traced by [O III] can be estimated from the ratio

3

of the sum of [O III]λ4959 and [O III]λ5007 over [O III]λ4363. By assuming a Maxwellian distribution of electrons in the HII region the relative intensity of these lines depends largely on the energy distribution of the electrons that would be exciting atoms through collisions to the different states, in other words, they are sensitive to the temperature of the gas (Osterbrock and Ferland, 2006). On the other hand, optical spectra also show lines of the same atomic species that are very close in wavelength and have nearly the same excitation energy. The relative strength of these lines depends on the ratio of the collision strengths, which represent a statistical coefficient accounting for how frequently the atoms are de-exciting electrons. The strength of the lines and ultimately the value of the ratio then depends on the density (Osterbrock and Ferland, 2006). The most used lines for density estimations are the [O II]$\lambda\lambda$3726,3729 and the [S II]$\lambda\lambda$6716,6730 doublets.

Once density and the electron temperature of the different ionization zones are measured, the estimation of chemical abundances is straightforward and relatively easy to perform for elements such as He, O, N, S, Ne and Ar. This is due to the fact that the temperature is directly related with the chemical abundances. Metals are one of the main sources of cooling. More metal rich environments will cool down the nebulae more efficiently causing a decrease of the temperature of the gas. Mathematical descriptions have been proposed to describe this physical scenario (Osterbrock and Ferland, 2006) and several grids of models offer analytical solutions that we can use nowadays to calculate the chemical abundances taking advantage of their trends with temperatures. For details of the specific equations involved and caveats to consider in this type of measurements please refer to Section 3.6.

This method of calculating chemical abundances from temperature and density estimations is the so-called direct method. Direct gas-phase metallcities have been extensively investigated to probe galaxy evolution, from the nearest HII regions in the Milky Way, such as the Orion nebula, to nowadays observations of the first-galaxies in the Universe with the James Webb Space Telescope (JWST). To understand the rationale behind this research, we need to review some of the crucial aspects of metallicity studies from the present to the past Universe.

1.3 The Oxygen Abundance in the Local Universe

Among metals, oxygen is the most abundant element in the Universe after hydrogen and helium and it is readily observable because it has bright lines in the optical regime. There is a consensus that oxygen is the main tracer of the global gas-phase metallicity of a galaxy. Thanks to surveys like the Sloan Digital Sky Survey (SDSS; York et al. 2000) we have been able to study the properties of a large amount of galaxies in the local Universe and unveil fundamental trends in galaxy evolution, for example, the bi-modality of elliptical and star-forming galaxies (see Blanton and Moustakas 2009 for a review on the properties of

local galaxies). Galaxies in SDSS show a wide range of oxygen abundance covering $8.0 < 12 + \log(O/H) < 9.4$. Most remarkably, this gas-phase metallicity has been shown to be strongly correlated with stellar mass in what today we call the mass-metallicity relation (MZR) shown in Figure 1.1 (Tremonti et al., 2004).
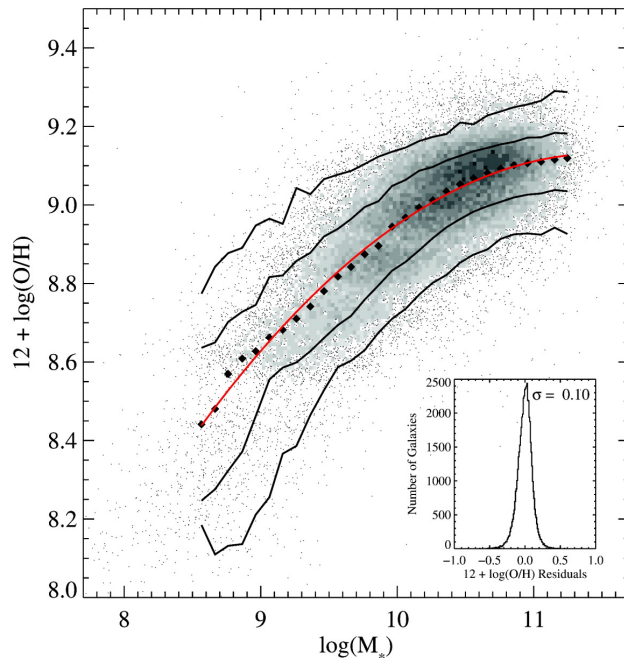
Figure 1.1: The mass-metallicty relation (MZR) of galaxies of the SDSS survey from Tremonti et al. (2004). Gray dots represent individual measurements of the gas-phase metallicity and stellar mass in units of solar masses. The black dots represent the median of 0.1 bins in solar mass and the solid black lines contain 68% and 95% of the data. The red curve show the best-fit mass-metallicity relation and the plot inside has the residuals of the fit.

The MZR is extremely important in galaxy evolution. It gives insights into what physical processes explain the amount of metals in galaxies. The trend of the MZR indicates that low-mass galaxies have lower gas-phase metallicities. Metals are synthesized in the interior of stars and low-mass galaxies have not formed a lot of stars during their lifetime. Since stars have a direct influence on the abundance of the gas in galaxies, lower metallicities could be partially explained by the low amount of stellar mass. Additionally, these galaxies have an amount of mass that is not able to produce a strong gravitational potential well that can retain the gas in the galaxy. The gas containing metals then can flow out easier than in high-mass galaxies, establishing another scenario that could help explaining the low-mass end of the MZR. On the other hand, the high-mass end of the MZR could be explained by the strong potential well that massive galaxies posses so that not much gas can escape the galaxy main body and they can easily be retained by the gravitational pull of the galaxy (see Chisholm et al. 2015 for a description of these processes as explanations of the MZR). As we can see, metallicity studies of galaxies in the local Universe alone can provide valuable insights on the star-formation history of galaxies (SFH) and impact enormously our conceptions on how galaxies evolve. Since its first suggestion (Lequeux et al., 1979), the MZR is an empiri-

cal relation that is useful as a constraint for chemical enrichment and star-formation models. Nowadays, the relation has adopted a new dimension including the star-formation rate (SFR) in the equation leading to the famous *fundamental* mass-metallicity relation (FMR; Ellison et al. 2008). The FMR provides more context to the MZR by including how galaxies are actively forming stars and gives more constraints to models of galaxy evolution. Studies suggest that the FMR does not evolve up to $z \sim 3.3$ (Sanders et al., 2021) which implies that galaxies with the same stellar mass and SFR at different z have the same amount of metals in the gas. With the new observations of JWST, recent work have suggested that the FMR does show evolution at very high redshift, particularly at $z > 6$ (Curti et al., 2024). These observations populate the low mass end of the MZR which also helps unveiling its shape and this provides information about what physical processes could drive the observed trends. The high redshift FMR suggest that galaxies with a set of stellar mass and SFR would have less metallicity than the predicted by the local FMR, giving insights into how enrichment should be in the early Universe. These findings are crucial to conclude on how gas accretion helps diluting the metal content of the gas and how gas flows evolve with cosmic time to finally understand how galaxies enrich throughout their lifetime.

Despite relations such as the MZR and FMR provide fundamental constraints that evolutionary models must reproduce, *we cannot state that these relations hold in the same way in the early Universe without accurate estimations of the metallicity in high-z galaxies.* In other words, as long as we do not prove whether these relations evolve with z we cannot confidently take them as a benchmark to compare with simulations and models of enrichment of galaxies in the early Universe. Particularly problematic is the fact that the relation derived differ depending on the method we used to determine the metallicity (Bian et al., 2017). This creates the necessity of measuring accurate metallicities of galaxies to characterize any existing trends that can be described by galaxies at higher z. This task, however, include a variety of observational challenges that we further describe here.

The first obvious problem that arises on determining oxygen abundances in distant galaxies is that they are too far to take spectrum of the same quality than in local HII regions. Most of the auroral lines useful to estimate electron temperatures such as [O III]$\lambda4363$ or [N II]$\lambda5755$ are already faint in local HII regions and the scenario gets worse at higher-z where galaxies appear fainter. The rest-frame optical emission lines also shift to redder wavelengths by a factor of $(1 + z)$ due to the effect of cosmological redshift. This implies that lines such as the auroral [O III]$\lambda4363$ which is crucial for electron temperature and metallicity calculations lie in the near-IR and beyond for galaxies at $z \gtrsim 1.0$. The big issue of IR spectra is that ground-based telescopes are limited by the atmospheric absorption of light due to the presence of molecules such as water and carbon-dioxide. Even with these difficulties, we can still figure out observational strategies to cover the [O III]$\lambda4363$ line in IR spectra, but having this auroral emission line in isolation is not enough to provide a robust full picture of the ionization of galaxies and their metallicity. For this, the challenge is even bigger be-

cause we would need to target galaxies in a specific redshift range to get as much auroral emission lines detections through the few atmospheric IR windows so that the temperatures and densities of the different ionization zones are reliably estimated. These problems led to alternative methods of estimating metallicities at high-z with a limited set of emission lines as we describe in the next Section.

1.4 Metallicity Studies of Distant Galaxies and the Role of Local Analogs

The most famous option to calculate metallicities at high-z is by the use of emission line ratios of bright lines known to vary with metallicity. This idea came up when Searle (1971) suggested that the systematic increase of line ratios (e.g. [O III]/Hβ) in HII regions at different radial distances from the center of the M33 galaxy (Triangulum galaxy) were due to abundance gradients. Since then, several authors have proposed various *strong emission line ratios* (SELRs) that can trace the variations in metallicity from source to source and involve, at the same time, the use of lines that are easy to detect due to their high brightness (see 3.8 for a list). Numerous authors have re-calibrated those relations based on photoionization models (e.g. Denicoló et al. 2002; Pettini and Pagel 2004; Nagao et al. 2006; Maiolino et al. 2008, and many more) and even proposed more in the way (e.g. Dopita et al. 2016). The use of these empirical relations is very practical and they opened a window to metallicity studies at earlier epochs of the Universe.

These relations have been used to estimate metallicities at high-z (e.g. Shapley et al. 2015). But are they really applicable in the early Universe? Precisely, the area of galaxy evolution has evidenced how galaxies change through cosmic time in a variety of characteristics, such as mass, star-formation activity, size, gas-budget, etc. (Shen et al., 2003; Rodighiero et al., 2011; Madau and Dickinson, 2014; Schreiber et al., 2015). The use of SELRs as indicators of metallicity comes from the discovery of metallicity-sensitive line ratios, but whether these sensitivities holds unchanged in the high-z Universe remains unclear. Interestingly, it has been found that the ISM of galaxies at higher-z is different from that of local ones, supporting the idea of changes in how the gas is ionized in galaxies at different epochs (e.g. Shapley et al. 2005; Erb et al. 2010; Steidel et al. 2014. The direct-method for estimation of metallicities is based on the temperature and density conditions of the ISM. If these properties of the ISM of high-z galaxies are different the use of empirical calibrations of SELRs vs gas-phase metallicities calibrated in the local Universe would not only not be valid, but they also could be biasing the oxygen abundance to values that can affect our view of fundamental relations of the Universe, such as the MZR. Many works in the literature have claimed to present direct-method metallicities in high-z galaxies (Christensen et al., 2012; Sanders et al., 2020; Arellano-Córdova et al., 2022; Taylor et al., 2022; Schaerer et al., 2022; Curti et al., 2022; Sanders et al., 2023), however, despite it being technically true that they used

the method to derive $T_e[O\ III]$ and the abundance of doubly ionized oxygen O^{2+}/H^+, their procedures still include the *assumption* of some model-based relation between $T_e[O\ III]$ and $T_e[O\ II]$ to estimate the singly ionized oxygen abundance O^+/H^+. Such relations are not known to hold in HII regions of high-z galaxies. This is mainly due to the lack of coverage of the $[O\ II]\lambda\lambda7319,7330$ doublet that is necessary to get $T_e[O\ II]$ and, consecutively, use it to estimate the total oxygen abundance of a galaxy (see Section 3.6 for details). This still emphasizes the need of valid relations to explore the applicability of SELRs and temperature relations in the early Universe. One possible solution to this issue is the use of the local analogs of high-z galaxies to calibrate the relevant relations.

Local analogs are galaxies that share similar physical conditions with galaxies at high-z, among the most relevant are the ionization parameter and electron density (See Chapter 2.2 for the definitions of these quantities and Bian et al. (2016) for more similar physical properties to high-z galaxies). Our expectations of the early Universe is that galaxies have had less time to assemble the metal budget that we observe in the local Universe so they should have less metallicity. This lead to studies of metal-poor analogs as laboratories of galaxies at high-z (e.g. Izotov et al. 2006; Zou et al. 2024). Alternative analogs have been proposed, e.g. with samples of galaxies with more extreme ionizing conditions such as it has been evidenced in high-z galaxies. Among them, we can find the green peas (Cardamone et al., 2009) and extreme emission line galaxies (Pérez-Montero et al., 2021). In 2016, Bian et al. (2016) defined a criteria to define analogs of high-z galaxies from local SDSS star-forming galaxies whose whose location in the BPT diagnostic diagram (Baldwin et al., 1981) resembles the strong line ratios of galaxies at $z \sim 2.3$ (Steidel et al., 2014). They found that such a sample of analogs has very similar ISM conditions compared to galaxies at high-z. Nevertheless, they provided re-calibrations of SELRs using spectra that lacked many detections of auroral lines, which are needed to perform metallicity calculations, making the authors to rely on stacked-spectra that can introduce statistical biases in the measurements.

In this work, we use optical spectra of 18 individual analogs of galaxies at $z \sim 2.3$ selected with the same criteria as Bian et al. (2016) to provide new empirical calibrations of metallicity with SELRs and temperature relations. This work is organized as follows: Chapter 2 contain a full description of the sample of galaxies and the data used in this work including selection criteria, observational techniques and data reduction. Chapter 3 describes all the procedures we followed to measure the metallicity and the relevant physical properties for the scientific problem proposed including all the required corrections, modeling of the SFH of the galaxies, emission line flux estimations and detailed step-by-step outline of the direct-T_e method. In chapter 4 we present our results on the ISM properties of our analogs, the temperature relations, and the metallicity calibrations. In Chapter 5, we discuss the implications that our findings have in the ionization conditions of galaxies at high-z. We also asses the ranges of values were our relations are valid and the impact they have on metallicity studies in the early Universe. Finally, our conclusions are summarized in Chapter 6. Throughout this

8

manuscript, we assumed a standard ΛCDM cosmology with $H_0 = 70$ km/s/Mpc, $\Omega_m = 0.3$, and $\Omega_\Lambda = 0.7$.

Chapter 2

The Data

This chapter is organized as follows: In section 2.1, we provide theoretical background of the BPT diagram to understand the selection criteria. Section 2.2 describes the data selection. In Section 2.3 we provide a review on the instrumental setup and observations of the local analogs. Section 2.4 describes the reduction and calibration steps. Finally, Section 2.5 provides information on the photometric data taken from SDSS to complement the analysis.

2.1 The BPT diagram

In pannels a) and b) of Figure 2.2, the Baldwin-Phillips-Terlevich diagram (Baldwin et al., 1981, BPT hereafter) for SDSS galaxies from Kewley et al. (2013a) is shown. The BPT diagram is a powerful tool used to distinguish the excitation source of the ionized nebular gas using a few *strong* emission lines that can be found in galaxy spectra, such as the Balmer Hα, Hβ, and oxygen lines. Based on the values of the emission line ratios, galaxies can be classified as star-forming, AGN, and composite. Currently, there are many versions of these diagrams, among the most commons are: 1) [N II]λ6584/Hα vs [O III]λ5007/Hβ (Baldwin et al. 1981; BPT-N2), 2) [S II]$\lambda\lambda$6717,6731 vs [O III]λ5007/Hβ, and 3) [O I]λ6300/Hα vs [O III]λ5007/Hβ (Veilleux and Osterbrock 1987; BPT-S2 and BPT-O1 hereafter). The lines involved in each emission line ratio are relatively close in wavelength, so the effects of dust correction and wavelength calibration issues are minimzed.

The main sources of excitation of the gas in galaxies are massive stars, AGN, and shocks. Shocks can be driven by several processes, ranging from stellar winds to galaxy-scale shocks due to interactions like mergers (e.g. Medling et al. 2015). Figure 2.2 shows the BPT-N2 diagram for galaxies of the SDSS survey (York et al., 2000). Galaxies whose gas is excited by star-formation branch together on the left side, where they can be clearly distinguished from those excited by AGN activity in the right side. The sequence formed by galaxies in this branch is usually called the *star-forming abundance sequence*, where the gas is excited in the form of HII regions and it is characterized by being a sequence in metallicity. Increasing the metallicity would move a galaxy along the sequence towards the bottom-right of the

BPT-N2 diagram. AGNs have a harder radiation field to excite the [O III] line to the same level that star-formation or even further, but they also exhibit higher [N II] emission due to their usually massive and metal-rich host galaxy (Thomas et al., 2018), occupying a different region shifted to the right side of the diagram. Nonetheless, it is known that AGNs can also hold star-formation in their disks. The mixture of these two excitation mechanisms give place to the so called *mixing sequence*, that connects the star-forming abundance sequence with the AGN region in the lower part of the BPT-N2 diagram (Between -0.5 and 0.0 in both axis of Figure 2.2). This branch would be populated by low-metallicity AGNs that present less [N II] emission and have low to moderate star-formation activity to excite the [O III] line. These types of sources are also referred as *composite galaxies* when classifying galaxies by their ionization source.
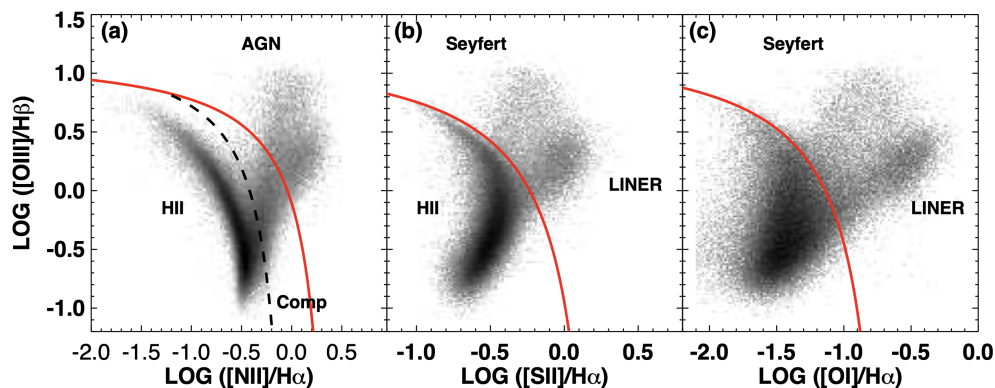
Figure 2.1: (a) BPT-N2, (b) BPT-S2, and (c) BPT-O1 diagrams taken from Kewley et al. (2006). The red lines define the classification boundaries separating HII regions from AGN and LINER galaxies. The black dashed line is the demarcation of extreme starburst galaxies defined by Kauffmann et al. (2003), which also defines the region where composite galaxies live in the BPT-N2 diagram..

The demarcations defined by the BPT diagrams to classify sources according to their excitation mechanism have been tweaked through the years. Based on theoretical models (Kewley et al., 2001), observations (Kauffmann et al., 2003; Brinchmann et al., 2004), and a combination of both (Stasińska et al., 2006), the classification boundaries have been extensively explored to provide the cleanest samples of each kind of source. Figure 2.1 shows examples of the three BPT diagrams aforementioned including the boundaries that define the distinct classes of galaxies proposed by Kewley et al. (2006). The BPT-S2 and BPT-O1 diagrams are sensitive to low-ionization lines such as [S II] and [O I], useful to separate galaxies whose emission is dominated by shocks or to classify low-ionization nuclear emission-line region galaxies (LINERs), where emission from low-ionized lines such as [O I], [O II], [S II], [N II] is more powerful.

Models suggest that the star-forming abundance sequence can change its position in the BPT-N2 diagram depending on the hardness of the ionization (Kewley et al., 2013a). Panel
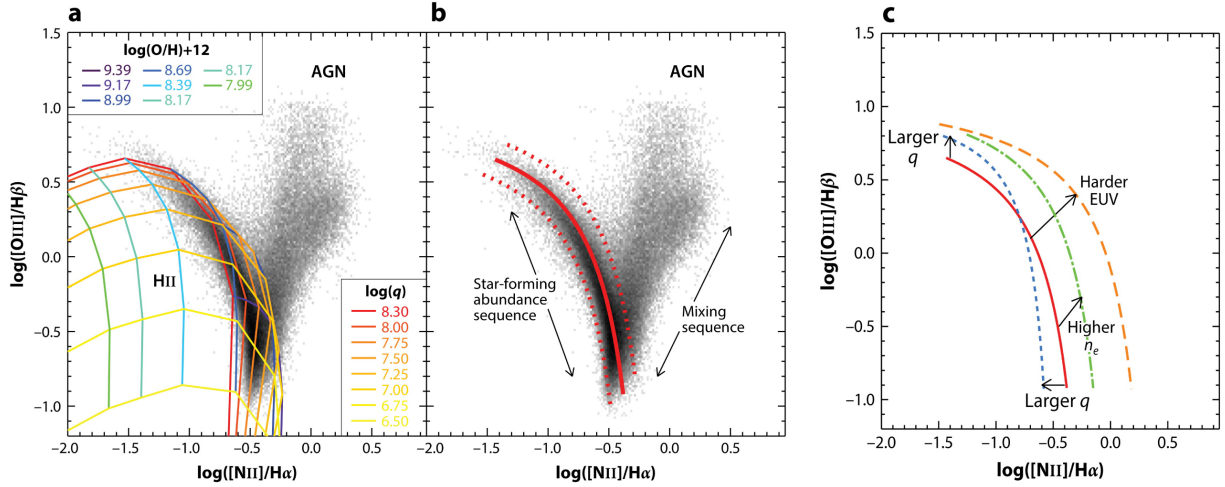
Figure 2.2: BPT-N2 diagram from Kewley et al. (2013a). Gray dots in panels (*a*) and (*b*) are the measurements of emission line ratios of galaxies individual galaxies from the SDSS survey (York et al., 2000). (*a*) Grid of photoionization models of metallicity and ionization parameter of the star-forming abundance sequence. (*b*) A cleaner version of the diagram where the star-forming abundance sequence and the mixing sequence are indicated with black arrows. The red solid line represents the mean of the star-forming abundance sequence whose shape and position are determined by the models and SDSS galaxies respectively. The red dashed lines are the errors of the models showing a ± 1 dex from the sequence. (*c*) Star-forming abundance sequence illustrating variations with electron density (n_e), ionization parameter (q), and the extreme UV emission from stars (EUV).

(c) of Figure 2.2 shows how this sequence changes when varying the electron density (n_e), ionization parameter (q or $U = q/c$), and the hardness of the extreme UV spectrum of stars (EUV). The electron density, as the name indicates, represent the number density of electrons in an HII region. Since hydrogen is well ionized by massive stars, it is also thought as an approximate indicator of the hydrogen density. The ionization parameter is defined as the rate of hydrogen ionizing photons over the number of hydrogen atoms in the cloud. It gives useful insight into the ionization state of the nebulae: The harder the far-UV emission, the larger the ionization parameter. It also depends on the density and the filling factor (ε), which is the fraction of the nebula that is filled with gas. The definition of the ionization parameter as q or U assume spherical geometry of HII regions. Studies have made attempts to get rid of this assumptions by adopting alternative definitions that do not depend on geometry (e.g. the Γ parameter; see Steidel et al. 2014). Finally, the extreme UV emission is just the hardness of the emission from the far-UV emitted by stars and is an indicator of how massive and hot are the stars ionizing the gas. This parameter is sensitive to the initial mass function (IMF) that is defined as the initial distribution of masses of a stellar population. If the IMF is top-heavy, more massive stars will be there to produce harder radiation fields that trigger higher ionization.

2.2 Data Selection

Studies have presented evidence of evolution of the BPT diagram with redshift (e.g. Erb et al. 2006; Shapley et al. 2005; Erb et al. 2010; Shapley et al. 2015). Towards high redshift, star-forming galaxies seem to slightly increase their [O III]$\lambda5007$/Hβ and [N II]$\lambda6584$/Hα ratios. The physical reason behind these offsets still remains under debate. Larger ratios could be produced by a higher ionization parameter, higher electron density, or higher N/O ratios (Steidel et al., 2014; Bian et al., 2020; Garg et al., 2022). Panel (c) of Figure 2.2 shows how models predict the change in the position and shape of the star-forming abundance sequence when varying the ionization conditions. It suggest that offsets to higher ratios in both axis can have place when galaxies have higher n_e and harder extreme ultra-violet emission (EUV), which is more typical in massive galaxies and AGN driven ionization. Furthermore, the shape of the sequence changes to higher [O III]$\lambda5007$/Hβ and lower [N II]$\lambda6584$/Hα when the ionization parameter is increased, favoring galaxies with more extreme ionization conditions due to star-formation activity in the top-left side of the BPT-N2 diagram (Kewley et al., 2013a,b).

Steidel et al. (2014) used near-IR spectra from the Multi-Object Spectrometer for InfraRed Exploration of the Keck Baryonic Structure Survey (KBSS-MOSFIRE Survey; Strom et al. 2015), to study a sample of star-forming galaxies observed at $z \sim 2.3$. These galaxies group above the local star-forming abundance sequence with harder ionization conditions as suggested by the BPT-N2 diagram. Indeed, they found that the data is consistent with models of an input black-body radiation from very hot stars with $50000 < T_{\text{eff}} < 55000$ K. The effective temperature of stars needed to explain their position is, however, senstivie to other properties such as the electron density. Unlike the local star-forming abundance sequence, they also show that the $z \sim 2.3$ locus has a much reduced dependence on the N/O ratio and metallicity while it is more sensitive to the ionization parameter. From these results, a region of the BPT-N2 diagram can be defined to search for galaxies with similar ionization conditions to galaxies at $z \sim 2.3$. Accordingly, the data selection in this work is made on local galaxies whose position in the BPT-N2 diagram overlaps with the high redshift locus. We define our sample of galaxies as a sub-sample selected from the Max-Planck Institute for Astrophysics and the John Hopkins University catalogs on galaxy properties (MPA-JHU group[1]) based on the 7th data release of Sloan Digital Sky Survey (SDSS) (York et al., 2000; Abazajian et al., 2009). Bian et al. (2016) defined three boundaries in the BPT-N2 diagram to enclose the region where local SDSS galaxies should lie to resemble the properties of galaxies in the $z \sim 2.3$ locus. The boundaries are defined as follows:

$$\log([\text{O III}]/\text{H}\beta) > \frac{0.66}{\log([\text{N II}]/\text{H}\alpha) - 0.31} + 1.14 \tag{2.1}$$

$$\log([\text{O III}]/\text{H}\beta) < \frac{0.61}{\log([\text{N II}]/\text{H}\alpha) - 0.47} + 1.19 \tag{2.2}$$

---

[1]https://www.sdss4.org/dr12/spectro/galaxy_mpajhu/

$$\log([\text{N II}]/\text{H}\alpha) < -0.5 \qquad\qquad (2.3)$$
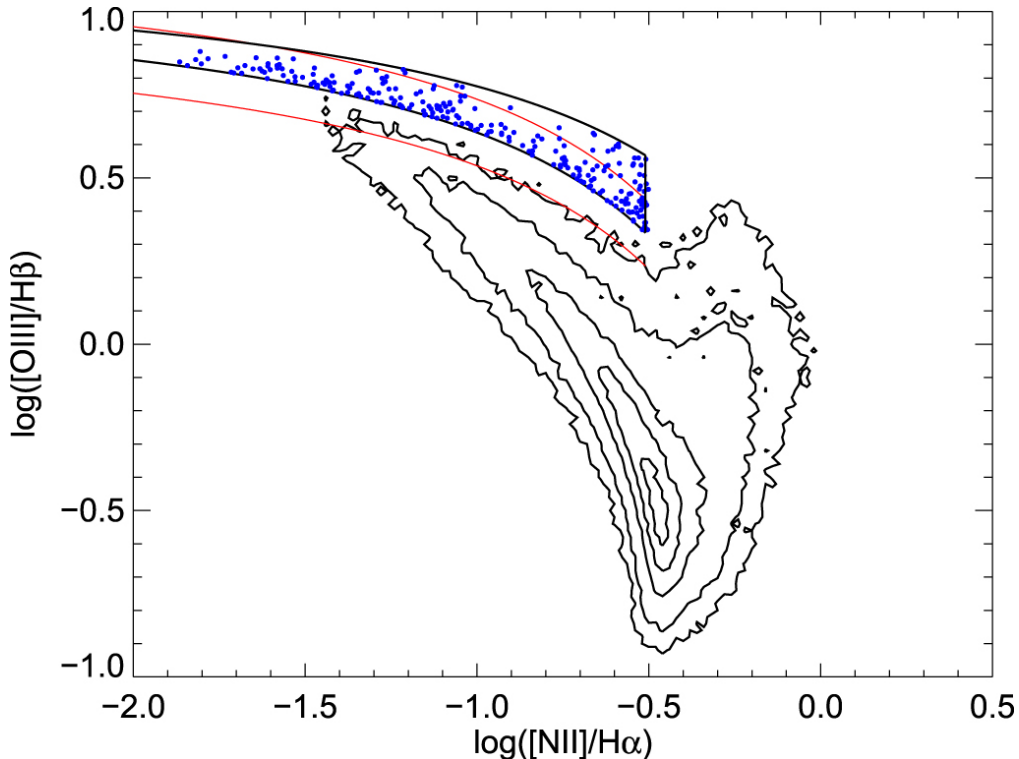
Figure 2.3: BPT-N2 diagram of star-forming and composite galaxies in SDSS taken from Bian et al. (2016) shown as black contours. The red solid lines enclose the vertical region of galaxies at $z \sim 2.3$ (Steidel et al., 2014). Black solid lines draw the region where galaxies meet the criteria described in Section 2.2. Galaxies inside the black curves are marked by blue dots and represent the selected SDSS local analogs by Bian et al. (2016), from where a sub-sample of 18 galaxies was drawn for this study.

Figure 2.3 shows the BPT diagram of SDSS galaxies, the limits of the $z \sim 2.3$ locus according to Steidel et al. (2014), and the selection criteria from Bian et al. (2016). The bottom boundary on Eq. 2.1 is slightly higher than the relation from Steidel et al. (2014) to decrease the probability of including normal star-forming galaxies with insufficient ionization strength to resemble the high redshift ISM conditions. The upper boundary given by Eq. 2.2 corresponds to the limit of starburst models defined by Kewley et al. (2001) that modelled theoretically extreme ionization conditions of the gas in star-forming galaxies. Ultimately, the right boundary in Eq. 2.3 is defined to avoid including AGN activity as a source of ionization in the sample (e.g. Brinchmann et al. 2004; Stasińska et al. 2006). It can be appreciated that the region selected effectively overlaps with the $z \sim 2.3$ star-forming abundance sequence. The sample selected populates mostly the bottom part where the overlap occur between the Bian et al. (2016) criteria and the Steidel et al. (2014) high-z galaxies. Nonetheless, there is still a range where galaxies with higher [O III]$\lambda 5007$/Hβ than the Steidel et al. (2014) upper boundary can be selected, although a minor fraction of analogs is found there. In principle,

sources selected in such region would have the highest [N II]λ6584/Hα compared to the rest of analogs, and hence, one would expect galaxies with both higher metallicity and harder ionization conditions.
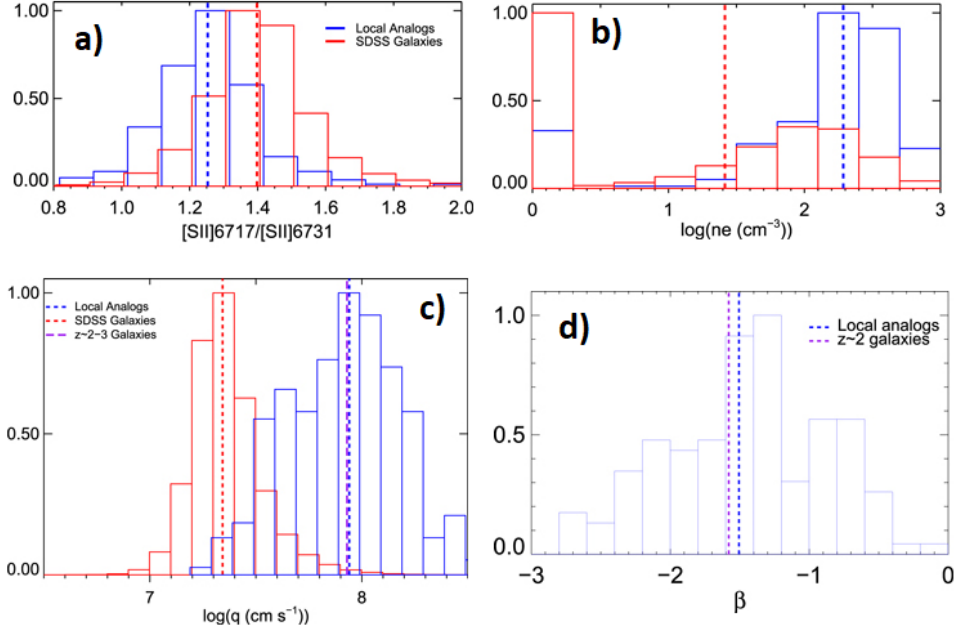
Figure 2.4: Comparison between the distributions of physical parameters of the selected local analogs against SDSS normal star-forming galaxies taken from Bian et al. (2016). Panel a), b) and c) show the distribution of the [S II]λ6717/[S II]λ6731 ratio, electron density and ionization parameter for local analogs (Blue) and normal SDSS local star forming galaxies (Red). Dashed lines represent the median of each distribution with its corresponding color. The purple dashed line in panel c) is the median ionization parameter for galaxies at $z \sim 2 - 3$ from Nakajima and Ouchi (2014). Panel d) shows the distribution of the UV-slope of the selected analogs compared to the mean slope of galaxies at $z \sim 2$ from Bouwens et al. (2009).

To ensure these local sources are good analogs of star-forming galaxies at high-z, Bian et al. (2016) explored the ionization conditions of their ISM. Figure 2.4 shows the distribution of the [S II]λ6717/[S II]λ6731 ratio, the electron density, the ionization parameter, and the UV-slope (β). The electron density calculation is based on the [S II]λ6717/[S II]λ6731 ratio, similarly to how it is explained later in Section 3.6. Lower values of the [S II] doublet ratio lead to higher n_e. A median of nearly one order of magnitude higher was found on local analogs compared to the SDSS galaxies in panel b) of Figure 2.4 mainly due to the large amount of nearby galaxies with lower values. Higher ionization parameters are also thought to drive similar ionization conditions than the electron density in high-z galaxies (See Panel c) of Figure 2.4). The median value of q for local analogs remarkably agrees with the median ionization parameter of galaxies at $z \sim 2 - 3$ (Nakajima and Ouchi, 2014). Furthermore, the UV continuum slopes of the candidates are in good agreement with the slopes of galaxies at $z \sim 2$ (Bouwens et al., 2009). This indicates that the analogs share a similar dust extinction than in galaxies at $z \sim 2$, since the UV continuum slope is most strongly driven by dust

15

content. However, this is only the case when we are comparing galaxies of similar UV luminosities.

We filtered the sample of galaxies that meet the selection criteria by asking for sources with reliable line measurements and physical parameters in SDSS to ensure we are indeed targeting galaxies. We selected galaxies with $z < 0.2$ and a signal-to-noise ratio of 10 for [O III]λ5007, Hα, and Hβ; 5 for the [S II]$\lambda\lambda$6716,6730 doublet; and 3 for [N II]λ6584 and the [O II]$\lambda\lambda$3726,3729 doublet. This leads to a sample of 28 observable sources in the southern hemisphere from which we observe 18 as it is outlined in Section 2.3.

2.3   Observations: Strategy & Setup

We conducted deep, medium-resolution optical spectroscopic observations of 18 local analogs in four observing nights earned through the *Chilean Time Allocation Comittee* (CNTAC). The spectra was gathered with the Magellan Echelle Spectrograph (MagE), mounted at the Baade 6.5m Telescope in Las Campanas Observatory (LCO[2]). Table 2.1 shows an R.A. ordered list of the sources in this study, including their ID, coordinates, z, and observing conditions such as the semester where they were observed, the airmass, seeing, and total exposure times. The spectra were collected with the $1''$ slit since most of them are compact sources ($\sim 1'' - 2''$). The spectrograph covers from 3200 to 10000 Å with a spectral resolution of $R \sim 4100$ for such slit[3], allowing us to separate line doublets by resolving down to FWHM ~ 100 km/s. The wavelength coverage allowed us to span all the necessary emission lines to unambiguously determine the electron temperature and chemical abundances by means of the direct-T_e method.

The observation strategy and setup is based on the recommendations in the MagE User Manual[4]. All galaxies where observed with the default slit orientation of 44.5 HRZ which align the slit with the parallactic angle defined by each object. The images were taken with a 1×1 binning in spectral and spacial direction. Indeed, the $1''$ slit used in this setup lead to emission lines with FWHM of the order of 100 km/s considering instrumental broadening (see Section 3.4), being able to resolve unambiguously some line doublets needed in this study, such as the [OII] and [SII] doublets (see Figure 3.5 in Section 3.4). Galaxies in our sample have SDSS g$'$ magnitudes between 16 and 20, with 50% of the sources having between 19 and 20 magnitudes (see Table 2.3 in Section 2.5). In Figure 2.5, we compare the brightest and the two faintest examples of the auroral [O III]λ4363 line in our spectra with a simulation of a flat AB spectrum with magnitude $g' = 19$ using the LCO Exposure Time Calculator[5]. The simulation follows the same setup than our measurements plus the addition of a [O III]λ4363

---

[2]https://www.lco.cl
[3]https://www.lco.cl/wp-content/uploads/2022/09/MAGEhandout2022.pdf
[4]https://www.lco.cl/?epkb_post_type_1=the-mage-spectrograph-user-manual
[5]https://www.lco.cl/lcoastronomers/~iss/lcoetc/html/lcoetc_sspec.html

Table 2.1: List of local analogs observed with Magellan MagE

Source	R.A. (hh:mm:ss)	Dec (dd:mm:ss)	Redshift[a]	Run[b]	Airmass[c]	Seeing[c] (″)	Exp[d] (s)
J0021+0052	00:21:01.02	+00:52:48.11	0.098	2018B	1.156	0.9	5400
J0023−0948	00:23:39.61	-09:48:48.72	0.053	2023A	1.305	1.3	5400
J0136−0037	01:36:30.59	-00:37:55.97	0.059	2019B	1.142	0.9	2700
J0240−0828	02:40:52.19	-08:28:27.41	0.082	2018B	1.125	0.9	2570
J0252+0114	02:52:34.29	+01:14:43.94	0.028	2019B	1.159	0.9	2700
J0305+0040	03:05:35.11	+00:40:59.24	0.086	2019B	1.204	0.8	4500
J0950+0042	09:50:23.31	+00:42:29.25	0.098	2019A	1.1555	0.775	3600
J1146+0053	11:46:49.33	+00:53:46.09	0.057	2019A	1.16	0.8	5400
J1226+0415	12:26:11.89	+04:15:36.07	0.094	2019A	1.231	0.8	5400
J1444+0409	14:44:41.37	+04:09:41.73	0.039	2019A	1.1975	0.75	3600
J1448−0110	14:48:05.38	-01:10:57.68	0.027	2019A	1.334	0.7	3000
J1624−0022	16:24:10.11	-00:22:02.60	0.031	2023A	1.162	0.86	7200
J2101−0555	21:01:14.39	-05:55:10.29	0.196	2019A	1.3145	0.65	3600
J2119+0052	21:19:58.30	+00:52:33.55	0.034	2019A	1.2545	0.6	3600
J2212+0006	22:12:43.05	+00:06:48.55	0.177	2023A	1.437	1.565	4800
J2215+0002	22:15:23.05	+00:02:46.79	0.077	2018B	1.1545	0.85	7200
J2225−0011	22:25:10.13	-00:11:52.89	0.067	2018B	1.3125	1.0	3600
J2337−0010	23:37:51.93	-00:10:00.50	0.072	2019B	1.147	1.0	5400

[a] Redshift estimation from SDSS.
[b] Observation run. A and B represent the first and second semester of the respective year.
[c] Median airmass and seeing between exposures.
[d] Total exposure time.

line with a peak intensity of 3×10^{-17} erg/s/cm^2. We give the simulator an airmass of 1.2, seeing of 0.8″, and extraction aperture of 1.5″ (5 pixels with this setup). We observe that integration times of 1.5 hrs (5400s) give enough signal-to-noise with levels above 10 in both the emission line and the continuum with this setup, as it is illustrated by the J0021+0052 galaxy. The line reaches the 10σ level at the peak of the flux for J1624−0022 and J2212+0006 that have exposures of 2 and 1.3 hrs respectively, which are the two faintest spectra in our sample. In terms of sensitivity, exposures of 30 minutes (1800s) are enough to detect the line unambiguously, allowing us to even have sensitive enough data in galaxies with less integration time due to any kind of overheads. Furthermore, long exposures can cause hard contamination from cosmic rays in MagE frames and saturation of brighter lines such as [O III]λ5007. This is undesired since we need to accurately constraint the flux of this line among many others to perform our analysis. We minimized the contamination and avoided saturation effects by dividing the observation into exposures of 30 minutes each, which gives sufficient SNR by coadding a few of these frames in the reduction. Note that exposure times of Table 2.1 are the total exposure times resulting from the summation of the individual frames coadded in the reduction.
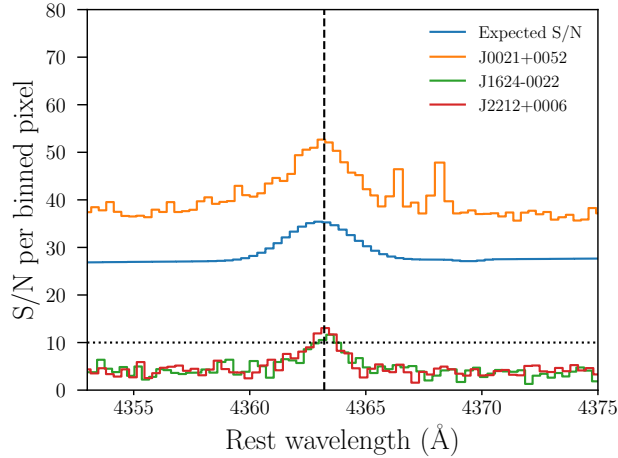
Figure 2.5: Signal-to-noise ratio per binned pixel for the [O III]λ4363 auroral line whose wavelength is indicated as a vertical dashed line. Blue steps show the simulated signal-to-noise with the LCO Exposure Time Calculator for a source with $g' = 19$. Orange steps represent the spectrum of J0021+0052 which is the galaxy with the highest SNR in our sample. In contrast, green and red steps are the faintest spectra from our dataset, J1624-0022 and J2212+0006. Although the stellar continuum is below the 10σ limit highlighted by the horizontal dotted line, the peak of intensity of [O III]λ4363 in the worst cases does reach the desired signal-to-noise > 10.

The first observation run took place on the night of October 7th, 2018 (PI: González, V). Four galaxies were observed during this run indicated as 2018B in the *Run* column in Table 2.1. The night had a varying seeing in the range $0.85''$-$1.0''$ and all objects were visible at adequate altitudes in the sky (airmass $\lesssim 1.3$). Observations had to be stopped at UT $\sim$ 5:30 due to bad weather conditions leading to less integration time on J0240-0828 than desired. Image frames from J0021+0052, J2215+0002, and J0240-0828 were affected by clouds, but most of the exposures of these sources have good enough S/N such that the combination with other good frames in the reduction gives good spectra with clearly detected lines. Feige110 and LTT7987 spectrophotoemtric standard stars were observed in between the sources to perform flux calibration (see a list of the standard stars in Table 2.2). The second observation run was on May 9th, 2019 (PI: González, V; 2019A in Table 2.1) where seven galaxies were observed. The seeing was ranging between $0.7''$-$0.9''$, but it dropped down at the end of the night to $0.6''$. The sources in this case were not as high in the sky as galaxies in 2018B where four galaxies were observed with > 1.2 airmass. No bad weather conditions were reported during this night. The stars GD108, HR4963, and LTT7379 were observed in this case. The third run took place on the night of September 22th (PI: González, V; 2019B in Table 2.1). In this night, six galaxies were observed with a seeing of $0.8''$-$1.0''$ in good weather conditions and airmass. However, the observed standard stars Feige110 and EG21 filled the slit almost completely, covering all the orders and making the reduction impossible to complete with this dataset. We tackled this problem by including observations of Feige110 from the night of 2018B instead of the bad standard star data. Finally, three galaxies where observed in the night of June 12th, 2023 (PI: Navarrete, B; 2023A in Table 2.1). We used

half of the night to re-observe galaxies from 2019B to get a more reliable reduction. This is the case for J0023-0948 and J2212+0006, while the new source J1624-0022 was added. The night sky was clear, but the objects were quite low in altitude, causing observations with higher airmass compared to the rest of our sample. Furthermore, the seeing got worse by the end of the night reaching a median of 1.565 for J2212+0006. The used standard star for this night was LTT6248. In summary, we end up with optical spectra of 18 local analogs: 4 from 2018B, 7 from 2019A, 4 from 2019B, and 3 from 2023A.

Table 2.2: Spectrophotometric standard stars observed to perform flux calibration.

Standard	R.A. (hh:mm:ss)	Dec (dd:mm:ss)	Run[*]	Airmass[*]	Seeing[*] (″)	Exp[*] (s)
GD108	10:00:47.24	-07:33:30.77	2019A	1.082	0.9	1260
HR4963	13:09:56.98	-05:32:20.41	2019A	1.3525	0.95	2
LTT6248	15:38:59.64	-28:35:36.97	2023A	1.2665	1.075	1200
LTT7379	18:36:25.95	-44:18:36.90	2019A	1.1335	0.6	3600
LTT7987	20:10:56.84	-30:13:06.62	2018B	1.002	0.95	660
Feige110	23:19:58.39	-05:09:56.17	2018B, 2019B	1.903	0.92	600

[*] Same as Table 2.1

A standard observation with MagE includes collecting several calibration frames to carry out the data reduction of the science frames. Between these, we can find red flat-fields, blue flat-fields, very blue flat-fields, order definition flat-fields, and ThAr frames. All calibration and science frames are taken with the 1″ slit and the spectrograph in focus, except for the blue and very blue flat-fields that are collected with the 5″ slit and de-focused spectrograph. The nominal focus of MagE changes from time to time, but it is always around 2900. Our sources and calibration frames were observed with a focus of 2800 in 2019A, 2860 in 2019B, and 2902 in 2023A (Night of 2018B have no reports of focus in the log). We follow the manual recommendations and took the calibration frames in slow readout mode as this is the mode in which science frames were created. With this setup, from 15 to 20 red flat-field frames were collected by turning on the quarz lamp with a power of 5.0 V and 25s of exposure time. As the name indicates, these calibration frames are used to illuminate the reddest orders of the spectrograph and create sensitive flat-fields for their corresponding wavelengths. The order definition flat-fields are taken by exposing the spectrograph to an Xe-flash lamp in focus. We take 5 frames of 25s and other 5 frames 60s each. These are used to trace the edge of the echelle orders. The night of 2018B includes twilight flat-fields that are taken by opening the shutter to the bright sky during the twilight. The use of twilight flats is recommended over other frames due to their good performance on tracing the edges since they illuminate all the orders very well and uniformly. As mentioned before, to take blue flat-fields we expose the 5″ slit of the spectrograph to an Xe-flash lamp bringing down the focus to 1100. Sets of 5 to 15 blue flat-fields of 15s exposure are gathered during our nights with the turbo and

slow readout mode giving a total of ~30 frames per night. The very blue flat-fields are the same as the blue flat-fields, but with 100s of exposure time to illuminate the bluest orders of the spectrograph. 5 frames of these are observed each night. Both blue and very blue flat-fields are used to illuminate the bluest orders of the spectra to map the sensitivity of those wavelengths during the reduction. Finally, the ThAr frames are images of a Thorium-Argon lamp of 4s to 5s of exposure. As it is said that the spectrograph tilts throughout one night of operation, these frames are constantly taken between science and standard star exposures to avoid wavelength calibration issues. In the reduction of each individual source, the closest ThAr frame observed is used for the wavelength calibration. The number of calibration frames of each class follow the recommendations of the MagE User Manual for our specified setup.

Table 2.2 shows the list of standards involved in this study. Each of these stars were selected among the closest visible standards to our sources. The exposure times are decided depending on the brightness of each star to avoid saturation. Standard frames are used to flux calibrate the spectra and their characteristic thin continuum in each order is useful to trace the center of the source when reducing the science frames.

2.4   Reduction & Calibration

Magellan/MagE Echelle data were reduced with version 1.13.0 of PypeIt (Prochaska et al., 2020b,a), an open-source python pipeline for spectroscopic data reduction. In general terms, the reduction of echelle data proceeds with a tracing of order edges, object detection, flat-fielding, spatial illumination correction, tilt correction, wavelength calibration, sky-subtraction, and source extraction. Furthermore, the pipeline includes routines to flux calibrate the spectra and correct by telluric band absorption. In this section we describe the detailed procedure we took to reduce the spectra.

In principle, the ideal reduction would include the mixture of red and blue flat-fields to create a complete flat-field and cover enough extent from redder to bluer orders. Although the pipeline creates such calibration image it cannot be used to reduce the data due to numerical issues according to PypeIt error messages. By evaluating the possibility of using only one type of flat-field frame, we realized there is a sensitivity loss in blue and red orders when using each type of flat-field. Not all the orders are well illuminated, and the pipeline is not able to perform good sky subtraction in orders with low sensitivity, giving a heavily contaminated spectrum. Therefore, we decided to carry out a blue and red reduction for each target separately to get the best quality spectra in both wavelength regimes.
5
We follow the procedure described in Xu et al. (2022). We used the order definition frames to trace the order edges in the blue reduction of each galaxy in each night, except

for the night of 2018B where we used the available twilight flats as recommended. On the other hand, the reduction of the red part of the spectra does not allow to trace the slits with the order definition frames, but the red flat-fields were sharp and bright enough to get proper edge tracing and order detection. PypeIt does not perform a good sky subtraction around bright emission lines by default, thus, boxcar extraction is the best option against optimal extraction to get suitable reduction for our science. PypeIt performs optimal and boxcar extraction simultaneously, nonetheless, the boxcar extracted spectrum shows flux loss and irregular shapes in bright emission lines when done at the same time with optimal, due to the effect of bad sky subtraction. Due to this problem, we decided to reduce the data only with boxcar extraction. Currently, building sensitivity functions from boxcar extracted spectra is not available in PypeIt. Hence, we reduced the stars with optimal extraction which in turn is better for good continuum emission sampling. The sensitivity functions are then derived with the `pypeit_sensfunc` script that internally uses spectra from CAL-SPEC and ESO spectrophotometric standard stars[6] to calculate the factor used to convert counts to flux units. Each galaxy was calibrated using the sensitivity function derived from optimal extraction over the source extracted with the boxcar method, selecting the nearest standard star in R.A., airmass, and time of the observation in each night. Additionally, the center of each order where the continuum of the galaxies are observed, is traced using the position of the continuum detected in the standard stars which is needed due to the characteristic faint stellar continuum of our galaxies. We coadded the reduced frames with the `pypeit_coadd_1dspec` tool to create weighted 1D spectra using the `velocity` method to sample wavelengths uniformly in velocity (Or logarithmically rebinned). Subsequently, a polynomial fit to the telluric grid models from LCO provided by PypeIt was used to correct from telluric band absorption contaminating the spectra. Spectra of sources with higher S/N require a polynomial of degree 10 to remove almost completely the telluric absorption bands. In the low S/N cases, a degree of 5 is enough. Higher polynomial degrees result in overfitting and leave artifacts that resemble absorption in some emission lines. Finally, we combine the spectra as a post-processing step maintaining the best from the red and blue part of each reduction. Down to Hβ we obtained remarkable quality in the red spectra. Thus, we manually merge the blue spectra for shorter wavelength lines ($\lambda < \lambda(\mathrm{H}\beta)$) preserving good consistency between the continuum level and noise ($\sim 4500 - 5000$ Å depending on the redshift).

This procedure worked perfectly for all nights except for the 2019A run. The reduction of the blue part with the same procedure did not work for this night due to PypeIt numeric problems again. In this particular set of 7 galaxies we manually added the reduction of an extra order at blue wavelengths to the red reduction in order to cover the [O II]$\lambda\lambda3726,3729$ doublet and partially solve the problem. The red reduction is able to cover most of the lines that we needed for this study, even more, the blue reduction is not necessary for the case of J2101-0555 due to its redshift of 0.196 that shifted all lines into the available wavelengths.

---

[6]https://www.eso.org/sci/observing/tools/standards/spectra/stanlis.html

However, as previously mentioned, the bluer orders are not well reduced when using red flat-fields and vice versa, giving unreliable estimates of the flux of the bluest emission lines. It is not until the release of PypeIt v1.15.0 that we could fix this issue. This new version allowed us to reduce the blue part of 2019A galaxies, so we re-reduced these 7 galaxies according to the general procedure we adopted for the other nights. The only worth-to-mention difference between v1.13.0 and v1.15.0 is that the use of the telluric model of the sky at LCO was deprecated in the last version, replacing it by the use of a model using principal component analysis (PCA). We use a telluric PCA model with coverage between 3000Å and $2.6\mu m$ and $R \sim 10000$. The telluric correction for all sources is satisfactorily removed with a polynomial of degree 5. We further tested whether significant differences were introduced to our reduction procedure between versions by comparing the reduction of a galaxy of another night with the two versions finding no difference in the spectrum.

An example of the result of the reduction procedure is shown in Figure 2.6. The upper panel shows the raw 2D spectrum of J0021+0052 as an image of 2048×1024 of the CCD. The exposure reveals the light emitted from the ISM of the galaxy with several emission lines as bright spots, while every order is crossed by an horizontal line corresponding to the stellar continuum emission. Sky emission lines and absorption features are present in the reddest orders as vertical bright lines (Wavelength is decreasing towards the right and bottom side of the image inside and between orders, respectively). The reduced 2D spectrum is shown below where the sky emission there was already subtracted. The image was rectified and corrected to get straight orders and emission lines from where the 1D spectrum is extracted. Here, we already identify clearly some bright emission lines such as the $H\alpha$ + [N II] profile, [O III] and $H\beta$ lines. The bottom of Figure 2.6 shows the 1D extracted spectrum for the same galaxy where we see the rich set of emission lines with remarkable sensitivity to carry out this study. We observe many Balmer series lines, He I lines, the [O II]$\lambda\lambda$3726,3729 doublet, [O III]λ4363, [O III]λ4959, [O III]λ5007, [S III]λ6312, [N II]λ6548, $H\alpha$, [N II]λ6584, the [S II]$\lambda\lambda$6716,6731 doublet, and the [O II]$\lambda\lambda$7319,7330, and many others.

2.5   Photometry

Our study require measurements of the flux of Balmer emission lines of the gas, with $H\alpha$ and $H\beta$ among the most important ones. These lines suffer from absorption of hydrogen in the atmospheres of A-type stars. To get the real flux of Balmer lines, one need to correct for this absorption by studying the continuum spectra of the underlying stellar population in our galaxies where the absorption cannot be measured explicitly. To model the stellar spectra we used photometric data from SDSS (Fukugita et al., 1996) to perform SED fitting (see Section 3.2 for details). Magnitudes for the five SDSS filters (u´g´r´i´z´ system; Smith et al. 2002) were drawn from the SDSS DR12 cross ID search[7] for our sample. All magnitudes in

---

[7]https://skyserver.sdss.org/dr12/en/tools/crossid/crossid.aspx

SDSS are given in the asinh magnitude system ([Lupton et al., 1999](#)). We use the composite model magnitude measurements that takes the best image fit of a linear combination of an exponential and de Vaucouleurs model to calculate the most reliable magnitude value of each source.

Table 2.3: Aparent SDSS u´g´r´i´z´ system magnitudes of the sample of local analogs.

Source	u′	g′	r′	i′	z′
J0021+0052	17.624±0.011	17.395±0.005	17.506±0.006	16.969±0.005	17.369±0.018
J0023−0948	18.514±0.026	17.550±0.006	17.882±0.010	17.531±0.011	17.340±0.050
J0136−0037	20.280±0.050	19.270±0.011	19.792±0.022	19.321±0.021	19.400±0.060
J0240−0828	19.474±0.033	18.992±0.012	19.586±0.021	18.453±0.011	19.660±0.110
J0252+0114	20.190±0.050	19.056±0.010	19.217±0.015	19.259±0.025	19.070±0.070
J0305+0040	20.600±0.070	19.920±0.016	19.765±0.018	19.287±0.019	19.480±0.080
J0950+0042	18.859±0.019	18.578±0.008	18.737±0.010	18.155±0.009	18.650±0.050
J1146+0053	20.480±0.060	19.416±0.012	20.045±0.033	19.595±0.027	19.500±0.080
J1226+0415	19.530±0.035	19.229±0.013	19.546±0.021	18.682±0.014	19.420±0.110
J1444+0409	20.510±0.100	19.411±0.012	20.310±0.040	20.330±0.050	19.470±0.300
J1448−0110	17.449±0.009	16.462±0.004	16.891±0.004	17.113±0.006	17.202±0.015
J1624−0022	17.214±0.008	16.537±0.003	16.890±0.004	16.878±0.005	16.817±0.013
J2101−0555	19.870±0.040	19.381±0.013	18.824±0.011	18.894±0.019	19.130±0.080
J2119+0052	19.446±0.035	18.079±0.007	17.995±0.008	17.843±0.010	18.530±0.060
J2212+0006	20.710±0.070	20.309±0.023	19.763±0.018	19.821±0.026	20.310±0.150
J2215+0002	19.690±0.040	19.148±0.010	19.404±0.017	18.623±0.012	19.100±0.110
J2225−0011	19.085±0.021	18.409±0.007	18.998±0.011	18.223±0.010	18.640±0.050
J2337−0010	20.090±0.060	19.273±0.011	19.722±0.019	19.014±0.015	19.490±0.130
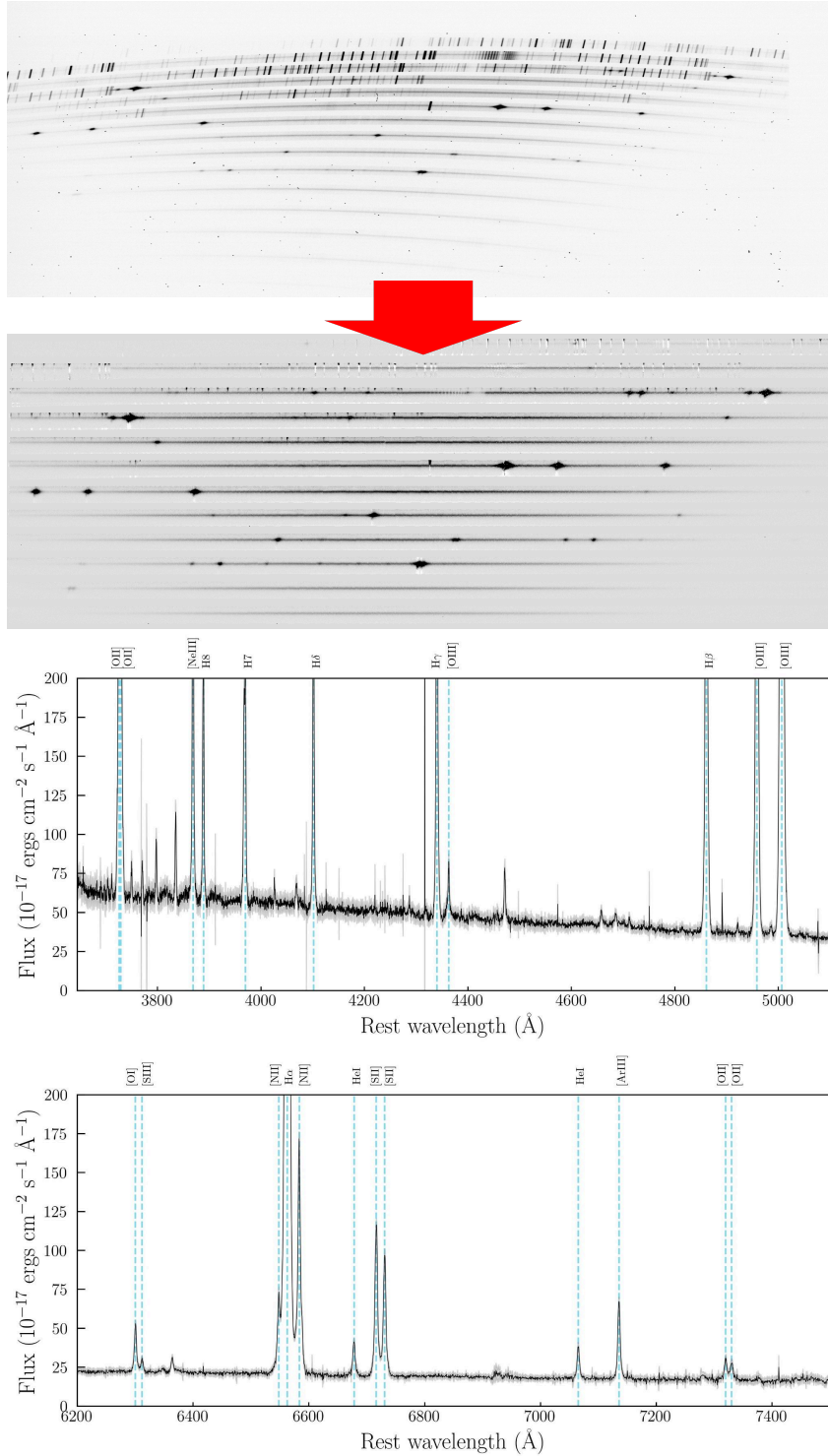
Figure 2.6: (*Top*) Raw and reduced 2D spectrum of J0021+0052. Images have 1×1 spatial and spectral binning and dimensions of the CCD are 2048×1024.(*Bottom*) 1D reduced and flux-calibrated spectrum of the same source. The errors of the binned pixels are shown at 3σ as shaded gray regions around the black spectrum. Blue vertical dashed and labeled lines indicate examples of emission lines involved in this study.

Chapter 3

Methods

In this chapter, we present the procedures followed to get the results of this research on metallicity calibrations and more. It is organized as follows: Section 3.1 describes how we corrected the spectra from extinction by dust in the Milky Way. In Section 3.2 we characterize the absorption features affecting Balmer emission lines through SED modeling of the photometry of our sample. Section 3.3 describe our model selection to fit emission lines and Section 3.4 the measurements of their fluxes. The correction by dust attenuation of each galaxy is explained in Section 3.5. We outline the equations to calculate the electron density and temperatures in Section 3.6, while the estimations of chemical abundances are detailed in Section 3.7. Finally, we list the ratios used to calibrate the chemical abundances in Section 3.8.

3.1 Galactic Dust Correction

The outcome of this project depends strongly on the method to estimate emission line fluxes because they are used to derive the physical quantities under study. More specifically, the properties of ionized gas such as electron temperature, electron density, and chemical abundances, depends on ratios of emission lines. Any source of contamination *unequally* modifying the value of emission lines involved in one ratio leads to mistrusted results. Correcting the data by any effect with such characteristics is then necessary to remove all systematics and get reliable estimates of the variables involved.

Optical light, and mostly blue bands, suffers from absorption and scatter by dust particles present in its path. This effect is determinant when analyzing quantities whose calculation depends on a ratio of emission lines with considerable separation in wavelength owing to the different behavior that dust have in different bands. For example, the electron temperature of the low-ionization zone T_e[O II] depends on the ratio of the [O II]$\lambda\lambda$7319,7330 doublet in the redder part of the spectra and the [O II]$\lambda\lambda$3726,3729 doublet in the bluer part (See Section 3.6 for details). This makes this temperature extremely sensitive to dust extinction.

Assuming there is little or no dust between the Milky Way and the galaxies observed, the absorption have place only when the light faces dust in the same field of the galaxies and when it goes through dust in the Milky Way. The flux correction by dust absorption inside the sample of local analogs is explained in Section 3.5. Here, we describe the procedure we adopted to account for the absorbed light by dust in the Milky Way.

In galaxy evolution studies, the dust absorption is widely characterized by the dust extinction curve. When the light crosses a dust cloud, its intensity can be described as the solution of the transfer equation:

$$I_\nu = I_\nu^0 \times e^{-\tau} \tag{3.1}$$

where τ is the optical depth and I_ν and I_ν^0 are the observed and intrinsic intensities of the light, respectively. The optical depth and the extinction curve are related by the expression

$$\tau_\lambda = 0.921 \cdot A(\lambda) = 0.921 \cdot E(B-V) \cdot k(\lambda) \tag{3.2}$$

where $A(\lambda)$ is the attenuation in magnitudes, $E(B-V)$ is the color-excess, and $k(\lambda)$ corresponds to the extinction curve, or being more precise, the attenuation law. Note that we make a distinction between *extinction* and *attenuation*. Extinction usually refers to the net light directly absorbed or scattered out of the line-of-sight by dust. One could think of it as the simple case of stellar light going through a dust cloud. On the other hand, attenuation holds for the averaged effect of having a complex distribution of stars/gas emitting light through non homogeneous dust clouds that lead to spatial differences in optical depth. This traduces in differential extinction with stars with little or no dust, stars embedded in dust clouds, or even the light that is scattered into the line-of-sight by the dust. There, the notion of extinction is too simplistic and attenuation refers more exactly to the averaged changes in the light. As we have spectra of galaxies that fall almost entirely in the slit, it is logical to assume that the light is rather attenuated than extincted. The attenuation by dust is then described by the attenuation law through a relation that can be noticed from Eq. 3.2:

$$A(\lambda) = E(B-V) \cdot k(\lambda) \tag{3.3}$$

The color-excess is interpreted as the thickness of the dust cloud or screen. Here, the attenuation in magnitudes as a function of wavelength is equal to the attenuation law in magnitudes as a function of wavelength weighted by the thickness of the dust cloud. Plugging Eq. 3.2 into Eq. 3.1, taking the natural logarithm and changing to base-10 logarithm, we get the expression that is widely used to account for the attenuated light by dust:

$$F_{\text{obs}}(\lambda) = F_{\text{int}}(\lambda) \times 10^{-0.4 \cdot E(B-V) \cdot k(\lambda)} \tag{3.4}$$

Or equivalently

$$F_{\text{int}}(\lambda) = F_{\text{obs}}(\lambda) \times 10^{0.4 \cdot E(B-V) \cdot k(\lambda)} \tag{3.5}$$

where $F_{\text{int}}(\lambda)$ and $F_{\text{obs}}(\lambda)$ are the intrinsic and observed flux in a certain wavelength λ, respectively. The notation on intensities is changed to put the variables into the context of this work. Since we are accounting for dust extinction in the Milky Way, we use the Milky Way extinction curve (Cardelli et al., 1989), and we query the point color-excess $E(B-V)$ of the line-of-sight of each galaxy using their SDSS coordinates on the Galactic Dust Reddening and Extinction tool of the NASA/IPAC Infrared Science Archive[1]. These numerical values are taken from the re-calibration provided by Schlafly and Finkbeiner (2011). Subsequently, we used the PyNeb (Luridiana et al., 2015) extinction correction tool giving $E(B-V)$ and the Milky Way extinction curve as input. PyNeb internally uses the formula from Eq. 3.4 to apply the correction.

Table 3.2 shows the values of the color-excess for the dust in the Milky Way. The sample has a very low median of $E(B-V)_{Gal} = 0.0472$. This suggest that the light passing through the Milky Way suffers from very low attenuation due to a thin cloud of gas. For a reference, the flux of Hβ in our sample has a percentage change ranging from 1.5% in the cases of less dust extinction to 8.8% for the highest color-excess. In Section 3.4, we take a deeper look into the effects that dust extinction can have in more sensitive physical quantities such as the T_e[O II] temperature.

3.2 SED Fitting & Balmer Absorption Correction

Apart from dust, internal processes in galaxies can cause big changes in the observed flux of specific emission lines. This is the case of the optical emission lines of the hydrogen atom: The Balmer series (Balmer, 1885). Balmer emission lines in galaxy spectra corresponds to the light emitted by the hydrogen atoms when a free electron captured through recombination jump down to the second energy level ($n \longrightarrow 2$, with $n \in \{3, 4, 5, ...\}$). The Balmer absorption, on the other hand, is an effect inherited from stellar spectra.

Figure 3.1 shows an example of stellar spectra from B to G type stars taken from Physics 230 Lecture Notes by Michael Richmond, RIT Observatory[2]. O and B-type stars are very hot ($T_{\text{eff}} \gtrsim 35000$K) and the hydrogen atoms in their atmospheres are mostly ionized by the radiation field and also excited by collisions. A minor fraction of the ionized hydrogen is able to recombine or de-excite to populate the first excited state ($n = 2$) which is the state that absorb photons with Balmer wavelengths and raise the absorption features in spectra, appearing very weak as we can see in the green spectrum of a B0 star in Figure 3.1. A-type

---

[1]https://irsa.ipac.caltech.edu/applications/DUST/
[2]http://spiff.rit.edu/classes/phys230/lectures/spec_interp/spec_interp.html
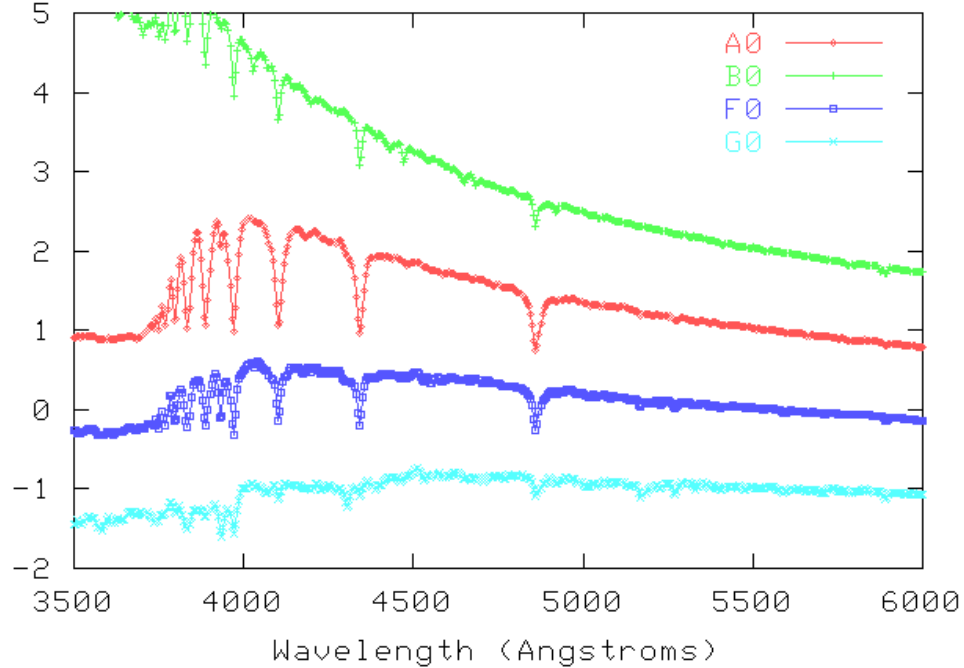
Figure 3.1: Sequence of stellar spectra from B0 to G0 stars taken from Physics 230 Lecture Notes by Michael Richmond, RIT Observatory. The green, red, blue, and light-blue markers represent spectra of B0 with $T_{eff} = 35000K$, A0 with $T_{eff} = 9500K$, F0 with $T_{eff} = 7300K$, and G0 with $T_{eff} = 5900K$, respectively. The absorption features observed at $\lambda < 5000$Å are the Balmer absorption lines starting by Hβ, Hγ and so on to lower wavelengths. The y-axis show the flux in relative units.

stars, instead, have a suitable temperature of $T_{eff} = 9500K$ to keep most of the hydrogen atoms in the $n = 2$ level and the absorption occurs more frequently leaving a stronger imprint in spectra as in the red spectrum of an A0 star in Figure 3.1. In the atmospheres of colder stars such as F0 ($T_{eff} = 7300K$) and G0 ($T_{eff} = 5900K$), most of the hydrogen remains in the ground state and they are not able to absorb much photons with Balmer wavelengths. This makes the absorption features to appear weaker again with respect to the stellar continuum as it can be seen in the blue (F0) and light-blue (G0) spectra of Figure 3.1. A-type stars are then the main contributors of the Balmer absorption and their presence in stellar populations can determine their strength. Our analogs should resemble, in principle, properties of relatively young systems due to their conditions reviewed by Bian et al. (2016) comparable to galaxies at $z \sim 2.3$ when the Universe was ~ 2.89 Gyrs old. Young stellar populations containing O and B-type stars are not expected to affect significantly the Balmer emission lines by their flatter absorption features. The emission from recombination and the Balmer absorption from the atmospheres of mainly A-type stars is combined and it translates in an underlying absorption in the integrated optical emission line spectra of galaxies, just like in our sample. Nevertheless, it is not possible to measure the absorption directly since the Balmer lines are so bright that can easily surpass the absorption feature and degenerate any attempt on constraining the flux from emission and absorption at the same time. To solve

this issue, we rely on estimates of the absorption lines from stellar population models.

Currently, several python-based packages can provide information of the stellar population of a galaxy by using their spectrum, photometry, or a mixture of both. Logically, having a spectrum would encourage us to use a pixel-weighted fitting method. However, these models do not work well in galaxies with prominent emission lines. Instead, they fit successfully spectra dominated by stellar emission. If one uses these packages, emission lines need to be masked out to not consider them in the fitting. In our case, this leaves a flat continuum with no stellar features and no kinematic information to fit, causing unreliable estimates of the stellar population even when providing prior knowledge of the redshift and kinematics of the source. For this reason, we use photometric data (See Section 2.5) to perform SED fitting and characterize the absorption of the Balmer lines from the best-fit stellar model. Although the objective of the SED fitting is to investigate the impact of the absorption, it provides valuable insight into the physical properties of the galaxies that are relevant for the case of study.

We follow a similar procedure than Shivaei et al. (2015). The SED modeling of the local analogs is made using the Code Investigating GALaxy Evolution (CIGALE[3]; Boquien et al., 2019). Our sample of analogs consist of star-forming galaxies with an important contribution in the blue bands. Indeed, manual examination of each spectrum shows an extremely low or practically no Balmer jump with flat to increasing continuum for $\lambda_{rest} < 3645$Å (Slightly appreciated in the 1D spectrum of Figure 2.6). Furthermore, the photometric data shows a relatively flat luminosity throughout filters. Although the photometry exhibit jumps in some optical bands due to the presence of bright emission lines, the SDSS u′ magnitude is considerably high to be at the base level of the rest of the filters (See Table 2.3 or Appendix A). Leveraging these characteristics, our expectations of galaxies dominated by a young stellar population are supported. This could be explained by a young galaxy or a galaxy with a recent burst of star-formation. For this reason, we decided to model our sample testing three different star-formation histories (SFHs):

1. Constant SFH with no age constraint (Model 1)

2. Constant SFH with age constrained to < 1 Gyr (Model 2)

3. Old stellar population with a late burst of star formation (10 Myr; Model 3)

Model 1 is an open run to check if the data admits a SFH against our expectations. Models 2 and 3 account for the options explained above: The constraint in model 2 is to fit a stellar population of a relatively young galaxy with ages < 1 Gyr. In model 3, galaxies with a mixture of an older stellar population and young stars from a late burst of star-formation are modeled, being the latter the population of stars dominating the emission spectra.

---

[3]https://cigale.lam.fr

For the three models described above, we used the Bruzual and Charlot (2003) stellar population models and a Chabrier (2003) initial mass function (IMF) with a metallicity grid of $Z = \{0.0004, 0.004, 0.02\}$, and 10 Myr of separation age between the young and old stellar populations. The separation age is only relevant when we use model 3 as it is the only case we have a dual stellar population. Every fit includes the contribution from nebular emission with grids of gas-phase metallicity of $Z_{gas} = \{0.0004, 0.004, 0.02\}$. The electron density is set to adopt all admitted values of the algorithm $n_e = \{10, 100, 1000\}$ cm^{-3} and the ionization parameter can take values between $\log(U) = \{-3.0, -2.0, -1.0\}$. Both fractions of escaping and absorbed Lyman continuum photons are set to have values of either 0.0 or 0.5. The width of emission lines is set to adopt values of 100km/s or 300km/s to account for possible broader emission as described in Section 3.3. The dust attenuation is fitted using the modified starburst dust attenuation model with the extinction curve of Calzetti et al. (2000). We use the default parameters of the dust attenuation, except for the reddening constant which we set to vary between $E(B - V) = \{0.03, 0.05, 0.1, 0.3\}$.
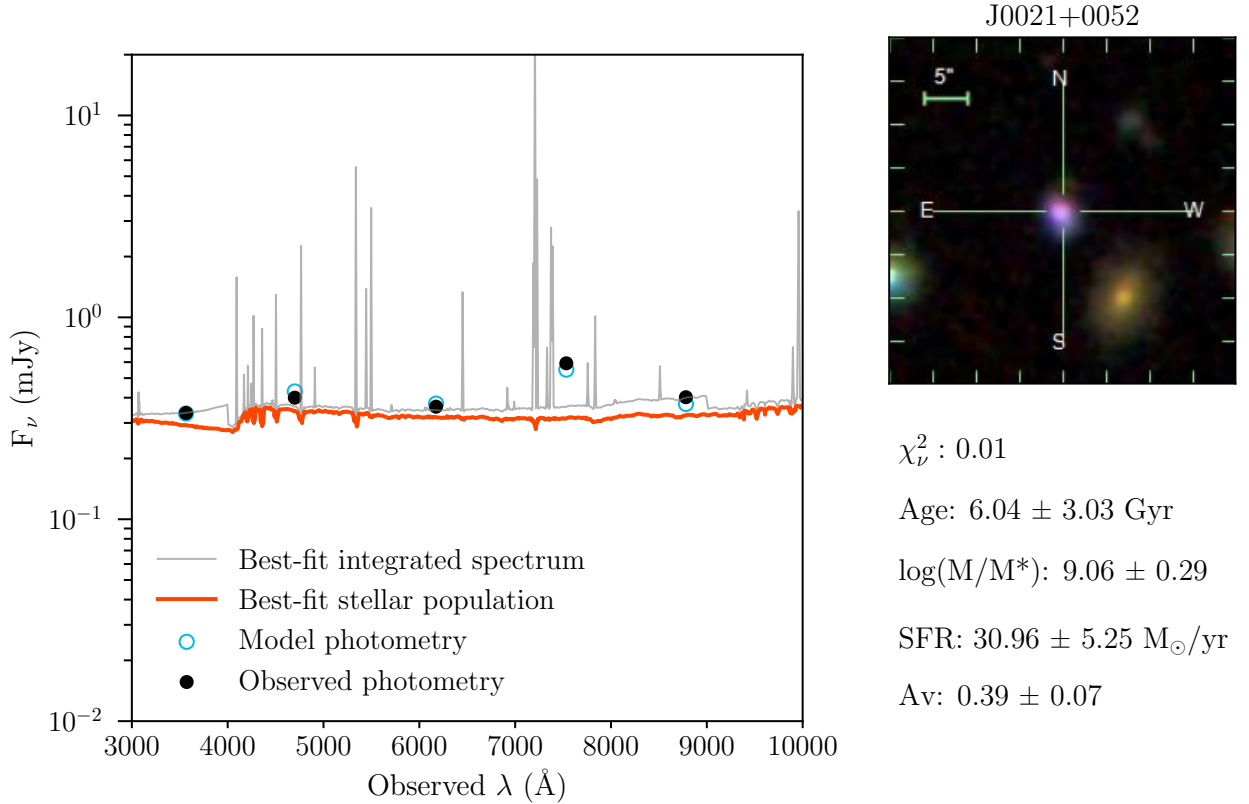
Figure 3.2: Example of the SED model of J0021+0052. (*Left*) Observed photometry represented as black dots and the photometry modeled by `CIGALE` as blue empty-circles. The y-axis is set in logarithmic scale and the flux is in mJy. The orange-red curve shows the emission from the best-fit stellar population, while the gray line marks the total best-fit spectrum model. (*Right*) SDSS stamp of J0021+0052 with some of the main properties estimated by the old stellar population model with late burst. Figures of the results of the SED modeling are in Appendix A.

To model the distinct SFHs, we use a delayed SFH model with optional exponential burst.

It is basically an exponential model with a control parameter τ of the rate of growth of the SFR which is the e-folding time (Time that the SFR increases by a factor of e at $t = \tau$). For model 1, we set 10^{10} Myr as the e-folding time to simulate a constant star-formation rate along with $f_{burst} = 0$ in CIGALE to neglect bursts of star-formation. The age of the stellar population can vary between 0.1, 0.5, 0.8, 1.0, 2.0, 5.0, 8.0, and 10.0 Gyr. For model 2, we use exactly the same configuration, but the stellar population can only have ages of 0.1, 0.5, 0.8, and 1.0 Gyr. The burst is only included in the case of model 3 that has an old stellar population with a recent burst of star-formation. As well as model 1, this model has a constant star formation activity, but with the difference of a restricted age of the stellar population above 2 Gyr and the late burst of star formation. The former is set to be recent with an age of 10 Myr to investigate how young stars dominate the photometry of the sample. The age of the stellar population in this case is set to vary between 2.0, 5.0, 8.0, and 10.0 Gyr. The e-folding time of the late starburst population model is the default 50 Myr, and the grid of fractions of mass injected to the burst is $f_{burst} = \{0.1, 0.3, 0.5, 0.7, 0.9\}$.

Figure 3.2 shows an example of the result from fitting the SED of J0021+0052 with the SFH of model 3. It can be noticed the close match between the observed and modeled photometry and the best-fit stellar population spectrum presents the Balmer absorption features that we aim to quantify. The total spectrum model given by CIGALE shows the prominent emission lines that causes some of the filters to lie above the rest, such as the SDSS i′ filter. The age of the stellar population is predicted to be quite old with 6.04 Gyr, but with a very high uncertainty of 3.03 Gyr. The model also predicts that J0021+0052 has a moderate stellar-mass of $10^{9.06}$ M$_\odot$ and it is actively forming stars at a rate of 30.95 ± 5.25 M$_\odot$/yr with low attenuation. This is an illustrative example and it is not representative for the whole sample of analogs.

Between some of the caveats of this procedure is the fact that only photometry is considered in this SED analysis. Only having photometry in optical bands is not enough to constrain very important features of the SFH of these galaxies reliably, such as the SFR. Additionally, without any information of the spectrum the code will not be able to distinguish which spectral features are the responsible of the flux observed in the filters near the nebular continuum breaks, such as the Balmer and Paschen breaks. This causes a degeneracy between the flux of the nebular continuum breaks and emission lines, they can compensate between each other and also put in question the veracity of this results. More sophisticated fits can be performed by including the spectra of our galaxies and searching for more bands covered in the literature for these sources, but we decided not to invest much more efforts on this topic as, although relevant, it is not the purpose of this work.

Figure 3.3 contain the most relevant physical parameters estimated from the three SFH scenarios proposed in this study. For Table with the specific values we refer the reader to Table A.1 of Appendix A. Logically, due to the expectations we imprint on model 2 all ages

31
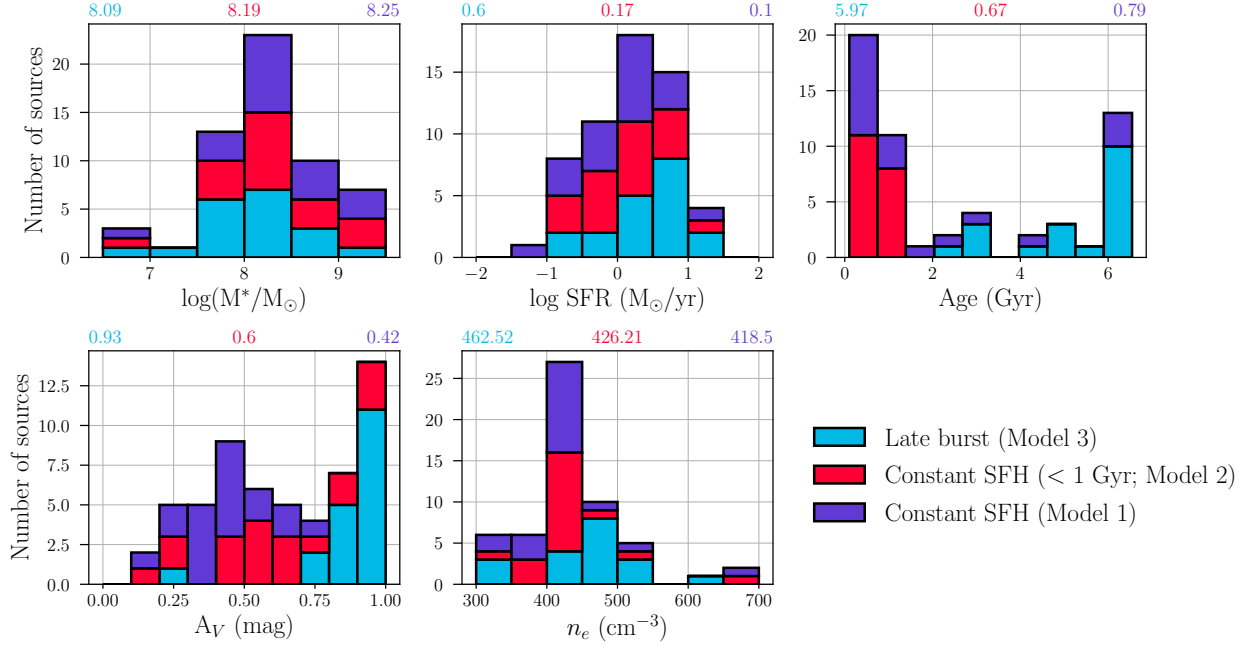
Figure 3.3: Bar-stacked histograms of the estimated physical properties from the SED fitting for Model 1 (constant SFH), Model 2 (constant SFH with age-constraint to less than 1 Gyr), and Model 3 (an old stellar population with late-burst). These are shown as purple, red, and blue histograms, respectively. Histograms of the stellar mass, instantaneous SFR, and mean age of the stellar population are shown, including the dust attenuation and electron density of the ionized gas. Above each panel the median of the sample is specified following the same colors of the histograms.

are between 0 and 1 Gyr with a median of $\sim$ 670 Myr shown in red color of the upper right-most panel of Figure 3.3. We note, however, that without applying any constraint on the age the constant SFH predicts that $\lesssim 50\%$ of the analogs have ages below 1 Gyr. This confirms our expectations on possible young stellar populations or young galaxies, but at the same time creates a dual sample of young and old galaxies with ongoing star-formation that would constitute the other $\gtrsim 50\%$. All SFHs predict that our galaxies populate the mass range of $\log(M^*/M_\odot) = 6.5 - 9.5$, show a very similar histogram shape, and medians of $\log(M^*/M_\odot) = 8.09$, 8.19, and 8.25. Regarding the star formation rate (SFR), models 1 and 2 have a very uniform distribution with almost the same amount of sources around SFR ~ 1 $M_\odot/\text{yr}$ (We remind the reader that Figure 3.3 shows bar-stacked histograms). Model 3 exhibit a slightly higher median SFR by 0.5 dex compared to the other models. The V-band attenuation in magnitudes of the is calculated using the reddening law $A_V = R_V \cdot E(B-V)$ with $R_V = 3.1$. We observe that the model 1 give the lowest attenuation values for the sample. The dust absorption and reddening is degenerated with the age of the galaxy since both play a role on determining the colors of each source. To reach redder colors in the photometry, one would either have older galaxies or higher dust content that scatter the blue light and make the galaxy look redder. This is precisely the effect that constraining the age has on the sample. We see that with model 2, the sample of galaxies before compatible with ages above 1 Gyr now need to be young, and therefore, they need higher dust attenuation

to explain their red magnitudes. This causes the red histogram to be more spread towards higher A_V with a median of 0.6 that is slightly higher than the 0.42 found in the unconstrained model. Additionally, there is a clear tendency to higher attenuation in model 3. As we model old galaxies, the contribution of the young stellar population to the age does not become significant unless the burst of star-formation dominates the photometry evidenced by the attenuation and SFR histograms where predicted values of model 3 are accumulated at higher values with respect to models 1 and 2. Finally, the estimated electron densities are considerably higher to electron densities in the local Universe where HII regions have around $n_e = 30$ cm^{-3} (Bian et al., 2016), and even higher than $z \sim 2.3$ galaxies with $n_e = 250$ cm^{-3} (Sanders et al., 2016). Regarding this study, this would be the first suggestion that our analogs are indeed good analogs that show values compatible with the selection criteria and electron densities that could trigger the shifts in the BPT-N2 diagram as discussed in Section 2.1. However, the electron density is poorly constrained as can be appreciated in the uncertainties in Table A.1. Uncertainties range between 400 and 500 cm^{-3} which opens the complete range of possibilities under 1000 cm^{-3} leading unreliable estimates. Furthermore, they are stuck in the upper limit allowed for the fit. This suggest that physical tracers of the ionization state of the ISM in our sample are not reliably constrained by the SED modeling and a fair comparison with high-z galaxies would need to be done with the $E(B-V)$ derived from emission line spectra. We revisit the discussion on electron densities and more ionization indicators in Section 4.1. Based on the best χ_ν^2 between SFHs, we decided to keep model 3 as the best model to fit our analogs. With this there are still sources with poor SED fitting such as the case of J2119+0052 being the most drastic with a $\chi_\nu^2 \sim 10.47$. Five galaxies show $\chi_\nu^2 > 1$, leaving 66.7% (12/18) cases with good fitting results demonstrated by their $\chi_\nu^2 \lesssim 1$, although some show extremely low values leading to overfitting. Values of the $E(B-V)_{\text{SED}}$ are included in Table 3.2 and are compared with the values estimated from the Balmer decrements analysis in Section 3.5.

By extracting the best-fit spectra of the stellar population composed by both young and old stars of model 3, we account for the Balmer absorption. At this point, our spectra is not corrected by slit loss, i.e., by the light that is not captured by slit spectroscopy. For this reason, the flux levels predicted by the SED fitting does not match our MagE flux calibrated spectra. Although the correction can be done, the absorption and emission has to be fitted anyway and it is more practical to compare the depth of the lines involved. Thus, instead of comparing direct fluxes we decided to quantify the absorption by studying the equivalent width of the lines. The equivalent width (EW) accounts for the strength of a spectral line (Carroll and Ostlie, 1996). Let F_c be the flux of the continuum level and F_λ the flux of the observed spectrum. The equivalent width is formally expressed as the integral of the *depth* of the line. The depth is calculated as the normalized difference between the flux of the actual spectrum and the continuum level. This leads to the equation

$$EW = \int \frac{F_c - F_\lambda}{F_c} d\lambda \tag{3.6}$$

Table 3.1: Equivalent width of emission and absorption lines of Hα and Hβ.

ID	EW(Hα)$_{em}$	EW(Hβ)$_{em}$	EW(Hα)$_{abs}$	EW(Hβ)$_{abs}$	Corr(Hα)[*] (%)	Corr(Hβ)[*] (%)
J0021+0052	500.1±1.5	98.6±0.4	3.21±0.20	5.1±0.9	0.641	5.203
J0023−0948	684±4	179.4±1.9	4.59±0.19	5.4±1.0	0.672	2.982
J0136−0037	487±6	120.2±2.0	4.97±0.23	6.8±1.0	1.021	5.652
J0240−0828	1046±10	329±5	3.75±0.20	4.1±0.9	0.358	1.236
J0252+0114	384±4	100.2±1.7	4.84±0.23	6.6±1.0	1.261	6.572
J0305+0040	336±4	85.1±1.5	5.08±0.23	6.9±1.0	1.515	8.106
J0950+0042	340.2±1.2	106.6±0.5	3.06±0.17	4.0±0.9	0.900	3.710
J1146+0053	584±8	148.3±2.0	4.61±0.19	5.4±1.0	0.790	3.620
J1226+0415	1039±6	216.3±1.5	4.67±0.24	6.2±1.1	0.449	2.870
J1444+0409	926±12	227±5	4.57±0.22	5.2±0.9	0.494	2.290
J1448−0110	706.1±1.9	151.4±0.6	4.25±0.19	4.5±0.9	0.601	2.996
J1624−0022	533±6	117.1±3.3	3.06±0.16	4.0±0.9	0.574	3.391
J2101−0555	491.7±3.5	121.2±1.1	5.04±0.21	6.0±1.2	1.024	4.988
J2119+0052	403.7±2.5	81.4±0.9	4.88±0.23	6.7±1.0	1.209	8.188
J2212+0006	522±9	122.2±3.1	4.81±0.20	5.2±1.0	0.921	4.216
J2215+0002	852±5	198.1±1.7	4.61±0.23	6.0±1.0	0.541	3.016
J2225−0011	676.7±3.3	157.2±1.1	4.96±0.25	6.6±1.1	0.734	4.202
J2337−0010	683±6	178.7±1.9	4.64±0.23	6.1±1.0	0.679	3.400

[*] Percentage flux correction for Hα and Hβ by Balmer absorption.

This integral represents a box of equal area than the covered by the absorption line. Such area can be approximated as the quotient between the flux of the line and the flux level of the stellar continuum that is a much simpler computation. Note that this integral gives positive values for absorption lines since $F_c > F_\lambda$ when λ belongs to the range of the lines. The calculation of the equivalent width for emission lines is analogous, although conceptually it would be the opposite of a depth. Table 3.1 show the equivalent widths of the emission lines measured using the spectra and the absorption lines of the SED modeling for Hα and Hβ. The steps we took to fit emission lines and estimate their fluxes are explained in Section 3.4. In average, the correction for Hα and Hβ are $\sim 0.80\%$ and 4.26%, making the effect of absorption quite negligible. Note that changing the model should not make a large difference in absorption, for instance, model 1 of constant SFH with no age constrain predict an average correction of $\sim 0.86\%$ and 5.3% for Hα and Hβ respectively. This result suggest that our galaxies are mainly dominated by young and hot stars such as O and B-type stars, expected by what we know about our galaxies, but it is still impressive to get such small corrections

despite choosing the SFHs giving the oldest ages of stellar population. Since the correction is so small, it is omitted in this analysis.

3.3   Model Testing for Emission Line Fitting

Measuring emission lines accurately is the most important step on calibrating metallicity with SELRs. Typically, emission lines are well described by single or multiple gaussian models. Multiple models are introduced when lines exhibit broad wings that cannot be accounted by a single gaussian. Adding more gaussian allow characterization of the flux in the wings and gives insight onto the kinematics of the gas. In cases such as in this work, spectra shows the integrated light coming from the whole or a considerable part of the source instead of a specific pointing of a sub-region. One has to be careful to not add too many gaussians and cause overfitting. It is a trade between using a mathematically correct model over a physically meaningful model that can account for the flux emitted by possible clouds of gas moving at different velocities. Furthermore, it opens the possibility of detecting inflow/outflow activity. We perform a model testing to emission lines to know whether broad components can affect our sample and to constraint precisely the fluxes.

The usual procedure to test the model is to choose a known bright line to fit. In star-forming galaxies, these could be either [O III]λ5007 or the Hα profile, or even one could split the analysis using both lines to model two groups of spectral lines with different ionization potentials (e.g. Hogarth et al. 2020). In this case, it is not convenient to use these lines since they both appear blended. Blended lines can bias the experiment by adding extra flux from an external line to the possible broad component of the line under study. In our sample, [O III]λ5007 has a broadened wing in the right side by the emergent HeIλ5015 and the Hα line is blended with the [N II]λ6548 and [N II]λ6584 lines. Thus, we decided to perform the model testing using the next brightest line without blending in our spectra: the [O III]λ4959 emission line.

We first try the simplest model: One single gaussian component. The left panel of Figure 3.4 shows the result of fitting only one gaussian to the bright [O III]λ4959 line of our example galaxy J0021+0052. All the parameters including the width, strength, and redshift of the line are set as free parameter. Although it is in log scale and the differences are exaggerated, the flux loss in the wings can be clearly appreciated by the best-model, even showing that the continuum level is overestimated. Furthermore, the bottom panel shows strong residuals that the model is not able to remove. This motivates the use of more gaussian components. We fit the lines two more times using a double and a triple gaussian model shown in the middle and right-most panels of Figure 3.4. Once more, the width, flux, and redshift of the multiple components are set as free parameters allowing them to not center at the same wavelength. We could add gaussian components until describing the line completely, but we need a limit
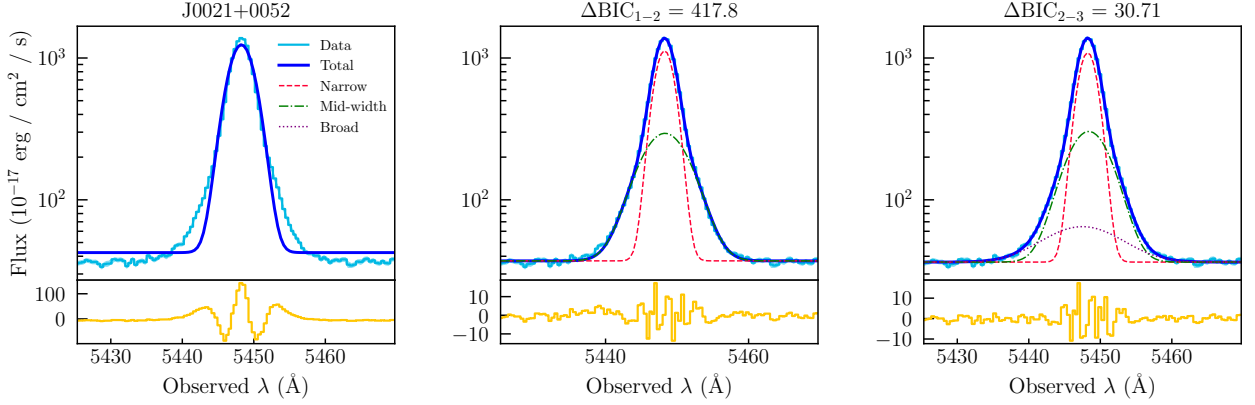
Figure 3.4: Multiple gaussian component test for J0021+0052. From left to right, each panel shows the result of fitting a single, double, and triple gaussian model to the [O III]$\lambda4959$ line. The spectrum is shown as light-blue steps. The red dashed line, green dashed-dotted line, and purple dotted line are the narrow, mid-width, and broad gaussian components, respectively. The total model composed by the sum of all gaussian components is described by the dark-blue curve. Below each panel, the residuals of the fit are shown as yellow steps. The numeric result of the BIC test is above the middle and right panels.

to avoid overfitting. For this purpose, we rely on the Bayesian Information Criterion (BIC; Schwarz 1978). As the name says, it is a criterion for model selection where lower values of the BIC are given to the preferred model. We use the estimate of BIC statistic given by the `LMFIT` class when fitting the emission lines. It is computed as:

$$\text{BIC} = N \ln(\chi^2/N) + k \ln(N) \tag{3.7}$$

where N is the number of data points, $\chi^2 = \sum_i^N (\text{Residual}_i)^2$ is the chi-squared statistic, and k is the number of free parameters. The BIC penalizes more complex models by giving linearly higher values scaling with the number of free parameters k. To calculate how significant is one model compared to others, we follow the methods described in Llerena et al. (2023) where they define a ΔBIC. According to such metric, if one calculates, for instance, the $\Delta\text{BIC} = \text{BIC}_{\text{single gaussian}} - \text{BIC}_{\text{double gaussian}}$, the single gaussian model is statistically preferred when $\Delta\text{BIC} < 2$, and the double component is more relevant when $\Delta\text{BIC} > 2$. We define ΔBIC_{1-2} and ΔBIC_{2-3} as the difference between the BIC of single vs double gaussians and double vs triple gaussians, respectively. Note that the definition of the BIC from `LMFIT` is different to the original, but a fast check comparing it with the true definition of the BIC suggest that both metrics give the same results in this analysis.

Table B.1 shows the result of the component test in the second and third column. All values of ΔBIC_{1-2} are exceedingly higher than 2 suggesting the model with double gaussians is better to fit the data. Except for J1146+0053 and J1444+0409, our galaxies also have $\Delta\text{BIC}_{2-3} > 2$ with J0136-0037 the closer to 2 with $\Delta\text{BIC}_{2-3} = 3.756$. J1146+0053 and J1444+0409 exhibit ΔBIC_{2-3} lower than 0. This indicates that the double gaussian model

has a lower BIC and it is statistically preferred against the triple gaussian model. Although $\sim 89\%$ of the sample admits the triple gaussian, we notice that the residuals of the fits are not significantly different from the residuals given by the double gaussian model (See Figure 3.4 of Appendix B). In the most critical cases, the range of the residuals change by 10^{-16} ergs/cm^2/s/Å, while the emission line flux is way above 10^{-15} ergs/cm^2/s/Å, leading to a flux loss of less than 10% between the double and triple gaussian model. Based on this, we decided to adopt the double gaussian model to describe the flux of emission lines in this work. Hereafter, the subscripts N and B symbolize the narrow and broad component, respectively.

3.4 Emission Line Fluxes

Finally, we are ready to measure the fluxes of the emission lines needed to estimate the properties of the ionized gas and heavy element abundances. As described in Section 3.3, we used a double-gaussian model for fitting the emission lines of all galaxies. In every double gaussian fit, the narrow component traces the center of the line and we use it to estimate the redshift of each source as it is reported in Table B.1. On the other hand, the broad component accounts for the flux in the wings of the lines and its velocity shift is only taken into account to replicate the model in the rest of the emission lines in every galaxy. In this section, we describe the procedure of measuring emission line fluxes and all the corrections involved.

In an homogeneously enriched ISM, one expects that emission from every fraction of the gas contributes to shape the emission lines if they are all captured by the slit. In our case, this assumption is reasonable since the sample consist of almost compact sources $(1'' - 2'')$ where the majority of the light is captured. This averages out the multiple gas components that could have place in the galaxy into a single emission line of each species in the 1D spectrum. Hence, we use the best-fit parameters of the [O III]λ4959 line fitting from the component test to fix the shape of the lines in the entire spectrum of each galaxy. For this, we first fit the [O III]λ4959 with all free parameters as in the model testing. Subsequently, we calculate the Doppler shift between the narrow and broad component using their respective estimated redshift z_N and z_B. The shift is calculated as

$$\Delta v = c \cdot \frac{z_B - z_N}{1 + z_N} \tag{3.8}$$

where c is the speed of light. We further correct the width of the best-fit narrow and broad components by the instrumental broadening. The observed width of emission lines is not only determined by the distribution of velocities of the gas, but also contains contribution from the instrument we are using. Such contribution depends on the resolution (R) of the spectrograph. If the resolution is uniform throughout the spectra, the dispersion of the instrument can be estimated as $\Delta\lambda = \lambda/R$ in Åand this can be used to estimate the broadening for all lines. In our case, echelle spectra have a line spread function that varies

with wavelength, where redder orders detect wider lines. Due to this, we need to account for these wavelength variations and correct the widths depending on the wavelength of the line we are fitting so that the correction is consistent with the characteristics of the spectra. The reduction pipeline provides an arc spectrum that was used for the wavelength calibration of each night. From this spectrum, we fit single gaussians to arc lines lying in the same wavelength range that the emission lines we are correcting. Unlike emission lines in the spectra, arc lines were well fitted by single gaussians which supports the idea that the broadening of the emission lines in our data could have a physical origin. For example, if we need to account for intrinsic broadening of J0021+0052 that has a $z \sim 0.099$, we fit the [O III]λ4959 line and the nearest arc line to the observed wavelength 4959Å $\times$ $(1 + 0.099) \sim 5450$Å. The width of arc and sky lines are typically around 10 km/s which is really low, meaning that the measured width of these lines can be considered as pure instrumental broadening with 69.7 km/s being the average width of the nights at 4959Å rest-frame. The only exception is the night of 2019B which had the worst conditions with a measured instrumental broadening of 106.8 km/s, that if considered in the average we should report 78.9 km/s. The width of the arc line then is quadratically subtracted to the observed width of the narrow and broad components of [O III]λ4959 through the formula:

$$\sigma_{\text{int}} = \sqrt{\sigma_{\text{obs}}^2 - \sigma_{\text{inst}}^2} \tag{3.9}$$

where σ_{inst} is the instrumental broadening, σ_{obs} the measured width of the lines, and σ_{int} the intrinsic broadening corresponding to the real width of the lines. Once we measure the intrinsic width, whenever we fit another emission line we need to estimate the instrumental broadening at its wavelength and add it quadratically to the intrinsic velocity dispersion of the galaxy. To speed up the process, we estimated the width of arc lines lying at the same wavelength than all the set of emission lines fitted for one guide galaxy in each observation run. We then fit a linear relation to extract the arc line width as a function of wavelength for each observation run. The guide galaxies of each night were J0021+0052 for 2018B, J0950+0042 for 2019A, J0136-0037 for 2019B, and J0023-0948 for 2023A. We found the following linear relations:

$$\sigma(\lambda) = \begin{cases} 9.42 \cdot 10^{-5} \cdot \lambda + 0.03, & \text{for 2018B} \\ 9.14 \cdot 10^{-5} \cdot \lambda + 0.04, & \text{for 2019A} \\ 1.61 \cdot 10^{-4} \cdot \lambda - 0.05, & \text{for 2019B} \\ 1.02 \cdot 10^{-4} \cdot \lambda - 0.03, & \text{for 2023A} \end{cases}$$

where $\sigma(\lambda)$ is the instrumental broadening and λ the wavelength, both in units of Å. If σ_{line} is the width of a gaussian component of an emission line at λ, we use the previous function to estimate it as follows:

$$\sigma_{\text{line}}^2 = \sigma_{\text{int}}^2 + \sigma^2(\lambda) \tag{3.10}$$

This correction applies to the narrow and broad component in the same way. Table B.1 contains the redshift of the source traced by the narrow component (z_N), the Doppler shift (Δv) between gaussian components, and their FWHM corrected by instrumental broadening. The redshift is very consistent with the values provided by SDSS (See Table 2.1). The results of the Doppler shift and the FWHM of the components make us omit the investigation of a complex kinematics in our emission lines. First of all, although gas flows might have implications on the chemical abundances of our galaxies since part of the material can be expelled through outflows or accreted from enriched gas, characterizing this effect is far from being the objective of this work. Secondly, the spectral resolution of MagE with the 1″ slit is ~ 73 km/s ($R \sim 4100$). This means that our data is not sensitive to lower changes in velocity than 73 km/s. The highest measured Doppler shift is -32.7 ± 3.5, that could be considered as a perturbation seen by the spectrograph, but cannot be confirmed as an outflow, for instance, with our resolution. Furthermore, the values of corrected FWHM as it can be appreciated in Table B.1 indicate that 38.9% (7/18) of our sample shows a FWHM of the narrow component lower than the spectral resolution of the instrument and 22.2 % (4/18) have or nearly have 73 km/s, which is consistent with rotation velocities of low-mass galaxies (See Downing and Oman 2023 for a reference on velocities of low-mass systems). This means that the lines are not broad enough to carry out a kinematic analysis of gas flows. Actually, there are cases where the narrow component had a lower width than the intrinsic broadening of the instrument such as in J0252+0114 and J1146+0053, or drastic cases like J2101-0555 where we measure an intrinsic broadening corrected narrow component velocity of 11 ± 25 km/s which is can be considered unreal. This does not contradict our model selection, but it takes away the option to make metallicity studies differentiated by kinematics. It is still necessary to keep using the double gaussian model to account for the full flux of the emission lines and this is the reason why we keep it in our analysis. Since the method failed for J0252-0114 and J1146+0053 because the measured narrow component was thinner than the instrumental broadening we used the instrumental width for the unresolved narrow component of those lines.

Knowing the intrinsic broadening and the Doppler shift between the narrow and broad components from fitting [O III]λ4959 in each galaxy, we fix these values to the rest of the emission lines. This leaves the fluxes as a free parameter, but we also decided to let the z_N parameter free to account for any small variations in the center of the lines while we fixed the relation with z_B by the Doppler shift. We do not apply any other theoretical restriction than the relation [N II]λ6584 $\sim 3\times$ [N II]λ6548 to decrease the amount of parameters when fitting the Hα profile. All the fits to the emission lines presented in this manuscript consist of an exploration of the parameter space made with the `emcee` method of minimization from the package: Non-Linear Least-Squares Minimization and Curve-Fitting for Python (LM-FIT; Newville et al. 2015). Regardless of the amount of parameters, we use 100 walkers with chains of 2500 steps long and accept values every 10 steps. By burning 1500 steps, the regions sampled in the parameter space were clear enough with flat chains of (2500 - 1500) $\times$ 100 /
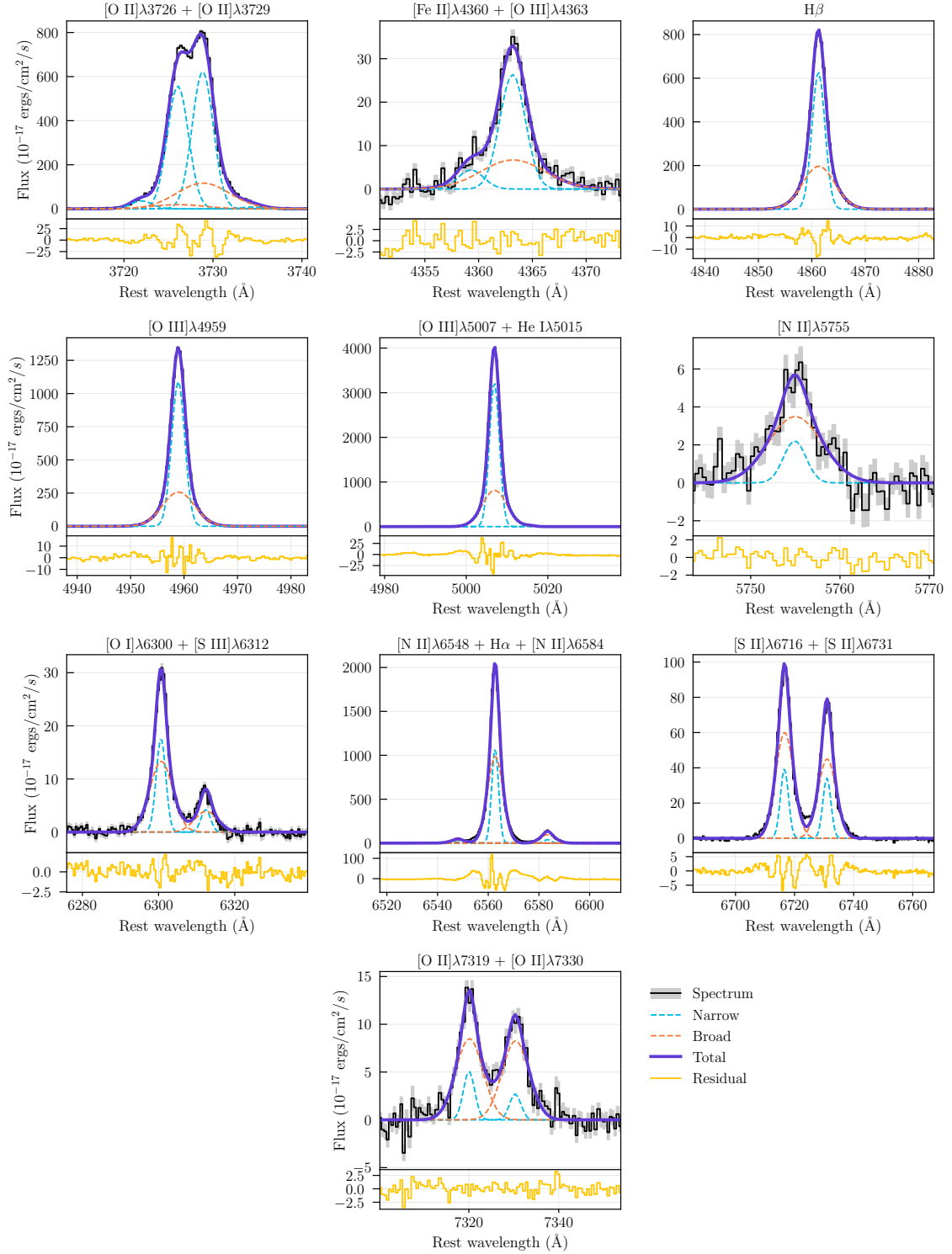
Figure 3.5: Fit results of the most relevant emission lines in this study ordered by wavelength for J0021+0052. The black solid line with gray shaded errorbars represents the spectrum. The solid purple line is the total model composed by the narrow and the broad components shown as dashed blue and orange lines, respectively. Below each plot, the residuals are shown as yellow steps.

10 = 10000 steps long for each parameter. The chains of the narrow and broad components of each emission line define a distribution of compatible solutions with our data. We take the mean and standard deviation of these distributions to get the emission line fluxes and divided them by the flux of the Hβ line as presented in Table D.1.

Figure 3.5 shows examples of emission line fitting results for J0021+0052. Here, excellent measurements of the brightest lines such as [O III]λ5007, [O III]λ4959, Hα, and Hβ can be appreciated. We emphasize the remarkable quality of our fits by observing how the narrow and broad components are able to encapsulate the information on the shape of the line profiles by measuring their emission line flux accurately and leaving small enough residuals. Even in the fainter lines the models are detailed enough to allow distinguishing their shape and giving good measurements on some of the crucial lines involved in the calculations of chemical abundances, such as the [O III]λ4363, [N II]λ5755, and the [O II] and [S II] doublets.

3.5   Dust Attenuation Correction

The last correction we must apply before using the emission line fluxes to derive metallicities and calibrate empirical relations with SELRs is the extinction by dust present in the ISM of our sources. Dust consist on silicate, ice, and carbonaceous grains that can have sizes up to the order of microns. The origin of dust in the ISM is still uncertain. It is proposed to come mainly from the feedback of AGB stars (Höfner and Olofsson, 2018) and cool supernovae ejecta (Matsuura et al., 2015), although more mechanisms are currently being explored. The dust is very effective on scattering the blue light, and hence, any analysis made on physical quantities derived from the blue and UV bands is affected by the dust content. In our case, the dust correction is critical for the [O II]λ3726,3729 doublet that is used to trace one of the electron temperatures T$_e$[O II] (See Section 3.6).

Eq. 3.4 describes how the correction by dust has to be applied to the observed fluxes to get the intrinsic measurement of the intensity of an emission line. As in Section 3.1, to know the real flux emitted by the galaxy we need the color-excess $E(B - V)$ and the extinction curve $k(\lambda)$. In this case, the color-excess cannot be estimated from archive data because it varies from galaxy to galaxy. Furthermore, the extinction curve is not always the same and it can differ depending on the source. Modeling these quantities is interesting by itself to characterize the shape of the dust extinction curve in star-forming galaxies at high-z. Such task does not align with the objectives of this project, thus, we limit the analysis to the results of $E(B - V)$ by adopting typical assumptions on the extinction curve and hydrogen emission lines. To characterize the dust attenuation as a function of wavelength we use the Calzetti et al. (2000) extinction curve:

$$k_{cal}(\lambda) = \begin{cases} 2.659(-1.857 + 1.040/\lambda) + R_V, & \text{if } \lambda \geq 0.63\mu m \\ 2.659(-2.156 + 1.509/\lambda - 0.198/\lambda^2 + 0.011/\lambda^3) + R_V, & \text{if } \lambda < 0.63\mu m \end{cases}$$

where $R_V = A_V/E(B-V) = 4.05$ for starburst galaxies. To estimate $E(B-V)$ from Eq. 3.4, we would need the intrinsic values of the fluxes, but they cannot be obtained directly since the actually need a value for $E(B-V)$, which is exactly what we are trying to estimate. Notwithstanding, we can extract information by taking ratios of the extinction correction equation evaluated in different hydrogen lines. If we take Eq. 3.5 evaluated in Hα and divide it by the same equation evaluated in Hβ we get

$$\frac{F_{H\alpha}^{int}}{F_{H\beta}^{int}} = \frac{F_{H\alpha}^{obs}}{F_{H\beta}^{obs}} \times 10^{0.4E(B-V)(k(\lambda_{H\alpha})-k(\lambda_{H\beta}))} \tag{3.11}$$

or equivalently

$$\frac{F_{H\alpha}^{obs}}{F_{H\beta}^{obs}} = \frac{F_{H\alpha}^{int}}{F_{H\beta}^{int}} \times 10^{-0.4E(B-V)(k(\lambda_{H\alpha})-k(\lambda_{H\beta}))} \tag{3.12}$$

Defining the ratios of Balmer lines as $R_{int}^{\alpha\beta} = \frac{F_{H\alpha}^{int}}{F_{H\beta}^{int}}$, and $R_{obs}^{\alpha\beta} = \frac{F_{H\alpha}^{obs}}{F_{H\beta}^{obs}}$, Eq. 3.12 turns to

$$R_{obs}^{\alpha\beta} = R_{int}^{\alpha\beta} \times 10^{-0.4E(B-V)(k(\lambda_{H\alpha})-k(\lambda_{H\beta}))} \tag{3.13}$$

Eq. 3.13 states that by adopting an extinction curve and knowing the intrinsic and observed ratios of Balmer lines we can estimate $E(B-V)$. Indeed, the observed ratios between Balmer line fluxes are measured from our spectra, while the intrinsic ratios depend on the recombination scheme assumed. In HII regions, the heavy elements are just a fraction of the gas surrounding stars. The gas is mainly composed by hydrogen and helium. Ionized hydrogen can recombine with free electrons which cascade down to lower energy levels and emitting photons in the process. Recombination to the the energy level $n = 1$ produces Lyman emission that can interact with other H atoms. If the nebulae are optically thin, this emission can escape without further difficulties in what is called the Case A recombination. Instead, if the nebulae are optically thick the Lyman emission from recombination interacts with other hydrogen atoms through resonance scattering. In such case, the emission of Lyman photons is obscured and only the Balmer emission escapes from the region. This is the Case B recombination scheme and it is usually the adopted in HII regions of star-forming galaxies. For a given recombination scenario, electron density and temperature, the intrinsic ratios of Balmer lines are known. We follow this procedure to calculate the ratio between intrinsic and observed ratios of Balmer lines, i.e., the Balmer decrements.

We assume the ISM in our galaxies is under case B recombination with an electron density of $n_e = 100$ cm^{-3} and electron temperature of T$_e = 10000$K. The intrinsic ratios of Balmer

lines with respect to Hβ represented by $R_{\text{int}}^{\lambda\beta}$ are drawn from Storey and Hummer (1995) and are shown in the first row of Table C.1. Despite these values are quite standard for star-forming regions, they are not absolute, as varying the electron density, temperature, and recombination case would give different intrinsic ratios. Once we have the intrinsic ratios, Eq. 3.13 can be worked out to define a linear function of the extinction. Let's generalize the equation by adopting any Balmer line at λ, not necessarily Hα. Dividing by $R_{\text{obs}}^{\lambda\beta}$ and taking logarithm, this gives

$$Y = -0.4 \cdot E(B-V) \cdot X \tag{3.14}$$

where $Y = \log(R_{\text{obs}}^{\lambda\beta}/R_{\text{int}}^{\lambda\beta})$ and $X = k(\lambda) - k(\lambda_{\text{H}\beta})$ are the independent variables that can be measured after the assumptions previously described. With a set of ratios of Balmer emission lines we can fit Eq. 3.14 and get the reddening constant $E(B-V)$. We then measure the Balmer decrements for Hα, Hβ, Hγ, and Hδ by using their emission line fluxes and intrinsic ratios with respect to Hβ. The results of these measurements are shown in Table C.1. The variable X is drawn by simply evaluating the Calzetti et al. (2000) extinction curve for the corresponding wavelength of the Balmer lines. We fit a linear function with no intercept and estimate the reddening constant from the best-fit slope (See Appendix A for plots of the fit to the Balmer decrements). Estimated values of the extinction are shown in Table 3.2 and analyzed in Chapter 4.

An important thing to notice is that, 22% of the sample (4/18) shows unphysical results for the Balmer decrements. This is the case of J0252+0114, J1226+0415, 1444+0409, and J1448-0110. They all present negative values for $E(B-V)$ in Table 3.2 as a consequence of inconsistent Balmer decrements. In particular, all these galaxies show Hα/Hβ < 2.86 (See Table C.1). The reasons for finding lower values than the intrinsic ratios is still under debate and the problem seems to lie on the assumption that Balmer emission does not suffer from self-absorption, causing an Hα flux loss depending on the thickness and symmetry of the cloud that we are not considering (Scarlata et al., 2024). Even when assuming other configurations of electron temperature and density, the intrinsic ratios do not vary enough to lie below the observed ratios of these galaxies. We take advantage of the results of extinction by noticing that the values are really low, even closer to 0 in the cases where the reddening constant results negative. Therefore, we decided to perform the dust correction only to galaxies with physically consistent line ratios, while no dust correction is applied to the problematic sources. The objective of this project is not to solve such issue, so the methods adopted in this work are faithful to the standards and the practic way to procedure up to date.

Table 3.2: Color-excess for attenuation by Galactic dust and dust in the galaxies.

ID	$E(B-V)_{\text{Gal}}$	$E(B-V)_{\text{SED}}$	$E(B-V)$
J0021+0052	0.0212±0.0008	0.29±0.05	0.1240±0.0026
J0023−0948	0.0422±0.0013	0.3000±0.0011	0.11±0.07
J0136−0037	0.0242±0.0010	0.300±0.006	0.070±0.008
J0240−0828	0.0263±0.0009	0.25±0.09	0.119±0.004
J0252+0114	0.0580±0.0033	0.3000±0.0006	$\lesssim 0$
J0305+0040	0.0671±0.0015	0.3000±0.0004	0.170±0.010
J0950+0042	0.0475±0.0014	0.28±0.06	0.3113±0.0034
J1146+0053	0.0210±0.0008	0.299±0.012	0.19±0.10
J1226+0415	0.0158±0.0006	0.26±0.09	$\lesssim 0$
J1444+0409	0.0266±0.0007	0.09±0.08	$\lesssim 0$
J1448−0110	0.0469±0.0015	0.27±0.08	$\lesssim 0$
J1624−0022	0.0771±0.0023	0.27±0.07	0.066±0.009
J2101−0555	0.0487±0.0019	0.300±0.008	0.081±0.004
J2119+0052	0.0680±0.0030	0.30000±0.00005	0.096±0.007
J2212+0006	0.0501±0.0020	0.29±0.05	0.127±0.010
J2215+0002	0.0644±0.0019	0.299±0.017	0.0791±0.0034
J2225−0011	0.0640±0.0034	0.295±0.032	0.058±0.004
J2337−0010	0.0323±0.0010	0.299±0.016	0.122±0.004

$E(B-V)_{\text{Gal}}$: Color-excess by Galactic dust from Schlafly and Finkbeiner (2011).
$E(B-V)_{\text{SED}}$: Color-excess of the gas estimated from the SED fitting.
$E(B-V)$: Color-excess of the gas derived from Balmer decrements with the Calzetti et al. (2000) extinction curve.

3.6 Electron Density & Temperatures

This Section and Section 3.7 describe the formulas of the direct-T_e method that we used to calculate all the physical quantities under study based on the tutorial of Pérez-Montero (2017). Equations to calculate temperature and density on this section are directly taken from the latter article and represent analytical fits to grids of photoionization models calculated using PyNeb. The direct-T_e receives its name from the fact that the electron temperature T_e is calculated directly from the values of optical line fluxes instead of using calibrations based on strong emission lines. It takes advantage from the dependencies of emission line ratios on density and temperature. Indeed, the Boltzmann equation of thermodynamic equilibrium states that the relative amount of atoms in two different excited states is given by

$$\frac{n_i}{n_j} = \frac{\omega_i}{\omega_j} \exp(-\chi/kT) \tag{3.15}$$

where n_i and n_j are the number density of atoms in the excited states i and j, respectively, ω_i and ω_j are the statistical weights, χ is the energy difference between the states, k is

the Boltzmann constant and, T the temperature. The observed flux of a collisionally excited line (CEL) is directly proportional to the number density of ions in the excited state that produces the line. The number density of atoms in an excited state depends on temperature and density, since the temperature set the energy of the electrons that are able to excite ions and the more dense the nebula is, the more important is collisional de-excitation. The combined effect of temperature and density translates to the emission lines we observe in nebular spectra and the lines inherit the properties of their original atoms. According to this, the ratio of emission line flux of two different excited states is sensitive to the electron temperature and density (Osterbrock and Ferland, 2006) depending on which lines we use.

Before going through the calculations of the direct-T_e method, some assumptions need to be made on the ionization structure of nebulae. A nebula can be divided by zones based on different ionization degrees. Up to date, the possibility of establishing a four-zone model is being explored by analysis of extreme emission line galaxies (Berg et al., 2021), but these include the use of UV emission lines. Due to our limitations and the focus of our study, we adopt the widely used framework proposed by Garnett (1992) where the gas is divided into three regions: i) The *low-ionization* zone for species such as O^+ and N^+, ii) The *intermediate-ionization* zone for ions such as S^{2+} and Ar^{2+}, and iii) The *high-ionization* zone for O^{2+} and Ne^{2+}-like ions. Each of these regions have a different electron temperature traced by CELs of their representative ion species. Note that the complete scheme presented in this chapter is to calculate density, temperature and abundances of HII regions and we are applying everything to entire galaxies as if they were a giant HII region. The differences between analyzing the integrated light of an entire body instead of a spatial analysis of the chemical abundances of the sources escapes the scope of this work.

The first variable we can constrain independently is the electron temperature of the high-ionization zone. This temperature is traced by the ratio

$$R_{O3} = \frac{I(\lambda 4959) + I(\lambda 5007)}{I(\lambda 4363)} \tag{3.16}$$

where $I(\lambda)$ is the intensity of the line at wavelength λ. The electron temperature is then calculated as follows

$$T_e[\text{O III}] = 0.784 - 1.357 \cdot 10^{-4} \cdot R_{O3} + \frac{48.44}{R_{O3}} \tag{3.17}$$

Note that this temperature is determined *independently* of any other physical parameter of the ISM of our galaxies. As discussed previously, the ratio of emission lines depends on temperature and density. However, the R_{O3} ratio is more sensitive to temperature than density. A line produced by downward transitions from an excited state of higher energy would require more energetic photons to reach such excitation from the ground level compared to lines produced by a lower-level excited state. For instance, [O III]$\lambda 4363$ and [O

III]λ5007 are produced by downward transitions from different collisionally excited states of the oxygen atom. The same oxygen atom in the ground level will require more energy to get excited to the level that triggers [O III]λ4363 than exciting the atom to the level that triggers [O III]λ5007. Therefore, the relative rate at which these optical [O III] lines occur (In other words, the ratio between these lines) is directly related to the energy distribution of the free electrons responsible of the excitation, i.e., the temperature. The convenient use of these lines define the R_{O3} ratio and allow constraining the electron temperature. The contribution of the density exist, as more dense regions lead to more particle interactions that could excite and de-excite the electrons in the ions, but there is no use if the electrons have insufficient energy for such task. A family of relations similar to Eq. 3.17 have place for different electron densities and collision strengths. The relation we outline here assume that the nebula has $n_e = 100$ cm^{-3} but changes in density for the temperature range are negligible (Pérez-Montero, 2017). For details on the models and collision strengths used please refer to Pérez-Montero (2017). Although the electron density it is a property that we must constrain, this assumption is good enough since it is around the typical value of HII regions found in local galaxies (Bian et al., 2016) and as long as changes in the density below 5000 cm^{-3} are made (Far above the ranges of density of HII regions) the temperature calculated from R_{O3} will not suffer significant changes (Nicholls et al., 2020). Eq. 3.17 give temperatures in units of 10^4K and are the units we use in this study.

The temperature of the intermediate-ionization zone is estimated from emission lines of the sulfur S^{2+} ion. For this temperature, we have the ratio

$$R_{S3} = \frac{I(\lambda9532) + I(\lambda9069)}{I(\lambda6312)} \tag{3.18}$$

and the temperature

$$\mathrm{T}_e[\mathrm{S\ III}] = 0.5147 + 3.187 \cdot 10^{-4} \cdot R_{S3} + \frac{23.64041}{R_{S3}} \tag{3.19}$$

The reasoning behind the lines used in the R_{S3} ratio is the same than for the R_{O3}, lines of the same atomic species with considerable differences in excitation energy are sensitive to temperature. The [S III]λ6312 is detected in all our sample with good S/N and resolution along the [O I]λ6300 line. Nevertheless, the [S III]λ9532 and [S III]λ9069 lines are in the near infrared where combined with the redshift of our sources they lie in the far red extreme of our spectra. Although noisy, we are still able to detect them with good S/N in most of the cases, except for J0950+0042 and J1146+0053 that have sky contamination in the wavelengths of the lines making them impossible to constraint accurately. J2101-0555 and J2212+0006 have $z > 0.15$, shifting these two lines out of the MagE wavelength coverage so we do not report measurements of the intermediate-ionization zone temperature for these two sources either. This leaves a total of 77.8% (14/18) of our sample that has measurements of T$_e$[S III].

The temperature of the low-ionization zone is traced by the O^+ ion. The only caveat on calculating T_e[O II] is that it has a non-negligible density dependence. Ideally, one would estimate the temperature of this zone avoiding the dependence on density by using emission lines of the N^+ ion. Nevertheless, the characteristics of our spectra allow us to estimate T_e[O II] for all sources, in contrast to T_e[N II] due to the lack of detections of the faint auroral [N II]$\lambda 5755$ line in our sample. As a representation of the low-ionization zone, it is usually assumed that T_e[N II] $\sim T_e$[O II] due to their similar ionization potentials (29.6eV and 35.1eV, respectively; Kramida et al. 2023). The procedure to calculate T_e[N II] is at the end of this section. We use then the T_e[O II] temperature as a tracer of the low-ionization line addressing carefully its relation with the density. To explain our procedure, it is first necessary to outline how the electron density must be calculated.

Pérez-Montero (2017) suggest the use of S^+ lines which as the usual procedure to constrain the electron density. In this case, the ratio of sulfur lines is defined as

$$R_{S2} = \frac{I(\lambda 6716)}{I(\lambda 6731)} \tag{3.20}$$

and the use of the ratio to calculate the electron density in units of cm^{-3} is

$$n_e[\text{S II}] = 10^3 \cdot \frac{R_{S2} \cdot a_0(t) + a_1(t)}{R_{S2} \cdot b_0(t) + b_1(t)} \tag{3.21}$$

The coefficients of the linear form in the numerator and denominator presented are

$$
\begin{aligned}
a_0(t) &= 16.054 - \frac{7.79}{t} - 11.32 \cdot t \\
a_1(t) &= -22.66 + \frac{11.08}{t} + 16.02 \cdot t \\
b_0(t) &= -21.61 + \frac{11.89}{t} + 14.59 \cdot t \\
b_1(t) &= 9.17 - \frac{5.09}{t} - 6.18 \cdot t
\end{aligned}
\tag{3.22}
$$

where t is an electron temperature. Here it can be noticed that the electron density depends on the ratio of [S II] lines. The lines in question belong to the doublet [S II]$\lambda\lambda 6716,6731$. The flux ratio between two lines of the same atom species with similar excitation energies (like doublets) only will be set by the rate at which these lines are de-excited through collisions. Therefore, they are defined by the ratio of transition probabilities of the lines in the doublet which is determined by the electron density that rules the number of interactions. Another example of doublet that can be used for this is the [O II]$\lambda\lambda 3726,3729$ through the ratio $I(\lambda 3729)/I(\lambda 3726)$ (Osterbrock and Ferland, 2006). These ratios are used to be more sensitive to density variations but the temperature dependency is not negligible. Pérez-Montero (2017) states that $t = T_e$[O III] is generally used, but determining the electron

density iteratively with a similar ion than S$^+$ is also possible. The T$_e$[S II] electron temperature can be used with such purpose, but in our case we do not have good detections of the [S II]$\lambda\lambda$4068,4076 lines necessary for its calculation. Therefore, we use the formulae of n_e[S II] and T$_e$[O II] to simultaneously determine them as the electron density and the low-ionization zone temperature for each galaxy and compare if there is an advantage over using T$_e$[O III]. The T$_e$[O II] is calculated from the ratio

$$R_{O2} = \frac{I(\lambda 3726) + I(\lambda 3729)}{I(\lambda 7319) + I(\lambda 7330)} \tag{3.23}$$

This ratio, however, cannot be used straightforward. It needs a correction from recombination lines. The equations presented are valid for the analysis made on CELs while the physics of recombination is different. Therefore, we need to get rid of any contamination from recombination emission to calculate the electron temperature with pure flux from CELs. The emission from recombination contaminating the [O II]$\lambda\lambda$7319,7330 doublet can be characterized by

$$\frac{I_R(\lambda 7319 + \lambda 7330)}{I(\text{H}\beta)} = 9.36 \cdot t^{0.44} \cdot \frac{\text{O}^{2+}}{\text{H}^+} \tag{3.24}$$

where t is the electron temperature and O^{2+}/H$^+$ is the abundance of O^{2+} ions with respect to ionized hydrogen H$^+$. Although we do not present the calculations of abundances until Section 3.7, the previous formula implies the use of an ionic abundance in between. Only in this case we jump to the calculation of some ionic abundances described in the next section and come back to the procedures of this one to get the final estimates of each temperature after applying the correction (See Section 3.7 for details). This correction, fortunately, only depends on the abundance of O^{2+} ions and their corresponding electron temperature T$_e$[O III], two quantities that depend only on the observed fluxes of [O III]λ5007, [O III]λ4959, [O III]λ4363, and Hβ. This is because the emission corresponds exactly to the process of O^{2+} capturing photons, turning into excited O$^+$ that leads to [O II] emission. We account for the recombination correction using T$_e$[O III] and the ionic abundances from Eq. 3.32. Once the ratio is corrected, the electron temperature of the low-ionization zone is given by

$$\text{T}_e[\text{O II}] = a_0(n) + a_1(n) \cdot R_{O2} + \frac{a_2(n)}{R_{O2}} \tag{3.25}$$

which is the same functional form than T$_e$[O III], except the coefficients now have the non-negligible density dependence. The coefficients for the [O II] temperature are outlined in Pérez-Montero (2017) as

$$a_0(t) = 0.2526 - 3.57 \cdot 10^{-4} \cdot n - \frac{0.43}{n}$$
$$a_1(t) = 0.00136 + 5.42 \cdot 10^{-6} \cdot n + \frac{0.00481}{n} \qquad (3.26)$$
$$a_2(t) = 35.624 - 0.0172 \cdot n + \frac{25.12}{n}$$

The emission lines involved in this calculation belong to the doublets [O II]$\lambda\lambda$3726,3729 and [O II]$\lambda\lambda$7319,7330. As well as [O III]λ4363 and [O III]λ5007 case, the energy required to bring oxygen atoms from the ground level to an excited state that will trigger lines in the [O II]$\lambda\lambda$3726,3729 doublet is higher than the required to trigger [O II]$\lambda\lambda$7319,7330, thus, the flux ratio between these two doublets is temperature-sensitive. As they are doublets, the ratio between fluxes of their belonging members are sensitive to density too and that is why this temperature traces and depends on both quantities. Now that we know how to calculate the electron density n_e[S II] and temperature T$_e$[O II], we proceed with the test.

At first, the electron density is calculated using T$_e$[O III] straightforward. To determine T$_e$[O II] and n_e[S II] consistently, first we note that the ratios R_{O2} and R_{S2} are measured from the emission line fluxes of each galaxy. Once the ratios are measured, the only variable left are the density and temperature for T$_e$[O II] and n_e[S II], respectively. If, for instance, we evaluate T$_e$[O II] for several electron densities for a fixed R_{O2} we get the curve of temperatures as a function of the density. In the same way, we can get the curve of densities valid for a range of temperatures once R_{S2} is fixed. Subsequently, if we use the curve of densities to iterate and get another curve of temperatures we can graphically compare the two available curves of temperatures and study the point where they cross. Such point defines a temperature-density pair that is consistent with Eqs. 3.21 and 3.25. This is the exact procedure we followed to determine these two quantities consistently. We compare the electron densities derived using T$_e$[O III] and T$_e$[O II] with the density-consistent method. Figure 3.6 shows the comparison between the electron densities estimated with the two methods. It can be seen that they follow closely the 1:1 relation with errors included. This is supported by the extremely low scatter of $\sigma = 4.09$ cm^{-3} existing between the two variables shown in the right panel of the Figure. This result confirms the statement of Pérez-Montero (2017) about calculating the density accurately only by using T$_e$[O III]. We decided to adopt the value of the density from the calculation with T$_e$[O III] as it is more direct. This test gave us a quick snapshot of the values of electron density of our galaxies, but we let the discussion and analysis for the following chapters. We report the final values of electron density with their uncertainties in Table 4.1.

Finally, we also estimate the T$_e$[N II] temperature. This is done by computing the ratio
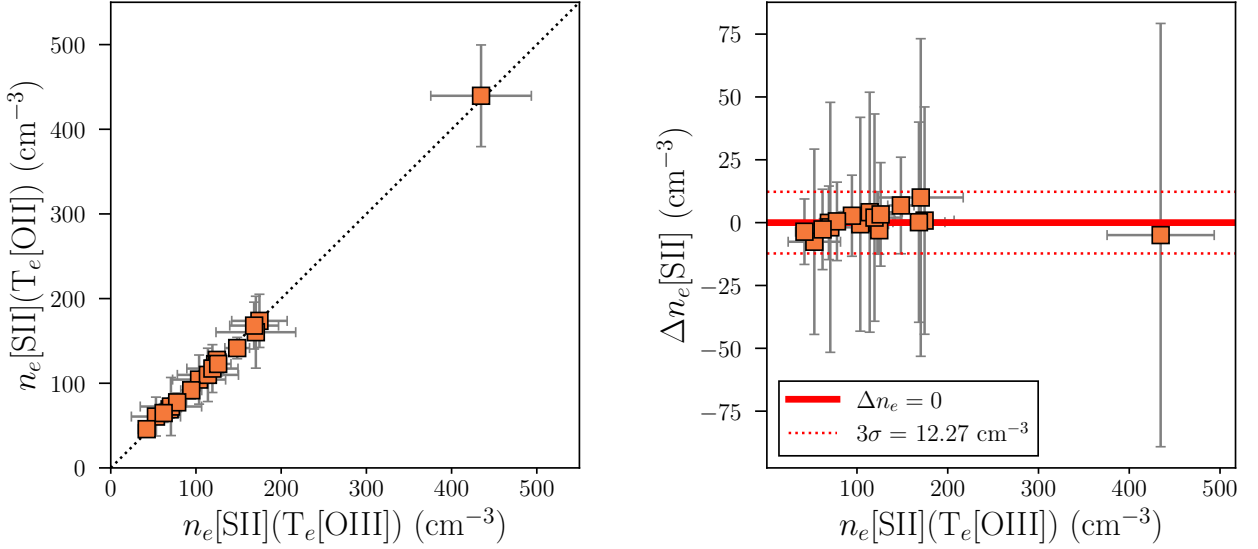
Figure 3.6: (Left) Comparison of the electron densities estimated with $T_e[\text{O III}]$ against the densities derived with a consistent analysis of $T_e[\text{O II}]$. The orange squares are the measurements of the density with their respective gray errorbars. The dotted black line represents the relation 1:1. (Right) Another perspective of the comparison with $\Delta n_e = n_e(T_e[\text{O III}]) - n_e(T_e[\text{O II}])$ as a function of $n_e(T_e[\text{O III}])$. The solid horizontal line is the $\Delta n_e = 0$ and the red dotted lines show the 3σ levels with $\sigma = 4.09 \text{ cm}^{-3}$ as the scatter between the two estimated densities.

$$R_{N2} = \frac{I(\lambda 6548) + I(\lambda 6584)}{I(\lambda 5755)} \tag{3.27}$$

and using the formula

$$T_e[\text{N II}] = 0.6153 - 1.529 \cdot 10^{-4} \cdot R_{N2} + \frac{35.3641}{R_{N2}} \tag{3.28}$$

that is used in the same way than the [O III] and [S III] electron temperatures, but with a correction for recombination first. Similar than [O II], [N II] suffer from recombination emission that can be characterized by the formula

$$\frac{I_R(\lambda 5755)}{I(\text{H}\beta)} = 3.19 \cdot t^{0.3} \cdot \frac{\text{N}^{2+}}{\text{H}^+} \tag{3.29}$$

where t is the electron temperature, and N^{2+}/H^+ is the abundance of N^{2+} ions. The temperature to use in this formula corresponds to the high-ionization zone electron temperature, as the ionization potential is near to that of the [O III] ion (47.45 and 54.94 eV, respectively; Kramida et al. 2023) than for the low and intermediate ionization zone tracers. However, there is no equations in Pérez-Montero (2017) to calculate the N^{2+} abundance from CELs in optical spectra. In this case, we use PyNeb to deal with this issue. We provide the R_{N2} ratio and the density calculated from [S II] lines to the getTemDen method of the Atom class of PyNeb and it return the values of electron temperature. Note that a density must be given as input, but in principle it should not affect the calculation of the temperature as the

R_{N2} is sensitive to the electron temperature rather than density. The auroral [N II]λ5755, however, has the same problem than [O III]λ4363. It is very faint, and it can turn elusive in extragalactic HII regions. This is actually our case, where the line is only detected in $\sim 28\%$ (5/18) of the local analogs.

3.7 Chemical Abundances

After estimating the electron density and electron temperature of all the ionization zones we are ready to estimate the relevant chemical abundances for this study. Again, the procedure described here is following equations and suggestions from Pérez-Montero (2017) applied to our data, so we encourage the reader to refer to that paper for details of the fits, collisional strengths, models used to derive the equations, and further references. For this section, we adopt the variable names used in Pérez-Montero (2017) for the scheme of electron temperatures. By doing this, the electron temperature of the high, intermediate, and low-ionization zones are noted as t_h, t_m, and t_l, respectively. This means that $t_h = \mathrm{T}_e[\mathrm{O\ III}]$, $t_m = \mathrm{T}_e[\mathrm{S\ III}]$, and $t_l = \mathrm{T}_e[\mathrm{O\ II}]$.

The first and most important abundance that we calculate is the oxygen abundance. This is the relative amount of oxygen with respect to the amount of hydrogen in the gas. The whole analysis of the calibrations depends on having accurate and reliable estimations of this elemental abundance. The total abundance of oxygen is assumed to be

$$\frac{\mathrm{O}}{\mathrm{H}} = \frac{\mathrm{O}^+}{\mathrm{H}^+} + \frac{\mathrm{O}^{2+}}{\mathrm{H}^+} \tag{3.30}$$

With Eq. 3.30, estimations of the singly and doubly ionized oxygen are necessary but not sufficient to estimate the metallicity of a galaxy. More oxygen can be in other ionized states, such as O^{3+}, so we need to correct the total by the ionic abundances missing. We derive the singly ionized oxygen abundance using the blue [O II]$\lambda\lambda$3726,3729 doublet as follows:

$$12 + \log\left(\frac{\mathrm{O}^+}{\mathrm{H}^+}\right) = \log\left(\frac{I(\lambda 3726) + I(\lambda 3729)}{I(\mathrm{H}\beta)}\right) + 5.887 + \frac{1.641}{t_l} - 0.543 \cdot \log(t_l) + 1.14 \cdot 10^{-4} \cdot n_e \tag{3.31}$$

where $n_e = n_e[\mathrm{S\ II}]$ is the electron density. The doubly ionized oxygen abundance is calculated as

$$12 + \log\left(\frac{\mathrm{O}^{2+}}{\mathrm{H}^+}\right) = \log\left(\frac{I(\lambda 4959) + I(\lambda 5007)}{I(\lambda 4363)}\right) + 6.1868 + \frac{1.2491}{t_h} - 0.5816 \cdot \log(t_h) \tag{3.32}$$

To account for missing oxygen in other ionization states we use the ionization correction factors (ICFs). If the ionizing radiation is strong enough to reach energies over 54.94 eV,

some of the oxygen might be in the form of O^{3+}. There is no lines in our optical spectra of star-forming galaxies that we could use to determine directly an O^{3+} abundance. Fortunately, the ionization potential of He II is about 54.424 eV, very close to the ionization potential of [O III]. This implies that whenever we detect the He II $\lambda 4686$ emission line we can estimate the ICF of oxygen to account for their contained in the form of O^{3+} and more. In cases where the line is not detected the oxygen abundance is straightforward and the correction can be ignored as it is assumed that negligible amount of oxygen is in thirdly ionized. In our sample, 72.2% (13/18) of the sample have He II $\lambda 4686$ detected above the 3σ level. We apply the correction on those galaxies by calculating the ICF of the oxygen abundance as

$$\text{ICF}(O^+ + O^{2+}) = 1 + \frac{\text{He}^{2+}}{\text{He}^+} \tag{3.33}$$

so we need to compute first the ratio of doubly-to-singly ionized helium abundance in order to correct the oxygen abundance. As well as oxygen, the helium abundance can be calculated as the sum of the singly and doubly ionized helium abundances as

$$\frac{\text{He}}{\text{H}} = \frac{\text{He}^+}{\text{H}^+} + \frac{\text{He}^{2+}}{\text{H}^+} \tag{3.34}$$

No ICF for helium is needed because it only has two electrons. The expression to compute the singly ionized helium is given by

$$\frac{\text{He}^+}{\text{H}^+} = \frac{I(\lambda \text{ He I})}{I(\text{H}\beta)} \cdot \frac{F_\lambda(n, t)}{f_\lambda(n, t, \tau)} \tag{3.35}$$

where $F_\lambda(n, t)$ is the emissivity of the line at λ scaled to Hβ, $f_\lambda(n, t, \tau)$ is the optical depth function of the line. These two quantities depend on the electron density, temperature, and the optical depth τ (The latter only on the optical depth function). Note that we wrote the intensity $I(\lambda \text{He I})$ with no specified wavelength. This is because the He$^+$ abundance can be calculated from any of the He I lines. The best procedure is to take as many He I lines as possible and calculate the weighted mean of the He$^+$ abundance between them. We followed this approach by considering only the strongest lines He I $\lambda 4471$, He I $\lambda 5876$, He I $\lambda 6678$, and He I $\lambda 7065$. The emissivities outlined in Pérez-Montero (2017) from references therein are:

$$
\begin{aligned}
F_{4471} &= (2.0301 + 1.5 \cdot 10^{-5} \cdot n) \cdot t^{0.1463 - 0.0005 \cdot n} \\
F_{5876} &= (0.745 - 5.1 \cdot 10^{-5} \cdot n) \cdot t^{-0.226 - 0.0011 \cdot n} \\
F_{6678} &= (2.612 - 0.000146 \cdot n) \cdot t^{0.2355 - 0.155 \cdot n} \\
F_{7065} &= (4.329 - 0.0024 \cdot n) \cdot t^{-0.368 - 0.0017 \cdot n}
\end{aligned}
\tag{3.36}
$$

For n and t we use the electron density n_e and temperature $T_e[O \text{ III}]$. The value of τ used for the optical depth function is calculated by using the color-excess estimated for the dust extinction of the galaxies according to Eq. 3.2. As Pérez-Montero (2017) suggests, the

optical depth functions are taken from Olive and Skillman (2004) that states:

$$
\begin{aligned}
f_{4471} &= 1 + \left(\frac{\tau}{2}\right)[0.00274 + (8.81 \cdot 10^{-4} - 1.21 \cdot 10^{-6} n_e) \cdot t] \\
f_{5876} &= 1 + \left(\frac{\tau}{2}\right)[0.00470 + (2.23 \cdot 10^{-3} - 2.51 \cdot 10^{-6} n_e) \cdot t] \\
f_{6678} &= 1 \\
f_{7065} &= 1 + \left(\frac{\tau}{2}\right)[0.359 + (-3.46 \cdot 10^{-2} - 1.84 \cdot 10^{-4} n_e + 3.039 \cdot 10^{-7} n_e^2) \cdot t]
\end{aligned}
\tag{3.37}
$$

With this set of equations, we calculate four singly-ionized helium abundances and averaged them weighted by their errors to have a single estimation of He^+. The doubly-ionized helium abundance is much simpler as shown in Eq. 3.38:

$$
\frac{He^{2+}}{H^+} = \frac{I(\lambda 4686)}{I(H\beta)} \cdot 0.0416 \cdot t^{-0.146}
\tag{3.38}
$$

Once again, $t = t_h$. Finally, by using Eq. 3.34 to calculate the total helium abundance and Eq. 3.33 to estimate the ICF of oxygen, the metallicity of the galaxy traced by oxygen is constrained as

$$
\frac{O}{H} = ICF(O^+ + O^{2+}) \cdot \frac{O^+ + O^{2+}}{H^+}
\tag{3.39}
$$

The average value of the ICF of oxygen for the 13 galaxies in our sample is 1.005, giving an average correction of an increase by 5% in the measured $12 + \log(O/H)$. Besides oxygen, nitrogen provides valuable insights into the ionization conditions of the ISM and the evolutionary state of galaxies. We estimate the singly ionized nitrogen abundance using the [N II]$\lambda 6548$ and [N II]$\lambda 6584$ lines along the Hα profile as

$$
12 + \log\left(\frac{N^+}{H^+}\right) = \log\left(\frac{I(\lambda 6548) + I(\lambda 6584)}{H\beta}\right) + 6.291 + \frac{0.90221}{t_l} + 0.05511 \cdot \log(t_l)
\tag{3.40}
$$

The ICF of nitrogen is calculated by assuming that the portion of singly ionized nitrogen with respect to the total nitrogen in the gas follows the same proportion than the singly-ionized oxygen to the total oxygen. Therefore,

$$
ICF(N^+) = \frac{O}{O^+}
\tag{3.41}
$$

leading to the correction

$$
\frac{N}{H} = ICF(N^+) \cdot \frac{N^+}{H^+}
\tag{3.42}
$$

The evolutionary state of a galaxy can be studied from the relative abundance of nitrogen to oxygen owing that the contribution to nitrogen abundance becomes more important for

galaxies with an evolved stellar population. Two methods can be used to estimate the N/O ratio of the gas-phase of galaxies. It can be directly extracted from the nitrogen and oxygen abundances or one can use the fit:

$$\log\left(\frac{\text{N}^+}{\text{O}^+}\right) = \log\left(\frac{I(\lambda6584)}{I(\lambda3726) + I(\lambda3729)}\right) + 0.493 - 0.025 \cdot t_l - \frac{0.687}{t_l} + 16.21 \cdot \log(t_l) \quad (3.43)$$

which is the option we adopt in this case. The use of Eq. 3.43 gives consistent results to taking the difference between $12 + \log(\text{N/H})$ - $12 + \log(\text{O/H})$. Figure 3.7 shows the workflow we follow to measure each quantity illustrating the requirements of each step from the electron temperatures to the estimated chemical abundances.

We finally estimate the ionization parameter (q) for our sample. An iterative calculation based on the metallicity of the objects was proposed by Kewley and Ellison (2008), due to a dependence between these quantities. However, we robustly constrain the oxygen abundance from the methods described above and modifications to these values could contradict the equations derived from the direct-T_e method. The relations states that the ionization parameter in units of cm/s can be estimated as:

$$\log(q) = \frac{32.81 - 1.153y^2 + x \cdot (-3.396 - 0.025y + 0.1444y^2)}{4.603 - 0.3119y - 0.163y^2 + x \cdot (-0.48 + 0.0271y + 0.02037y^2)} \quad (3.44)$$

where $y = \log([\text{O III}]\lambda5007/[\text{O II}]\lambda3726)$ and $x = 12 + \log(\text{O/H})$. For all the calculations made on Sections 3.6 and 3.7 we used the 10000-steps long chains of possible solutions to the emission line fitting of our data as described in Section 3.4. The chains of the emission lines are further corrected by the dust attenuation described in Section 3.5. These chains define distributions of electron density, electron temperatures, and chemical abundances. Thus, we work with the complete chains of fluxes and take the final values of each physical quantity along with 16th and 84th percentiles from their distributions as in Tables 4.1 and E.1.
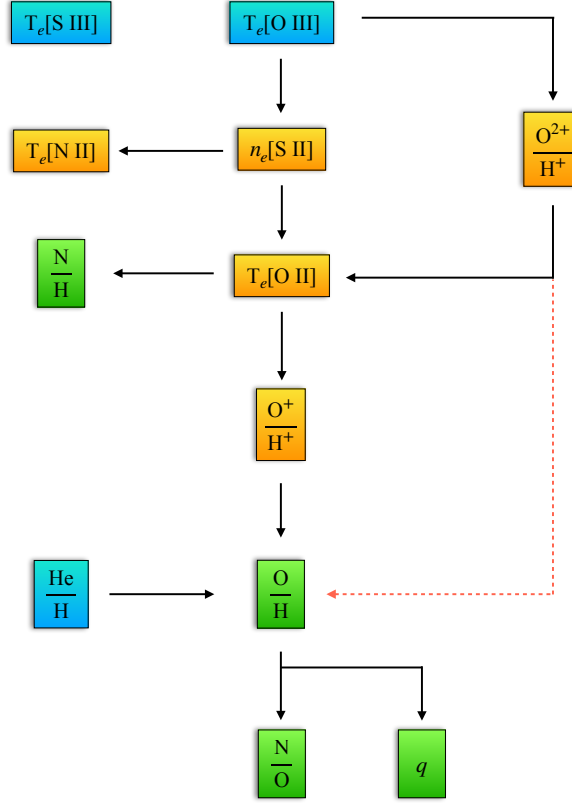
Figure 3.7: Workflow of calculation of electron temperatures, the electron density, and chemical abundances. Quantities that can be calculated directly from emission line ratios are colored in blue. In yellow, we show the variables that depend on other properties in the workflow. Final chemical abundances of elements are shown in green. The red-dashed lines are to clarify that the oxygen abundance also use the doubly ionized oxygen abundance.

3.8   SELRs

Here we present the definition of the SELRs that we used in this study to calibrate the direct-method metallicities. Before the launch of JWST, the emission line budget in spectra of high-z galaxies was limited by the strong atmosphere absorption due water vapor in the atmosphere. The rest-frame optical emission lines needed to accurately estimate electron temperatures and abundances are shifted to the infrared where the absorption is more extreme. The infrared bands surviving the absorption allowed several studies of metallicities of galaxies at $z > 1$ such as in the MOSDEF Survey (Kriek et al., 2015) and the KBSS Survey (Steidel et al., 2014). Nevertheless, these studies still lack lots of lines to carry out robust estimations of metallicity having to rely on previous metallicity calibrations such as the derived in this work or in temperature relations from photoionization models (Garnett, 1992),

highlighting even more the importance of using a set of calibraitons physically consistent with galaxies at high-z.
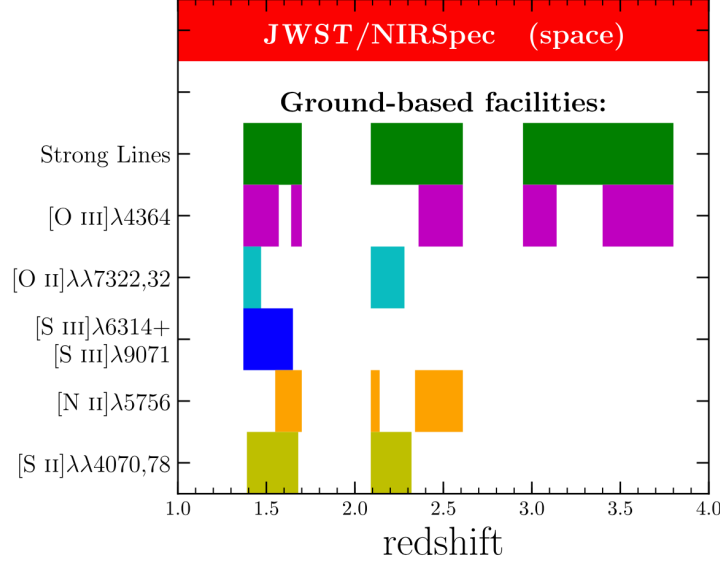
Figure 3.8: Diagram of detectability of rest-optical emission lines for galaxies at $1 < z < 4$ by Sanders et al. (2023). The y-axis denotes the emission lines, where "Strong Lines" refers to the usual brighter lines in optical spectra such as [O II]λ3726,29, Hβ [O III]λ5007, Hα, [N II]λ6548, [S II]λ6713,17. The colored blocks indicate the redshift ranges where the lines are detectable and the red block at the top shows the range covered by JWST/NIRSpec.

Now, the JWST will provide spectra spanning enough emission lines to directly estimate metallicities in galaxies up to $z = 4$ and beyond. Our calibrations will set a base level to compare upcoming findings in the early Universe so we define the SELRs based on the lines that JWST will cover. Among the strongest lines in spectra of star-forming galaxies we find the [O II]$\lambda\lambda$3726,3729 doublet, [Ne III]λ3868, Hβ, [O III]λ4959, [O III]λ5007, Hα, [N II]λ6584, and the [S II]$\lambda\lambda$6716,6731 doublet. These strong lines can be detected in the infrared windows for galaxies at $z \sim 1.5$, $z \sim 2.5$ and between $z \sim 3.0 - 3.8$, unlike the faint auroral lines (See Figure 3.8). Garg et al. (2023) defined a list of 12 SELRs compiled from the literature that make use of the strong lines aforementioned. The SELRs are listed as follows:

- **N2**: $\log([\text{N II}]\lambda6584/\text{H}\alpha)$

- **R3**: $\log([\text{O III}]\lambda5007/\text{H}\beta)$

- **R2**: $\log([\text{O II}]\lambda3726, 3729/\text{H}\beta)$

- **R23**: $\log(([\text{O II}]\lambda3726, 3729 + [\text{O III}]\lambda4959, 5007)/\text{H}\beta)$

- **O3N2**: $\log(([\text{O III}]\lambda5007/\text{H}\beta)/([\text{N II}]\lambda6584/\text{H}\alpha))$

- **R3N2**: $\log([\text{O III}]\lambda5007/[\text{N II}]\lambda6584)$

- **N2O2**: $\log([\text{N II}]\lambda6584/[\text{O II}]\lambda3726)$

- **O3O2**: $\log([\text{O III}]\lambda5007/[\text{O II}]\lambda3726, 3729)$

- **Ne3O2**: $\log([\text{Ne III}]\lambda3868/[\text{O II}]\lambda3726, 3729)$

- **S2**: $\log([\text{S II}]\lambda6716, 31/\text{H}\alpha)$

- **O3S2**: $\log(([\text{O III}]\lambda5007/\text{H}\beta)/([\text{S II}]\lambda6716, 31/\text{H}\alpha))$

- **N2S2**: $\log(([\text{N II}]\lambda6584/[\text{S II}]\lambda6716, 31) + 0.264 \cdot ([\text{N II}]\lambda6584/\text{H}\alpha))$

We study the relations between these ratios and metallicity in Section 4.3.

Chapter 4

Results

In this chapter we present the results the calculations outlined in Chapter 3. It is divided into three sections with the main results of this research: Section 4.1 shows the measured physical properties of our sample of analogs including ionization conditions, stellar mass, and star-formation activity. Section 4.2 studies the relation between the temperatures of the different ionization zones and Section 4.3 gives the new calibration between SELRs and metallicity for galaxies at high-z.

4.1 Physical conditions

Here we show the results of some of the most relevant physical properties of the sample of analogs that help characterizing the type of galaxies used in this study. For this, we compare with the sample of analogs selected by Bian et al. (2016) from SDSS with the same selection criteria and the properties of galaxies found in some high-z studies.

4.1.1 Electron Density

A little glimpse into the values of the electron density of our analogs was given in Figure 3.6 of Section 3.6 while in the current Section we present the actual values and distribution. Measured values of electron densities are shown in Table 4.1 and the histogram of $\log(n_e)$ is included in Figure 4.1. Bian et al. (2016) found that the sample of analogs selected from the SDSS survey with the same criteria than in this work have a median of $n_e \sim 200$ cm^{-3} which is very close to the 250 cm^{-3} found in galaxies at $z \sim 2.3$ (Sanders et al., 2016) and almost one order of magnitude higher than the value found in normal star-forming galaxies at $z \sim 0$. We found that our galaxies are well clumped between $n_e \sim 40$ and 180, with a median of 117 ± 22 cm^{-3}. This value is still high compared to electron densities in normal star-forming galaxies at $z \sim 0$, but slightly lower than the median electron density found in high-z galaxies and analogs from Bian et al. (2016). Note that in our sample two galaxies present values in both the low and high electron density regimes. J2119+0052 has a density of $n_e = 43.2$ cm^{-3} very close to the median of $z \sim 0$ galaxies and J0240$-$0828 exhibit $n_e = 438$ cm^{-3} ($\log(n_e) = 2.64$

which is the only galaxy in the high electron density bin in 4.1), even exceeding the median density found in high-z galaxies. As we mention before in Section 3.2, SED models cannot constrain well reliably the value of the electron densities just from the photometric data. Electron densities of $400 - 500$ cm^{-3} exceeds by far the real values measured for our analogs with the direct method, which is much more robust and precise in comparison. The only galaxy with a similar value than the predicted by the SED models is indeed J0240$-$0828 although it is an unfair comparison since the predicted values from the SED are uncertain in the whole range of electron densities up to 1000 cm^{-3} (See uncertainties in Table A.1), while the electron density of J0240$-$0828 is well constrained between $383 - 494$ cm^{-3} which is a range of around 100 cm^{-3}. In summary, our population of galaxies have higher electron density than local star-forming galaxies by 0.5 dex in $\log(n_e)$ and 0.2 lower than galaxies at $z \sim 2.3$.
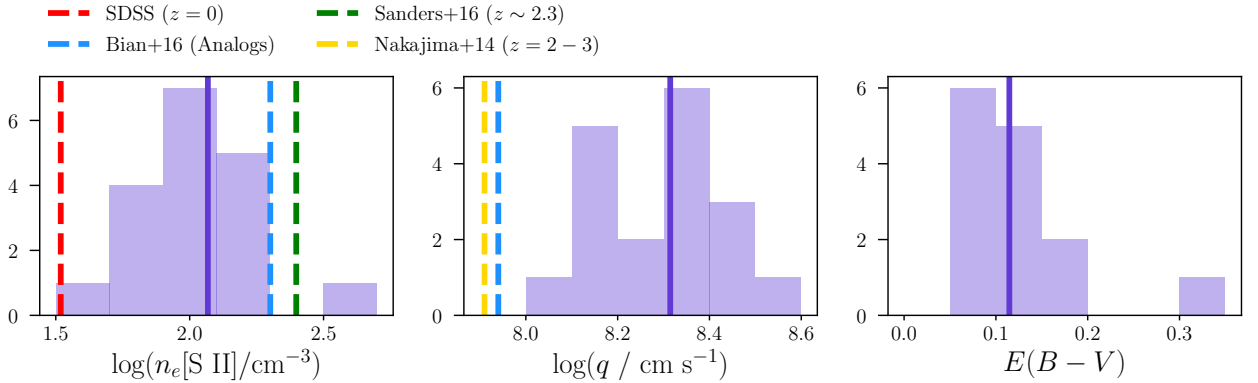
Figure 4.1: Distributions of electron density, ionization parameter, and color-excess for the sample of local analogs. In violet, the histogram bins are shown along with the median values represented by a vertical solid line. The median electron density of local star-forming galaxies of SDSS and local analogs selected by Bian et al. (2016) are shown as red and blue dashed vertical lines, respectively. The blue vertical-dashed lines represent the median values of electron density and ionization parameters found in Sanders et al. (2016) for galaxies at $z \sim 2.3$; in yellow, the ionization parameter of galaxies at $z \sim 2 - 3$ (Nakajima and Ouchi, 2014).

4.1.2   The Ionization Parameter

We study the distribution of ionization parameter for our sample of local analogs in the middle panel of Figure 4.1. (Bian et al., 2016) found a median of $\log(q(\text{cm/s})) \sim 7.94$. It is 0.6 dex higher than the estimated value for local SDSS star-forming galaxies and only 0.03 dex higher than the ionization parameter in galaxies at $z \sim 2 - 3$ (Nakajima and Ouchi, 2014) illustrating the good agreement between the selected analogs and high-z galaxies. We estimate that our sample have $\log(q) > 8.0$ with a median of $\log(q) \sim 8.32 \pm 0.01$. This value is about 0.4 dex higher than the median value of Bian et al. (2016) analogs and indicate that our sample comprises a group of galaxies in the hard ionization end of their distribution of analogs selected from SDSS. The SED models predict that almost half of our sample have $\log(U) \sim -2.0$ with the rest distributed between -3.0 and -1.0. For comparison, $q = cU$

so a median of -2.0 in $\log(U)$ is equivalent to $\log(q) \sim 8.48$, which is 0.16 dex higher than the median ionization parameter measured in our galaxies. Note that we do not measure explicitly the ionization parameter in the SED modeling, but we recover the best-fit value provided by CIGALE for comparison, which can adopt values of $\log(U) = \{-3.0, -2.0, -1.0\}$. The SED models then overestimate the median ionization parameter, although we cannot considerate this result as it is not reliably estimated from the SED fitting as mentioned in Section 3.2. Despite this, our results still suggest that it is really high even compared to galaxies at $z = 2 - 3$.

4.1.3   Dust Attenuation

The color-excess measured through Balmer decrements for our analogs is distributed between $E(B - V) = 0.0 - 0.4$ with zero values adopted for four galaxies with $E(B - V) < 0$ (See Section 3.5). Most of the other 14 galaxies in our sample show higher values of $E(B-V)$ than the Galactic dust attenuation where all have $E(B-V) < 0.1$ for the latter. The exceptions are the sources J1624$-$0022 and J2225$-$0011 that present very flat Balmer decrements leading to values of $E(B - V)$ similar to the galactic color-excess (See Table 3.2). In contrast, the color-excess derived from the SED modeling overestimate $E(B-V)$ with values around ~ 0.3, which is 0.2 dex above the median $E(B - V) = 0.115 \pm 0.033$ estimated for our analogs. We remind the reader that 0.3 was the upper limit allowed for $E(B - V)$ in the SED modeling which indicates that the models prefer even higher extinction as they mostly get stuck in this value in Table 3.2. The median color-excess found in our analogs agrees with values of the UV-slope of $\beta \sim -1.5$ for galaxies at $z \sim 2$ with $M_{UV} = -21$ with an assumed young stellar population with 100 Myr of constant star-formation (Bouwens et al., 2009). On the other hand, this value coincide with the UV-slope estimated by Bian et al. (2016) for the analogs from SDSS that also found values clumped around $\beta = -1.5$ in agreement with the dust extinction of local star-forming galaxies traced by the FIR-to-UV luminosity ratio from the Meruer relation (Meurer et al., 1999).

4.1.4   Stellar Mass, SFR, and sSFR

The sample of local analogs in this work show low stellar-masses derived from the SED fitting compared to the analogs in Bian et al. (2016). Our results are grouped in the low mass end of the distribution with a median of $\log(M/M_\odot) = 8.07 \pm 0.13$ which is almost 1.0 dex lower than the median of the SDSS analogs as illustrated in Figure 4.2. This result in a very low mass sample compared to local star-forming galaxies at $z \sim 0$ having a median near $\log(M/M_\odot) = 10$. The SFH of the old population with a late burst of star-formation predicts a median SFR of 3.50 ± 0.29 $M_\odot$/yr. This is in agreement with the median SFR of ~ 3.6 $M_\odot$/yr predicted by Bian et al. (2016) as it can be noted in Figure 4.2. We compare the results of the SFR to the predicted values of the star-formation main sequence of galaxies at $z = 2 - 3$ from Rodighiero et al. (2011) for a galaxy with our median stellar-mass of
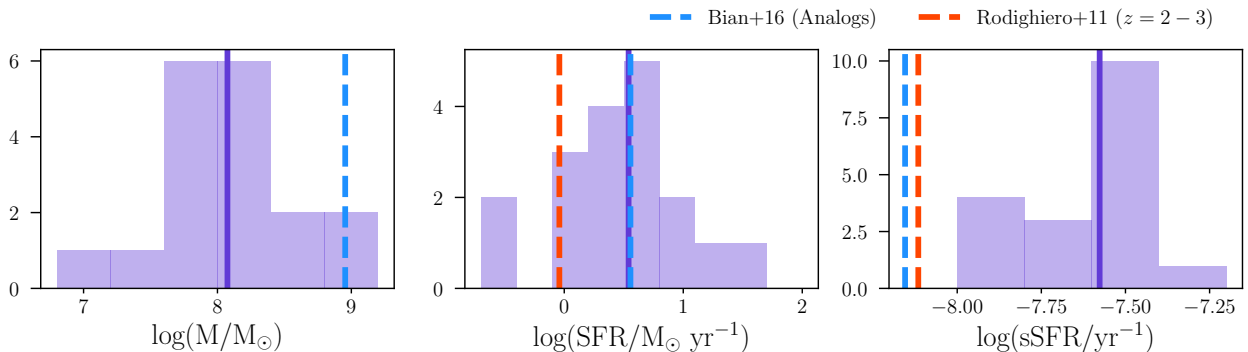
Figure 4.2: Distributions of stellar-mass, SFR, and sSFR for the sample of local analogs in this study. Same colors than Figure 4.2 are assigned for the distributions and medians including Bian et al. (2016) results. Additionally, the predicted SFR and sSFR from the main sequence relation of Rodighiero et al. (2011) for the median stellar-mass of our sample $\log(M/M_\odot) = 8.07 \pm 0.13$ is added as a red-dashed vertical line.

$\log(M/M_\odot) = 8.07$. The red-dashed vertical line in Figure 4.2 indicates that galaxies with $10^{8.07}$ solar masses should have SFR values around $1\,M_\odot/\text{yr}$ ($\log(\text{SFR}) \sim 0$) which is 3.5 times less than the estimated median SFR of our analogs. This leads to a very high sSFR shown in the right panel of Figure 4.2 where our analogs exhibit a median of $\log(\text{sSFR/yr}) = -7.58$. Unlike our estimation and according to the sSFR of $\log(\text{sSFR/yr}) = -8.12$ predicted by the main sequence at $z = 2 - 3$ from Rodighiero et al. (2011), a galaxy with the median stellar mass of our analogs should be in very well agreement with the sSFR estimated for the sample of SDSS analogs in Bian et al. (2016) due to the close position of the blue and red dashed lines in the right panel of Figure 4.2. These results suggest that our sample of analogs comprises a group of low-mass highly active star-forming galaxies.

4.2   Temperature Relations

The electron temperatures of the ionized regions of the ISM in galaxies can be measured in high-z galaxies depending on the detectability of their auroral lines in the infrared (Sanders et al., 2023). The relation between the electron temperatures traced by ions representing different ionizaiton zones have been explored in the local Universe with measurements of HII regions (CHAOS survey; Berg et al. 2020a) and through photoionizaiton models (Stasińska, 1990; Garnett, 1992). Here, we present for the first time the temperature relations using our sample of local analogs providing the closest insight into temperature relations in the high-z Universe.

Table 4.1 shows the values of electron temperatures of the high, intermediate, and low-ionization zones derived with the direct-T_e method described in Section 3.6. We found $T_e[\text{O III}]$ to be well contained within the range $10000 - 18000\text{K}$ with a median of $= 1.288 \pm 0.005 \cdot 10^4\text{K}$. The low-ionization zone electron temperature shows lower values with a median of

T_e[O II] = 1.094$\pm$0.027$\cdot 10^4$K and values varying between 8000 and 16000 K. The temperature of the intermediate ionization zone estimated for 14/18 galaxies exhibit a median of T_e[S III] = 1.301 $\pm$ 0.016 $\cdot 10^4$K in agreement with T_e[O III], but covering a slightly wider range between 10000 $-$ 19000K. Only five galaxies have measurements of T_e[N II] that is often used as another representative of the low ionization zone. A median of T_e[N II] = 1.23$\pm$0.04$\cdot 10^4$K is found which is 0.2 dex higher than T_e[O II].

Table 4.1: Values of electron density and electron temperatures derived from the direct-method according to Section 3.6.

ID	n_e (cm^{-3})	T_e[O III] (10^4 K)	T_e[O II] (10^4 K)	T_e[S III] (10^4 K)	T_e[N II] (10^4 K)
J0021+0052	$122.997^{131.248}_{114.714}$	$1.076^{1.087}_{1.065}$	$1.072^{1.089}_{1.055}$	$0.998^{1.018}_{0.979}$	$1.658^{1.731}_{1.585}$
J0023$-$0948	$69.427^{79.414}_{59.788}$	$1.247^{1.257}_{1.238}$	$1.379^{1.406}_{1.353}$	$1.306^{1.336}_{1.276}$	
J0136$-$0037	$70.276^{104.925}_{37.628}$	$1.349^{1.367}_{1.330}$	$1.137^{1.201}_{1.074}$	$1.287^{1.356}_{1.220}$	
J0240$-$0828	$437.986^{494.862}_{383.509}$	$1.440^{1.448}_{1.431}$	$1.595^{1.682}_{1.510}$	$1.471^{1.543}_{1.402}$	
J0252+0114	$112.786^{149.276}_{78.802}$	$1.448^{1.470}_{1.425}$	$1.245^{1.325}_{1.169}$	$1.239^{1.309}_{1.170}$	
J0305+0040	$114.009^{147.481}_{82.182}$	$1.215^{1.246}_{1.184}$	$0.904^{0.945}_{0.867}$	$1.141^{1.205}_{1.081}$	
J0950+0042	$93.800^{105.514}_{82.145}$	$1.273^{1.281}_{1.266}$	$0.788^{0.794}_{0.781}$		
J1146+0053	$79.585^{109.052}_{51.270}$	$1.605^{1.613}_{1.596}$	$0.843^{0.867}_{0.822}$		
J1226+0415	$148.644^{162.621}_{134.458}$	$1.398^{1.401}_{1.394}$	$0.958^{0.974}_{0.943}$	$1.218^{1.245}_{1.193}$	$1.137^{1.251}_{1.029}$
J1444+0409	$174.608^{207.113}_{143.061}$	$1.667^{1.677}_{1.657}$	$1.330^{1.411}_{1.251}$	$1.489^{1.549}_{1.432}$	
J1448$-$0110	$127.089^{133.038}_{121.156}$	$1.197^{1.200}_{1.195}$	$0.886^{0.891}_{0.880}$	$1.297^{1.307}_{1.286}$	$1.311^{1.420}_{1.201}$
J1624$-$0022	$119.950^{149.254}_{92.176}$	$1.138^{1.170}_{1.105}$	$1.117^{1.171}_{1.065}$	$1.340^{1.428}_{1.254}$	
J2101$-$0555	$125.706^{141.057}_{110.967}$	$1.100^{1.110}_{1.091}$	$0.880^{0.899}_{0.863}$		$1.035^{1.157}_{0.913}$
J2119+0052	$43.214^{52.528}_{34.115}$	$1.126^{1.140}_{1.113}$	$0.988^{1.003}_{0.972}$	$1.172^{1.200}_{1.146}$	
J2212+0006	$169.710^{216.642}_{126.341}$	$1.060^{1.088}_{1.034}$	$0.889^{0.961}_{0.825}$		
J2215+0002	$78.102^{88.679}_{67.542}$	$1.303^{1.309}_{1.297}$	$1.315^{1.332}_{1.298}$	$1.359^{1.377}_{1.341}$	$1.226^{1.281}_{1.173}$
J2225$-$0011	$62.124^{73.113}_{51.265}$	$1.438^{1.445}_{1.432}$	$1.128^{1.150}_{1.107}$	$1.486^{1.509}_{1.464}$	
J2337$-$0010	$168.448^{194.647}_{142.598}$	$1.781^{1.791}_{1.770}$	$1.345^{1.390}_{1.301}$	$1.891^{1.961}_{1.823}$	

Figure 4.3 shows the relations between T_e[O III] and the rest of the electron temperatures measured in this study. We investigate the best-fit relations from our data using the LINMIX python package (Kelly, 2007). This package provides an implementation of a gaussian mixture Bayesian model regression of a straight line to data with uncertainty in both axis and an explicit treatment of the intrinsic scatter that is very robust to cases with outliers and/or heteroscedasticity. We compare our results with temperature relations from literature measured in photoionization models (Garnett, 1992; Pérez-Montero, 2017) (G92 and PM17 hereafter) and local HII regions (Berg et al., 2020b; Rogers et al., 2021) (B20 and R21 hereafter). Strictly speaking, the relation between T_e[O II] and T_e[O III] that we refer

to G92 was first used by Campbell et al. (1986), the curved relation is from Stasińska (1990) models, and the density-dependent relation that we refer from PM17 is from Hägele et al. (2006). In this work and for simplicity, we refer to these relations as from the source where we took it from.

The best-fit relation found for $T_e[O\ II]$ vs $T_e[O\ III]$ is shown in Eq. 4.1:

$$T_e[O\ II] = (0.46 \pm 0.28) \cdot T_e[O\ III] + (0.49 \pm 0.38) \qquad (4.1)$$

with $\sigma_{int} = 2374$ K.

The high intrinsic dispersion above 2000K is due to the scatter existing between these temperatures that increases with increasing $T_e[O\ III]$ as illustrated by Figure 4.3. We note that the relation we found gives a shallower slope than the 1:1 relation and even more than the predicted by G92. On the other hand, our relation lies below the smooth relation from PM17 that gives $\gtrsim 0.2$ dex higher values of $T_e[O\ II]$ above $T_e[O\ III] \sim 1.5 \cdot 10^4$K. By comparing our relation with a similarly smooth but density-dependent relation outlined in PM17 we observe that there is a very good agreement between values of $1.0 - 1.5 \cdot 10^4$K with an input electron density of $n_e = 250$ cm^{-3}. For higher $T_e[O\ III]$ the disagreement increases reaching up to 0.1 dex at $T_e[O\ III] = 2.0 \cdot 10^4$K. Despite the scatter, we can observe some sub-trends of the data by noticing that there is a sample of galaxies clustered in the $T_e[O\ II]$ regime that does not vary much with $T_e[O\ III]$. In contrast, there are about three galaxies lying exactly in the 1:1 relation, while the rest of the galaxies above the best-fit relation seem to agree with the G92 relation at the same time than for the derived in this work.

The second relation we explore is the $T_e[S\ III]$ vs $T_e[O\ III]$ relation. The best-fit linear function is given by Eq. 4.2:

$$T_e[S\ III] = (0.87 \pm 0.20) \cdot T_e[O\ III] + (0.17 \pm 0.28) \qquad (4.2)$$

with $\sigma_{int} = 1367$ K.

The dispersion in this relation is lower due to the good agreement between these two electron temperatures. Our results are observed to vary around the 1:1 relation in the upper right panel of Figure 4.3, supported by the high slope of 0.87 ± 0.20 found in the relation. This result is higher by 0.04 dex than that of G92 from photoionization models leading to a really low difference with our fit considering the scatter of the data. As well as in the left panel, a subset of about 3 to 4 galaxies in our sample with low values of $T_e[O\ III]$ agrees with the temperature relations found in local HII regions by B20 and R21 who show a very steep slope in comparison. However, our trend is completely different to these relations showing a very distinct behavior in local HII regions.

The third and last relation we fit is the T_e[O II] vs T_e[S III] relation. As we already explored the relations that these two temperatures hold with T_e[O III], we expect this relation to follow a derived trend from those relations. As the T_e[O III] and T_e[S III] temperatures show the tightest relation in this work, we expect that the T_e[O II] follows a similar trend with T_e[S III] than with T_e[O III]. Indeed, we find that:

$$T_e[\text{O II}] = (0.55 \pm 0.31) \cdot T_e[\text{S III}] + (0.43 \pm 0.41) \tag{4.3}$$

with $\sigma_{int} = 2116$ K. This relation shown in the lower right panel of Figure 4.3, predicts lower values of T_e[O II] for a fixed T_e[S III] as well as the relation between T_e[O II] and T_e[O III]. The slope of 0.55 ± 0.58 is higher than the slope found for T_e[O III] and several temperatures above the best-fit relation lie along the 1:1 relation. The data here has also a high scatter reflected in an intrinsic dispersion of 2116K.

Finally, we check how do the few values of T_e[N II] relates with the T_e[O III] temperature in the lower left panel of Figure 4.3. As we only have 5 data points here and no trends are observed, no relation is fitted between these variables. Instead, we observe that all values of T_e[N II] are present when T_e[O II] lies between 10000 and 15000K. In this range, the three lines plotted representing the 1:1 relation, photoionization models relation from PM17, and the local HII region relation by R21 agree in their predicted values for T_e[N II]. 2/5 galaxies in our sample agree with the relation from R21, but it is not possible to comment around which other relation the rest of the data lie due to the low amount of data points and the unknown scatter of the data. Furthermore, two galaxies exhibit values of T_e[N II] larger than T_e[O III] and makes more difficult the interpretation of this relation.

In summary, we found new temperature relations between T_e[O II] and T_e[O III] that disagree with the widely used G92 at high temperatures and agree very well with a density dependent relation of PM17 for $n_e = 250$ cm^{-3}. We find consistent T_e[S III] vs T_e[O III] relation with G92 models and a significant disagreement with the relations derived from local HII regions by B20 and R21. The few measurements of T_e[N II] agree with the relations from PM17 and R21, but we do not have enough data points to analyze the trend of this temperature with respect to T_e[O III].
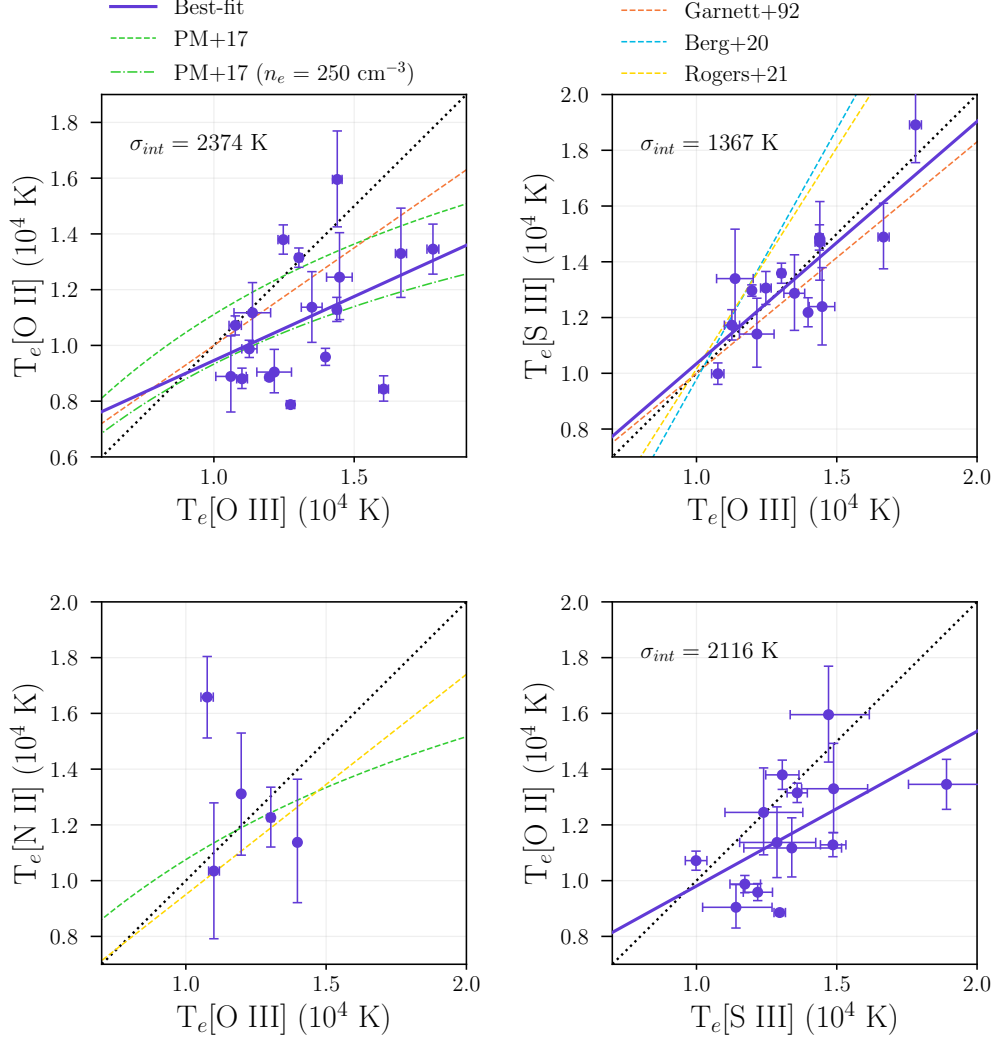
Figure 4.3: Temperature relations between T_e[O II], T_e[S III], T_e[N II], and T_e[O III]. Dark blue circles represents our measurements along with a solid line indicating the best-fit linear relations, including the estimated intrinsic dispersion in units of K for each case. All measurements are shown with 2σ errorbars. The 1:1 relation is indicated with a dotted black line in every panel. Comparisons with literature relations from Garnett (1992), Pérez-Montero (2017), Berg et al. (2020b), and Rogers et al. (2021) are shown as orange, green, blue, and yellow dashed lines. Additionally, a density-dependent relation outlined in Pérez-Montero (2017) between T_e[O II] and T_e[O III] is included in the upper left panel as a dot-dashed green line for a density of $n_e = 250$ cm^{-3}.

4.3 Calibration of Oxygen Abundance w.r.t. SELRs

In this section we present the results of the calibration between the strong emission line ratios and the oxygen abundance. Table E.1 contains the values of the oxygen abundance, the nitrogen abundance, and the N/O ratio according to the direct-method outlined in Section 3.7. The values of all the SELRs listed in Section 3.8 are included in Table E.2. We note that our sample of analogs have a metallicity ranging from 7.8 to 8.6, with a median value of $12 + \log(O/H) = 8.18 \pm 0.03$. On the other hand, the nitrogen abundance show lower values with a median of $12 + \log(N/H) = 6.66 \pm 0.05$. This predict a median of $\log(N/O) = -1.52 \pm 0.06$, however, the nitrogen abundance in this work is not measured from the difference between the nitrogen and oxygen abundance, but from its own equation described in Section 3.7. This suggest that the median ratio would be instead $\log(N/O) = -1.54 \pm 0.11$ that is consistent with the previous result considering the range of uncertainties. For further discussion on these values we refer to Section 5.1.

To derive the calibrations between SELRs and metallicities we explore the best-fit relations using the individual measurements for our 18 galaxies. We then bin the ratios and the abundance by taking the mean value in four metallicity bins shown in the lower section of Table E.1 and E.2. We used the binned data to observe the metallicity trends more clearly and check whether the fits from the individual data are able to reproduce them. For the fitting procedure we fit second order polynomials of the form:

$$y = a_0 + a_1 \cdot x + a_2 \cdot x^2 \tag{4.4}$$

where y is the ratio and $x = 12 + \log(O/H)$. This accounts for some known double-valued relations with metallicity, such as the R23 ratio. In cases where the trends are rather linear and also have linear relations described in literature we simply set $a_0 = 0$. This is the case of the N2, O3N2, O3O2, Ne3O2, S2, and O3S2 ratios, while the R2, R3, R23, R3N2, N2O2, and N2S2 are described by a polynomial of order 2. One thing to notice before proceeding with the fitting results is that the galaxies in our sample with the highest S/N spectra show extremely precise measurements of both the physical quantities involved in this study and the SELRs. This is the case of the sources J0021+0052, J1448−0110, and J2215+0002. The measurements made on these galaxies can reach about 10 times lower errors in the SELRs than the rest of the dataset making them dominate any regression weighted by the uncertainties in the data and leading to results that does not represent the trends observed. For the linear fits we used the LINMIX package as well as for the results of Section 4.2 since the method it uses is ideal to overcome the problem of the uncertainties. Unfortunately, the package only has regressions with a straight line implemented. Therefore, we implement a simpler but effective Bayesian regression with outliers (gaussian mixture) and intrinsic scatter to fit the polynomial calibrations of this work. We used the emcee package (Foreman-Mackey et al., 2013) to run MCMC simulations to report the best-fit parameters and intrinsic

scatter. Table 4.2 contain the best-fit parameters for each case including the scatter between the predicted values and the real measurements and the intrinsic scatter estimated from the regressions. Note that only the intrinsic scatter of the regressions performed with LINMIX are derived considering data in both the x and y direction. The rest of the estimations are considered as coming from the perturbations in the y direction only, i.e., scatter in the SELRs.

Table 4.2: Best-fit coefficients of the calibrations between SELRs and $12 + \log(O/H)$.

Ratio	a_0	a_1	a_2	σ_{RMS}	σ_{int}
N2	-8.112	0.790		0.227	0.278
R2	-151.672	36.458	-2.187	0.180	0.198
R3	-28.775	7.413	-0.464	0.060	0.067
R23	-1.677	0.746	-0.051	0.045	0.055
O3N2	10.586	-0.994		0.270	0.330
R3N2	-84.296	22.002	-1.398	0.297	0.333
N2O2	105.545	-26.006	1.587	0.254	0.289
O3O2	8.199	-0.918		0.141	0.173
Ne3O2	6.491	-0.838		0.155	0.190
S2	-5.901	0.571		0.148	0.183
O3S2	8.292	-0.765		0.190	0.232
N2S2	97.508	-24.089	1.480	0.201	0.225

Figure 4.4 shows the results of the metallicity calibrations derived in this work for the full list of SELRs introduced in Section 3.8. We observe that our data is, in general, highly scattered, but the binned data helps highlighting the underlying tendencies between the variables. Our linear relations follow really close the binned data showing good correlations with metallicity in general. Among the linear relations, the widely used N2 and O3N2 ratios have a visually larger scatter in Figure 4.4 which is supported by their values of scatter of Table 4.2. The ratios O3O2, Ne3O2, S2, and O3S2, exhibit tighter correlations, being O3O2 outstandingly well constrained with the lowest scatter compared to the rest of the linear relations. Regarding the polynomial relations, we observe that our results are far from providing robust constraints on the shape of the calibration. The ratios R2 and R3 admit the polynomial regression with a close description of a portion of the data, but they seem to fail in the metallicity limits. R3 drops down considerably for $12 + \log(O/H) < 7.8$ which is the lower limit of our data. On the other hand, R2 drops down at the high metallicity end where the last bin appears to be insufficient to lift up the relation. Despite these caveats, R2 and R3 show the smallest scatters after the R23 ratio. We discuss about the implications and usefulness of these results in Section 5.3.
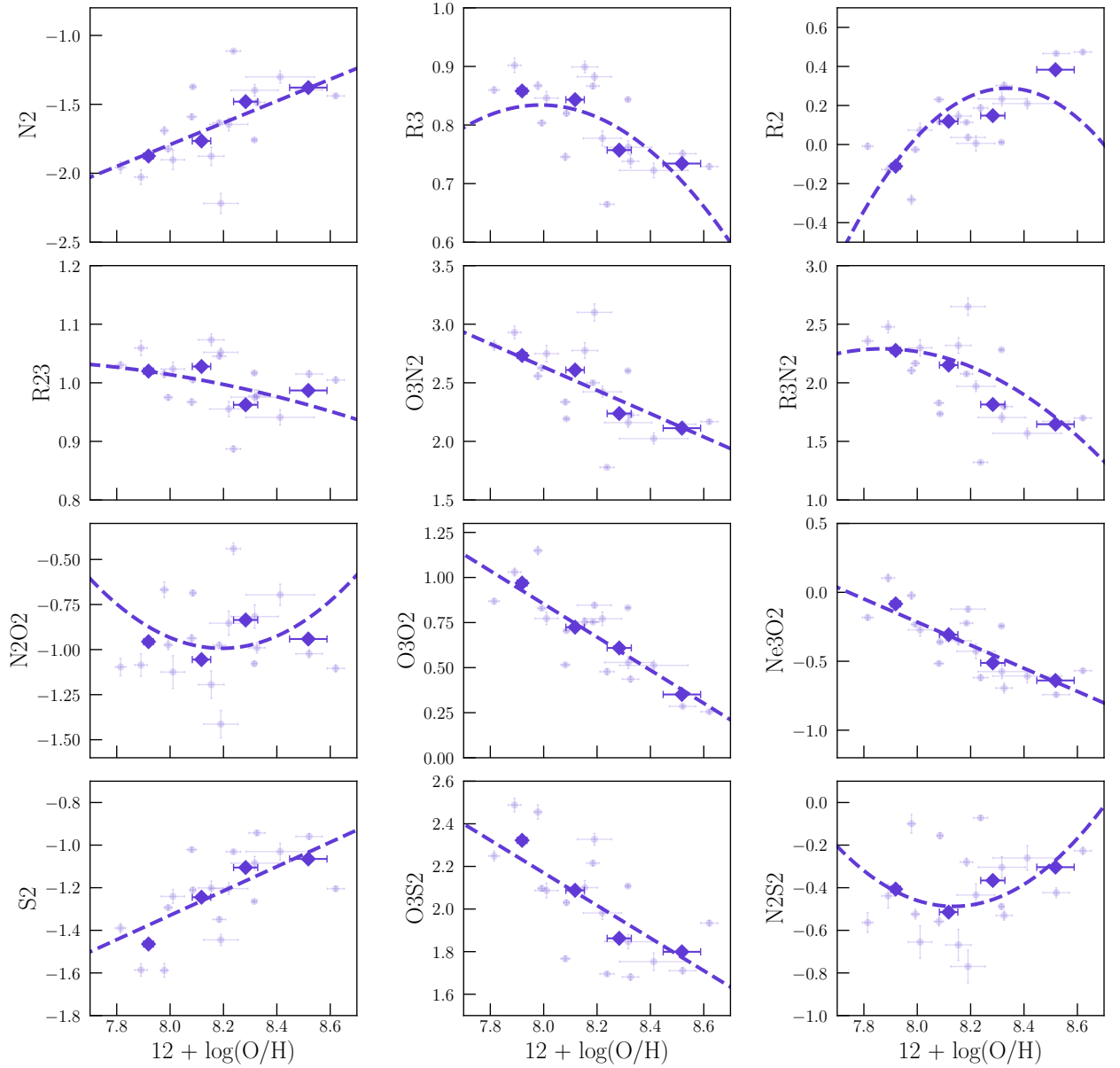
Figure 4.4: Calibrations of relations between the full list of SELRs and $12 + \log(O/H)$ derived with the local analogs in this study. The individual measurements of the ratios and oxygen abundance are shown as faded dark-blue points with errorbars of 5σ and 2σ, respectively. Dark-blue diamonds indicate the metallicity-binned data with 2σ in both directions. The dashed line in each panel represent the relations from the best-fit parameters of Table 4.2.

The R23 ratio shows little or no correlation with metallicity. This is due to the range of abundances measured in the local analogs of this work. They all fall in a metallicity range where the R23 ratio, known for their double-valued function, show the turnover behavior (Nagao et al., 2006; Maiolino et al., 2008; Curti et al., 2020; Sanders et al., 2021). The binned data remains flat around R23 ~ 1.0 and the best-fit relation ends in a wide open quadratic polynomial due to the little constrain. This ratio shows the smallest scatter of all our derived relations followed by R3 and the linear O3O2. Finally, the remaining N2O2 and N2S2 ratios also show negligible correlations with the metallicity both by the individual values

distributed as a cloud of points and the binned data around ~ -1.0 for N2O2 and ~ -0.4 for N2S2. The quadratic relations derived for these ratios are very steep and partially resemble the individual points, leading to larger scatters compared to the rest of the polynomial fits.

4.3.1   Local Star-forming Galaxies

Figure 4.5: Comparison of the calibrations derived in this work against calibrations based on $z \sim 0$ HII regions. The markers, lines, and transparency of our data follows the same format than in Figure 4.4. Colored faded lines correspond to local relations from Denicoló et al. (2002); Pettini and Pagel (2004); Tremonti et al. (2004); Nagao et al. (2006); Maiolino et al. (2008); Marino et al. (2013); Curti et al. (2020), and Sanders et al. (2021). Only relations between metallicity and N2, R3, R2, R23, O3N2, R3N2, N2O2, O3O2, and Ne3O2 are included.

We compare our results with some of the most used empirical calibrations from the literature derived from samples of HII regions (Denicoló et al., 2002; Pettini and Pagel, 2004) and star-forming galaxies (Tremonti et al., 2004; Nagao et al., 2006; Maiolino et al., 2008; Marino et al., 2013; Curti et al., 2020; Sanders et al., 2021). These relations often had to also opt for using photoionization models to complement their sample and span a wider range of metallicities. In Figure 4.5 we observe that our results effectively separate from most of the $z \sim 0$ calibrations. The N2 ratio in this work exhibit a shallower slope with metallicity compared to local calibrations, although the low metallicity end agree very well. A sub-sample of four

galaxies in this study seems to follow closely the relations presented by Pettini and Pagel (2004) and Marino et al. (2013), but constitutes only 22% of our sample consistent with such predictions while the other 78% of the sample is systematically shifted to higher metallicities by 0.2 dex at N2 $\gtrsim -1.5$. The R3 ratio shows also a significant separation with local calibrations with a best-fit relation lying above the predicted values from Maiolino et al. (2008); Curti et al. (2020); Sanders et al. (2021). The scatter of R3 in this work is consistent with the 0.07 intrinsic scatter of the calibration from Curti et al. (2020) that is the closes to this ratio for the metal-poor part of our sample, but the differences increases considerably towards high metallicity. Maiolino et al. (2008) and Curti et al. (2020) are able to reproduce an important part of our data throughout the entire range of metallicities. However, our sample still appears clumped below at the intermediate range of our data $(12 + \log(O/H) \sim 8.2)$. There is no much gain in comparing the shapes of the relations for the R2 ratio since it is poorly constrained above $12 + \log(O/H) = 8.4$. That is also the case for the full range of metallicities in the R23 panel where our relation remains extremely flat compared to the steep relation from Tremonti et al. (2004) and lie above the rest of the literature calibrations. The shape gives no information, but the R23 of our analogs appears to be systematically larger than those of local HII regions suggesting a different normalization than literature relations. The O3N2 ratio seems to inherit the behavior of N2 with a less steep relation than in literature and a clear separation towards high metallicities. The R3N2 deviate very well from the calibrations of Nagao et al. (2006) and Maiolino et al. (2008), suggesting a higher normalization in this relation and the difference increase with metallicity. However, this ratio shows one of the largest scatters both visually and in Table 4.2. The nonexistent correlation between the N2O2 ratio and metallicity aforementioned leads to a really close quadratic polynomial compared with the Nagao et al. (2006) relation that has a positive and smoothly increasing correlation. Many literature calibrations fall below the tight relation found in this work for the O3O2 ratio which predict higher metallicities for fixed O3O2. Finally, the Ne3O2 shows a similar slope than the relation in Maiolino et al. (2008), but it is shifted to drastically higher metallicities for fixed Ne3O2 for the whole range of values of $12 + \log(O/H)$, reaching differences of $\gtrsim 0.3$ dex in metallicity.

Overall, all relations derived in this work show systematically larger metallicities than those predicted by the relations calibrated with local HII regions and star-forming galaxies. The differences appear to increase towards the high metallicity regime of our data in the linear relations compared in Figure 4.5. Excluding the portion of 22% of our data consistent with local relations (See the points with low errorbars in the N2, R3, O3N2, and R3N2 panels of Figure 4.5) and some fraction of the relations that provide useless comparisons such as R23 and N2O2, most of the linearly tight relations provide significant differences with the predictions of calibrations done with galaxies in the local Universe. We discuss the validity and impact of these results in Section 5.3.

4.3.2 High-z Analogs
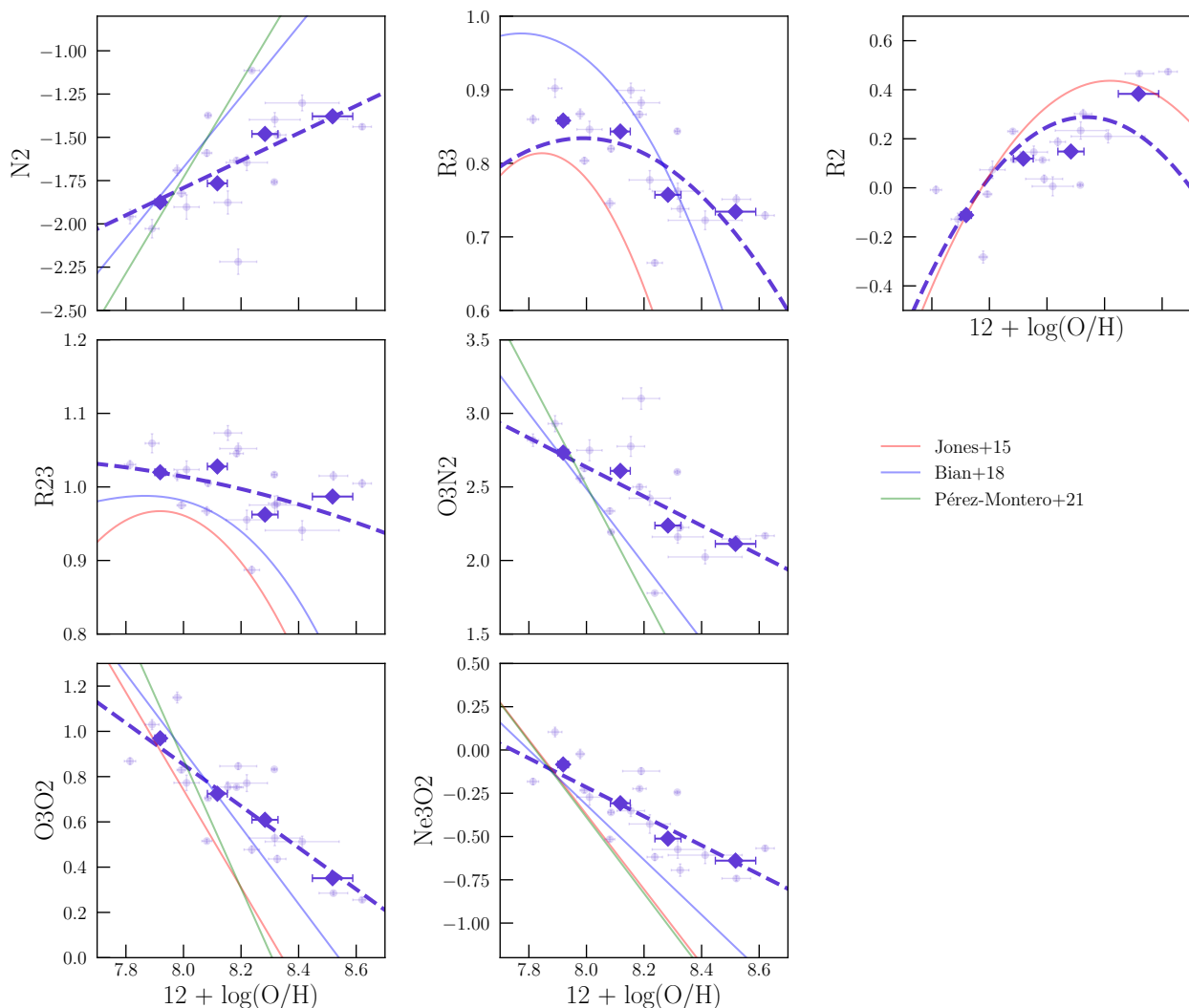
Figure 4.6: Comparison of the calibrations derived in this work against literature based on other samples of local analogs. The markers, lines, and transparency of our data follows the same format than in Figure 4.4. In this case, the relations are compared to galaxies at $z \sim 0.8$ from Jones et al. (2015), the local SDSS analogs relations from Bian et al. (2018), and extreme emission line galaxies (EELGs) from Pérez-Montero et al. (2021) shown as red, blue, and green solid faded lines. The only ratios available for comparison are N2, R2, R3, R23, O3N2, O3O2, and Ne3O2.

We compare our calibrations with literature relations based on samples of local analogs of high-z galaxies. This is done in Figure 4.6 where we face our results against the calibrations based on 1) star-forming galaxies at $z \sim 0.8$ (Jones et al., 2015), 2) stacked spectra of SDSS local analogs selected with the same criteria described in this work (Bian et al., 2018), and 3) a sample of extreme emission-line galaxies (EELGs) (Pérez-Montero et al., 2021). In this case, we were able to compare the ratios N2, R2, R3, R23, O3N2, O3O2, and Ne3O2. Once again, the N2 ratio show a more shallower slope with respect to the metallicity compared to relations of Bian et al. (2018) and Pérez-Montero et al. (2021). These relations have similar

trends than that of Pettini and Pagel (2004) and Marino et al. (2013) as it can be appreciated in Figure 4.6 where the same points of our data consistent with the local relations are following the trends from SDSS analogs and EELGs. Interestingly, the majority of our sample of analogs deviates from the trends explored by (Bian et al., 2018) who selected galaxies under the same criteria from (Bian et al., 2016). Those relations deviate by $0.05 - 0.1$ dex compared to local HII regions and our relation in N2, for instance, shows a large difference of about 0.25 dex in metallicity for galaxies with $N2 = -1.5$. The R3 ratio, on the other hand, is more consistent with literature relations by leaving most of our dataset between the Jones et al. (2015) and Bian et al. (2018) relations up to $12 + \log(O/H) = 8.4$, which is the actual limit of validity of Bian et al. (2018). Our data sample reaches a few values above this limit giving a more flatter quadratic calibration of R3. The R2 ratio results very similar to the Jones et al. (2015) calibration, although the difference between the relations increases up to 0.2 dex in the R2 ratio at higher metallicities. Our best-fit relation is not able to describe the metal rich bin in the right-most part of the R2 vs $12 + \log(O/H)$ plot, unlike the Jones et al. (2015) calibration that predict a more rapidly changing polynomial. The calibrations of the R23 ratio are closer to describe the levels of our measured R23 than the relations from $z \sim 0$ HII regions. However, the trends of the quadratic polynomial are still very different due to the flat relation predicted by our data. The O3O2 and Ne3O2 ratios show closer results to those from the literature in contrast to the O3N2 ratio that shows a similar difference than N2. The big difference again emerges from the fact that previous relations do not reach the high metallicity bin of our data for the values of the ratios involved, being (Bian et al., 2018) relations being the closest to our data until $12 + \log(O/H) \sim 8.3$ in O3O2 and $12 + \log(O/H) \sim 8.1$ in Ne3O2. Our relations there predict a flatter slope in the ratios vs metallicity plane, meaning that literature relations would be underestimating the metallicity by about 0.2 dex by $O3O2 \sim 0.4$ and 0.3 dex by $Ne3O2 \sim -0.5$. The O3O2 and Ne3O2 relations from Jones et al. (2015) and Pérez-Montero et al. (2021) are very similar between them and consistent with the ranges of values of Bian et al. (2018) in the low metallicity end.

We therefore found that our analogs hold big differences not only with calibrations based on local HII regions but also with relations based on distinct populations of galaxies whose ionization conditions are more extreme (Bian et al., 2018; Pérez-Montero et al., 2021) or galaxies of the epoch when the Universe had about half his age Jones et al. (2015). We explore the reason behind these differences and the impact they have in metallicity estimations of high-z galaxies in Section 5.3.

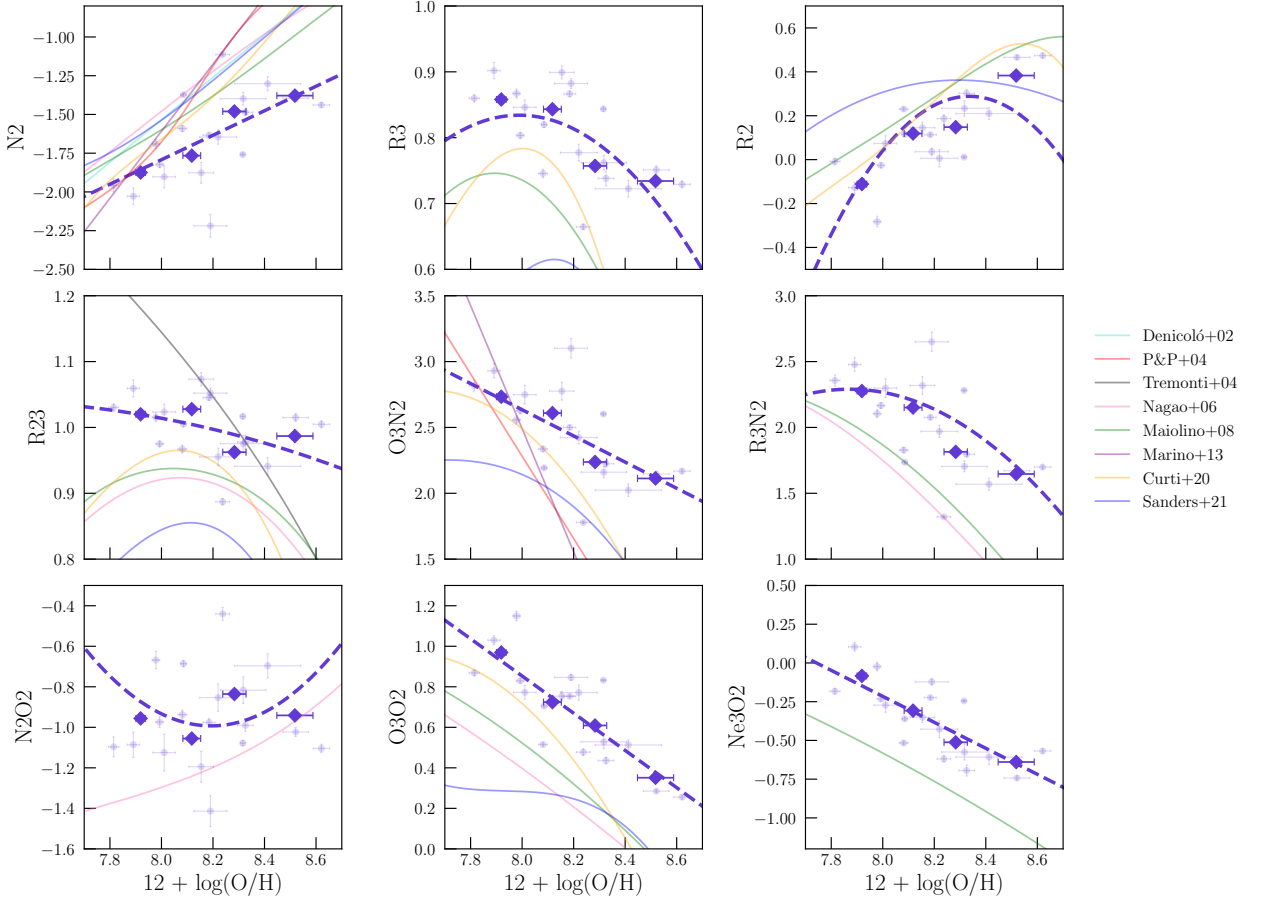### 4.3.3 Photoionization Models
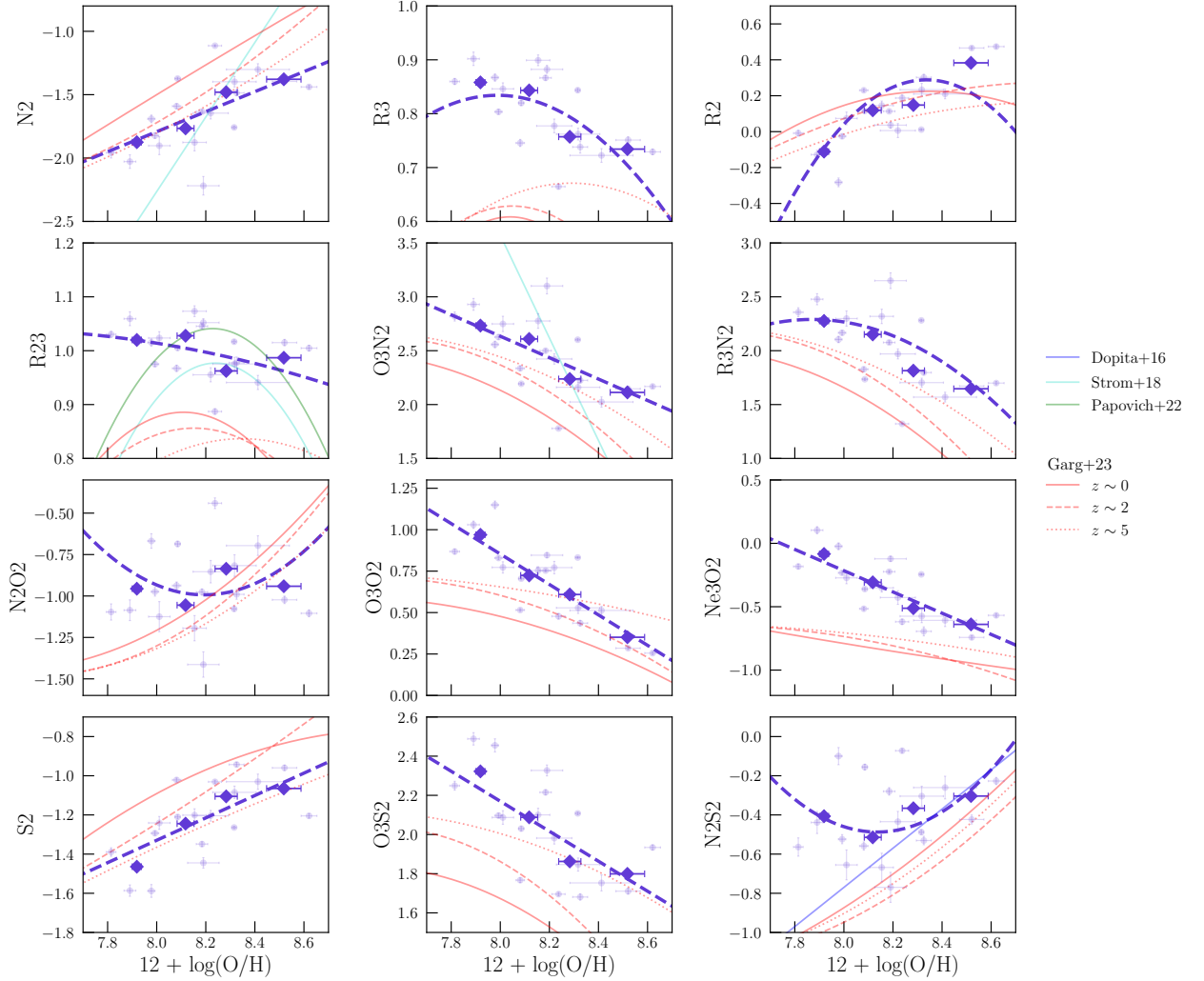
Figure 4.7: Comparison of the calibrations derived in this work against calibrations based on photoionization models. The markers, lines, and transparency of our data follows the same format than in Figure 4.4. Relations are plotted along with models from Dopita et al. (2016); Strom et al. (2018), and Papovich et al. (2022). Furthermore, models from Garg et al. (2023) for galaxies at $z = \{0, 2, 5\}$ are included as solid red, dashed, and dotted lines, respectively. In this case, all the ratios are available for comparison with Garg et al. (2023).

One last relevant comparison that we can perform in this study is to face our relations against photoionization models. In Figure 4.7 we plot our relation among literature calibrations from Dopita et al. (2016), Strom et al. (2018), Papovich et al. (2022), and Garg et al. (2023). In this case, we have available comparisons with all the ratios defined in this study. The Strom et al. (2018) calibration for N2 and O3N2 is very different to our derived trends, showing very steep relations of ratio vs metallicity. The pairs (R23, $12 + \log(O/H)$) measured in this work are consistent with the turnover part of the relations from Strom et al. (2018) and Papovich et al. (2022). The N2S2 ratio presented by Dopita et al. (2016) matches almost exactly the best-fit relation found in this work for galaxies with $12 + \log(O/H) > 8.3$,

but the separation increases enormously towards lower metallicities owing to the flat trend traced by the binned data. Garg et al. (2023) used a combination of cosmological models and photoionization models to establish evolving empirical relations with redshift which are tested in this study by comparing the solutions at $z = 0, 2$, and 5 with our local analogs. The red solid line representing the $z = 0$ calibration is the farthermost curve in most of the cases, while the $z = 2$ and 5 calibrations get closer to our measurements. The models of R3 and R23 are far from the measured values falling almost out of the range of values of these ratios in their corresponding panels. The R2 relations from Garg et al. (2023) predict a flatter behavior compared to the increasing trend of our data to high-metallicities and the ranges of values between $12 + \log(O/H) = 8.0$ and 8.4 agree very well with the three redshift curves due to the very small variation between them. Some models approximate very well the relations found in this work as one increases the redshift of the relation. This is the case of N2, O3N2, R3N2, S2, and O3S2, where the closest match to our relations are the $z = 5$ calibrations. The match between this calibration is outstanding for $12 + \log(O/H) < 8.4$ in N2 and the full range of metallicities for S2. The high-metallicity end of O3O2 and O3S2 agree well with the $z = 2$ and 5 from Garg et al. (2023), respectively. On the other hand, although the shape of the trends are similar, the normalization is systematically shifted in the O3N2 and R3N2 relations, making them unable to predict our measurements. The Ne3O2 ratio shows little or negligible evolution in Garg et al. (2023) models, separating the relations significantly from our calibration. Finally, the N2O2 and N2S2 ratios once again have an unfair comparison due to their little correlation with metallicity. Not only the trends suggested by the models are different than our data, but the evolution appears to separate even more from the measured ratios at fixed metallicity from $z = 0$ to 5.

Our results constitute a good constraint to the photoionization models thanks to the detailed amount of SELRs measured from our sample. A substantial fraction of the SELRs involved in this study are consistent with the evolutionary trend of the models from Garg et al. (2023). We comment on the role of our galaxies as indicators of metallicities in high-z galaxies suggested by the comparison with these models in Section 5.3.

Chapter 5

Discussion

In this chapter we discuss about the implications of the results found in Chapter 4. Section 5.1 analyzes our results along with ionization diagnosis to discuss about how good is the sample as local analogs of high-z galaxies. Section 5.2 explore the impact of the temperature relations in this work on measuring metallicities at high-z using the direct-method with a partials sets of emission lines as in literature. Finally, Section 5.3 discuss about the validity of our new metallicity calibrations with SELRs and the predictions of chemical abundance studies in the distant Universe.

5.1   The Ionization Nature of the Sample of Local Analogs

We explore the resemblance of the ionizing conditions of the ISM of our sample of local analogs given the results presented in Section 4.1. For this, a full perspective of what our sample consist of is necessary to have a full pictured analog scenario. The results of Section 4.1 imply that the local analogs consist of a sample of low mass galaxies with a median of $\log(M/M_\odot) = 8$. The local mass-metallicity relation derived in Tremonti et al. (2004) predicts a metallicity of $12 + \log(O/H) \sim 8.186$ which is consistent with the median metallicity of the local analogs $12 + \log(O/H) = 8.187 \pm 0.017$. This result suggest that the analogs selected based on the shifts of the ISM conditions in the BPT diagram tends to select also low-mass and relatively metal-poor galaxies in the local Universe. The predicted SFR from the SED models in our sample is really high for the ranges of stellar mass involved, leading to very high sSFR compared to galaxies in the main sequence at $z \sim 2$ (Rodighiero et al., 2011). However, the SFR might be one of the parameters with more caveats that we measure. First, the optical photometry alone is not enough to constraint the star-formation activity accurately ignoring the information that other bands could provide. Furthermore, the SFH used to describe the SED of the local analogs include a recent epoch of bursty star-formation that increases the instantaneous measure of the SFR. Indeed, if we take the averaged SFR over the last 100 Myrs provided by `CIGALE` we find that the SFR is decreased by $\delta \log(SFR) = 0.85$ and would resemble the properties of main-sequence galaxies at $z \sim 2$. The levels of the instantaneous SFR goes beyond the main sequence of galaxies at $z \sim 4$ (Schreiber et al., 2015) which

makes these results even more suspicious. These results suggest that the local analogs could possibly constitute a sample of very active star-forming galaxies at least compared to the local galaxies in the main sequence.
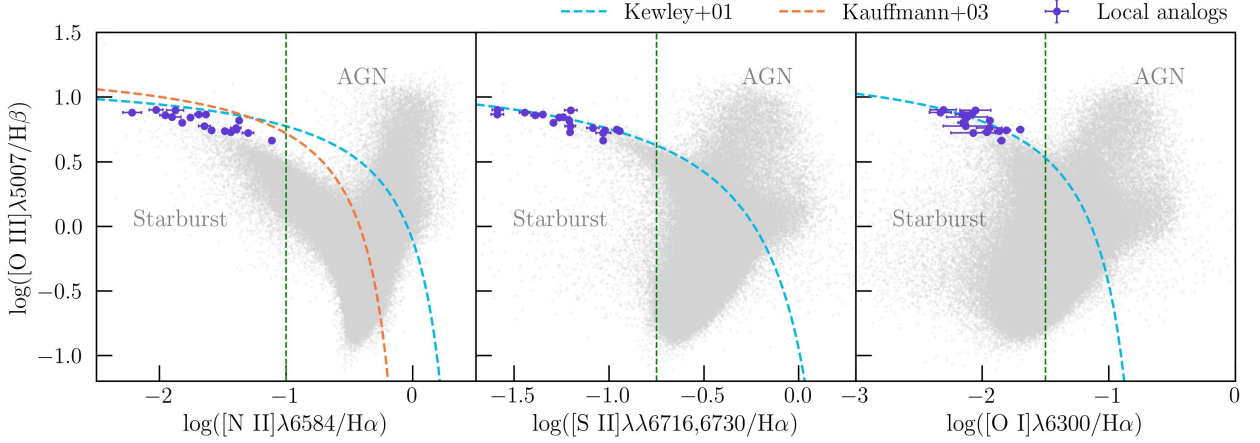
Figure 5.1: BPT diagnosis of local analogs. The left, middle, and right panels shows the [N II], [S II], and [O I]-based versions of the BPT diagram (Baldwin et al., 1981; Veilleux and Osterbrock, 1987) for galaxies from SDSS. Our local analogs are shown as dark-blue points with 2σ errorbars, while SDSS galaxies are represented by gray dots. All panels contains the demarcations defined by ionization models from Kewley et al. (2001), including the Kauffmann et al. (2003) relation in the left panel. The vertical green dashed lines indicate the limits from which to the left the emission from AGNs and fast shocks are significant (Kewley et al., 2019)

To confirm whether our sample is dominated by active star-formation and to check if the conditions of the ISM resemble those of galaxies at high-z, we discuss about the results of the physical properties of the gas of the local analogs. To aid the analysis of the results of electron density and ionization parameter of Section 4.1, Figure 5.1 shows the three versions of the BPT diagnostic diagrams for galaxies in this work. The BPT-N2 diagram in the first panel was the used to select the sample of local analogs (Bian et al., 2016). The local analogs cluster in a sequence-like shape below the limit of the starburst models (Kewley et al., 2001) and show $\log([\text{N II}]\lambda 6584/\text{H}\alpha) < -0.5$, satisfying two of the three restrictions of the selection criteria (See Section 2.2). In particular, our sample exhibit even lower nitrogen emission where $\log([\text{N II}]\lambda 6584/\text{H}\alpha) < -1.0$. At these ratios, models suggest that the AGN excitation leads to $\log([\text{O III}]\lambda 5007/\text{H}\beta) > 1.0$ (Kewley et al., 2019), which is not observed in our galaxies. Along with the demarcations from Kewley et al. (2001) and Kauffmann et al. (2003) suggesting star-formation as the source of excitation, we can discard any possible AGN contamination in our sample. Nevertheless, fast-shocks can still reach down to $\log([\text{N II}]\lambda 6584/\text{H}\alpha) = -1.5$ at the same range of oxygen strength measured in our analogs around 0.5 and 1.0 in the y-axis. For this reason, we include the BPT-S2 and BPT-O1 diagrams that can help separating other types of excitation sources. By checking the possible values of the grids of photoionization models in Figure 11 of Kewley et al. (2019) we notice that excitation by fast-shocks is more important for $\log([\text{S II}]\lambda\lambda 6716,6730/\text{H}\alpha) \gtrsim -0.75$ and $\log([\text{O I}]\lambda 6300/\text{H}\alpha) \sim -1.5$. Our sample of analogs are all clustered below these values

and are consistent with the Kewley et al. (2001) demarcations as well, lying well inside the sequences of star-forming galaxies. Therefore, the combination of the three BPT diagrams suggest that the source of excitation in our local analogs is pure star-formation activity as expected from the selection criteria.
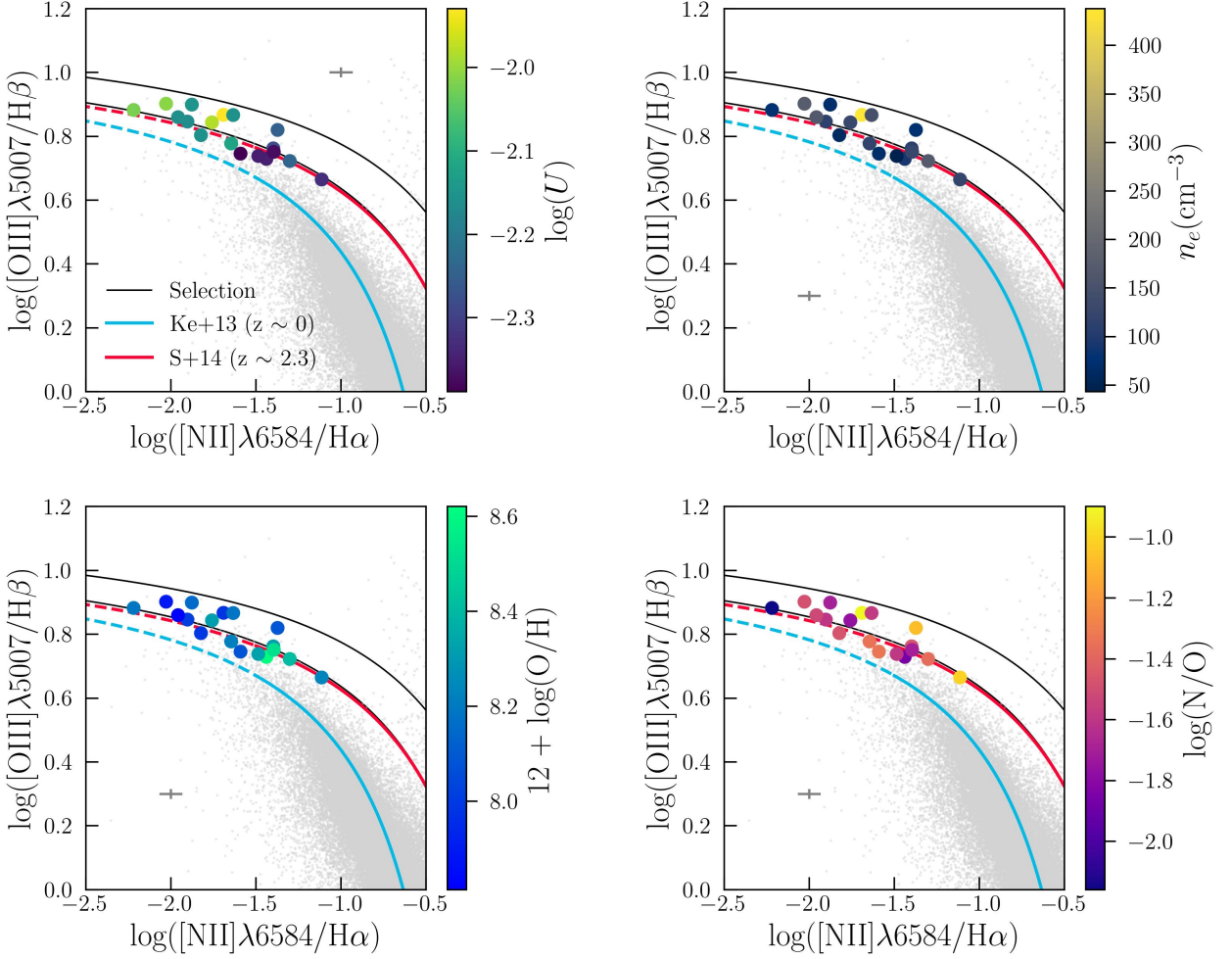
Figure 5.2: Zoom in to the BPT-N2 diagram of our local analogs color-coded by distinct physical properties. Gray cross in each panel shows the exaggerated 10σ uncertainty of our measurements. As well as in Figure 5.1, the gray dots represent the position of SDSS galaxies in the diagram. The upper left and right panels show the position of our analogs as circles with no errorbars color-coded by the ionization parameter and electron density, while the lower left and right panels are color-coded by the metallicity and the N/O ratio, respectively. Each panel includes the selection criteria defined in Section 2.2 (Bian et al., 2016). The red and blue solid lines show the *abundance main sequence* of star-forming galaxies at $z = 0$ (Kewley et al., 2013a) and $z \sim 2.3$ (Steidel et al., 2014), respectively. An extension of these relations to lower values of $\log([\text{N II}]\lambda6584/\text{H}\alpha)$ is indicated with dashed lines of the same color.

Assuming that star-formation is the dominant source of excitation of the analogs suggested by the BPT diagnosis, we need to explore further which of the properties of the galaxies can lead to the shifts in the diagrams at higher-z. In Figure 5.2 a zoom in into the region where our analogs lie is shown. First, we confirm the shift to higher values of [O

III]$\lambda 5007/\mathrm{H}\beta$ compared to the star-forming abundance sequence of galaxies at $z = 0$ (Kewley et al., 2013a). Instead, our galaxies clump very well around the relation found by Steidel et al. (2014) of galaxies at $z \sim 2.3$. Most of our analogs match the selection criteria, but a few sources lie below the lower limit that was defined to avoid contamination from normal star-forming galaxies at $z = 0$, but they are still in the range of variation of galaxies at $z \sim 2.3$ considering the scatter of 0.12 found by Steidel et al. (2014). The position of the sources in the diagram supports the idea of the analogs as good laboratories to probe the properties of high-z galaxies.

As discussed in Section 2.1, two properties that can drive shifts in the BPT diagram are the electron density and the ionization parameter. Results from Section 4.1 show that the gas in our galaxies have electron densities between the median values of the local Universe and high-z galaxies (See Figure 4.1). Assuming that our galaxies are good analogs, our results suggest that the electron density might have a minor contribution to this shift, owing to the fact that these galaxies do not need the same high values of n_e of galaxies at $z \sim 2.3$ (Sanders et al., 2016) to reach the same level of strength in the [O III]$\lambda 5007/\mathrm{H}\beta$ ratio given that they follow closely the relation found in Steidel et al. (2014). Furthermore, we find no evidence of variation to lower [N II] emission with electron density as shown in the upper right panel of Figure 5.2, suggesting that variations in the x-direction of the BPT are not likely to be driven neither by the electron density. On the other hand, the difference in ionization parameter with local galaxies and even the SDSS analogs studied by Bian et al. (2016) is more drastic, putting this variable under scope as a driver of the high excitation of the gas. The higher ionization parameters in our sample indicate that the hardness of the ionization field or the luminosity of the stellar population is enhanced compared to galaxies in the local Universe. By exploring grids of models with different ionization conditions, Steidel et al. (2014) suggested that the shifts in the BPT diagram not only could be driven by a higher ionization parameter, but it could also contribute on shaping a sequence in high-z star-forming galaxies. Our results indeed appear to show a sequence in ionization parameter as it can be appreciated in the upper left panel of Figure 5.2, where higher values of $\log(U)$ are found with decreasing [N II]$\lambda 6484/\mathrm{H}\alpha$ and vice versa. The ionization parameter is still sensitive to changes in metallicity as we can see in the lower left panel of Figure 5.2 where the metal-rich galaxies in our sample appear to have stronger [N II] emission with respect to $\mathrm{H}\alpha$, although the trend is less evident, this would support the inverse proportionally between metallicity and the ionization parameter. The models from Steidel et al. (2014) get tight when they assume a linear relationship between metallicity and the N/O ratio instead of considering constant N/O ratio near solar values. It is crucial to constrain the N/O ratio to avoid degeneracies with other physical parameters in models when reproducing the strength of the [O III] and [N II] lines in the BPT diagram. This encouraged us to investigate the relation between the oxygen abundance and the N/O ratio. While the metallicity shows a small trend in our data, the lower right panel of Figure 5.2 shows no clear evidence of a sequence in N/O values along the position of our analogs in the BPT diagram. This imply

that there is no clear relation between N/O and O/H.

Indeed Figure 5.3 supports this statement by studying precisely the relation between these abundances. As observed in Section 4, the sample of analogs exhibit sub-solar metallicities with all values below $12 + \log(O/H) = 8.69$ which is the adopted solar oxygen abundance in this work (Asplund et al., 2021). Three sources with relatively low metallicity in our sample have a nitrogen abundance near the solar $\log(N/O)$, while the majority of our sample is well located around the primary regime of nitrogen production (Andrews and Martini, 2013). We observe that there is no clear correlation between N/O and O/H abundances as they mostly populate the primary regime where they agree with metal-poor galaxies in the local Universe (Izotov et al., 2006). Although there are differences with N/O ratios found in local HII regions located mainly in the secondary regime of nitrogen production (Berg et al., 2020a), the lack of correlation with O/H suggest that this parameter does not drive significant shifts in the line ratios of the BPT diagram of the local analogs in this work. It is noteworthy that most of our analogs agree with the abundance plateau of $\log(N/O) \simeq -1.5$. This is the so-called primary regime of nitrogen production where galaxies are creating nitrogen from intermediate-mass stars in a scenario where the gas has not been enriched enough to use carbon to catalyze nitrogen production. Figure 5.3 act as a clock of elementary production in galaxies where we would expect young systems with metal-poor gas lying in this primary regime (Henry et al., 2000). These results support the quality of our analogs as the expectations of the early Universe is that the ISM is less enriched because galaxies would be building significant part of their mass from metal-poor gas and still haven had enough time to form more stars from metal-rich gas originated by stellar feedback.

Since our sample is not abundant, our implications lack of statistical significance, but provide a valuable insight into the trends of galaxies at high-z that cannot be achieved with the same robustness due to limited sets of emission lines in the distant Universe. Bian et al. (2020) compared the N/O ratio and oxygen abundance of a sample of stacked spectra of local analogs selected with the same method than this work against SDSS galaxies. They found that the local analogs are in average around $N/O = -1.43$ and local SDSS galaxies at $N/O = -1.53$. The exact comparison should be made by binning our individual analogs and compare directly with Bian et al. (2020) results, but as we mentioned, our galaxies are clustered around the N/O plateau at -1.5 and we expect the average to do so. According to Bian et al. (2020), a difference above 0.2 dex should exist compared to local SDSS galaxies for N/O to have a significant contribution on shifting the position of the galaxies to the $z \sim 2.3$ locus in the BPT-N2 diagram. Thus, our results confirm that the N/O ratio and electron density have a minor contribution on driving the hard ionization conditions on sample, being the ionization parameter and metallicity the most sensitive characteristics indicating the possible sequence suggested by Steidel et al. (2014).
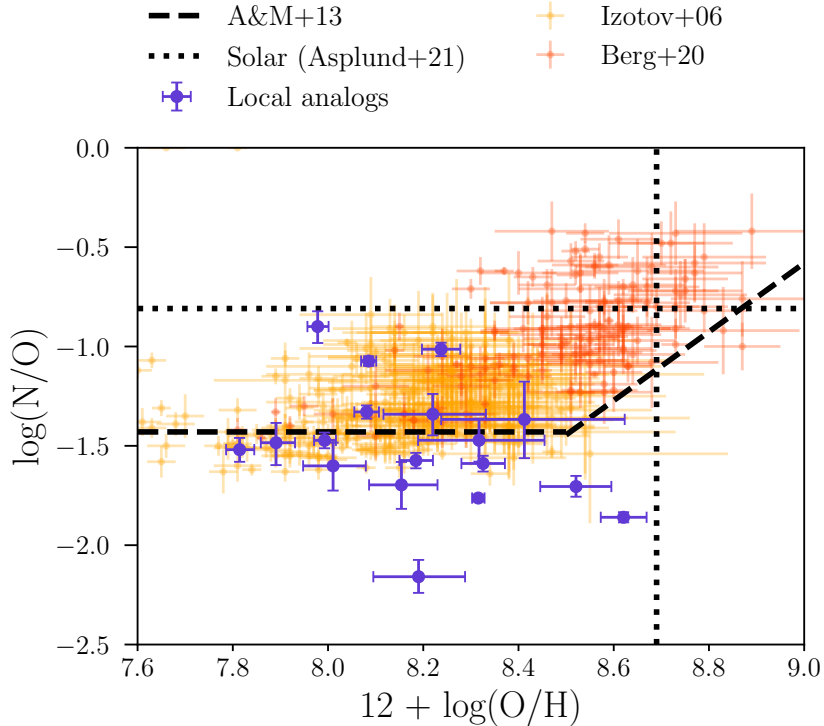
Figure 5.3: N/O ratio as a function of $12 + \log(\mathrm{O/H})$. The measurements of the local analogs in this work are shown as dark-blue circles with 3σ errorbars for appreciation. Yellow dots with errorbars represent the measurements of metal-poor galaxies from SDSS at $z = 0$ (Izotov et al., 2006), and red dots with errorbars are HII regions from local galaxies of the CHAOS Survey Berg et al. (2020a). The black-dotted line indicates the solar abundances from Asplund et al. (2021). The black dashed lines dennote the primary and secondary regimes of nitrogen production (Andrews and Martini, 2013).

5.2   Implications of Temperature Relations

The temperature relations derived in this work and presented in Section 4.2 not only provide a new benchmark for estimations of the metallicity in galaxies at high-z, but also gives some insights into their physical conditions. One aspect of this is the good agreement between the $\mathrm{T}_e[\mathrm{O\ II}]$ vs $\mathrm{T}_e[\mathrm{O\ III}]$ relation derived in this work and the density dependent relation of PM17 for an input density of $n_e = 250$ cm^{-3}. In the previous section, we already assessed the role of the density as a trigger for higher ionization conditions in the ISM of our galaxies by showing that it is not the main responsible of the evolution in the BPT diagram. Here, we compare the effect of density variation in the temperature relation between $\mathrm{T}_e[\mathrm{O\ II}]$ and $\mathrm{T}_e[\mathrm{O\ III}]$.

Figure 5.4 shows the measured pairs of $\mathrm{T}_e[\mathrm{O\ II}]$ and $\mathrm{T}_e[\mathrm{O\ III}]$ as well as in Figure 4.3, but including literature predictions of how the relation between these variable changes with density. We observe that there is no correlation at all due to the fact that very dark-blue circles with low electron density can exhibit really low values of $\mathrm{T}_e[\mathrm{O\ II}]$ in the regime where
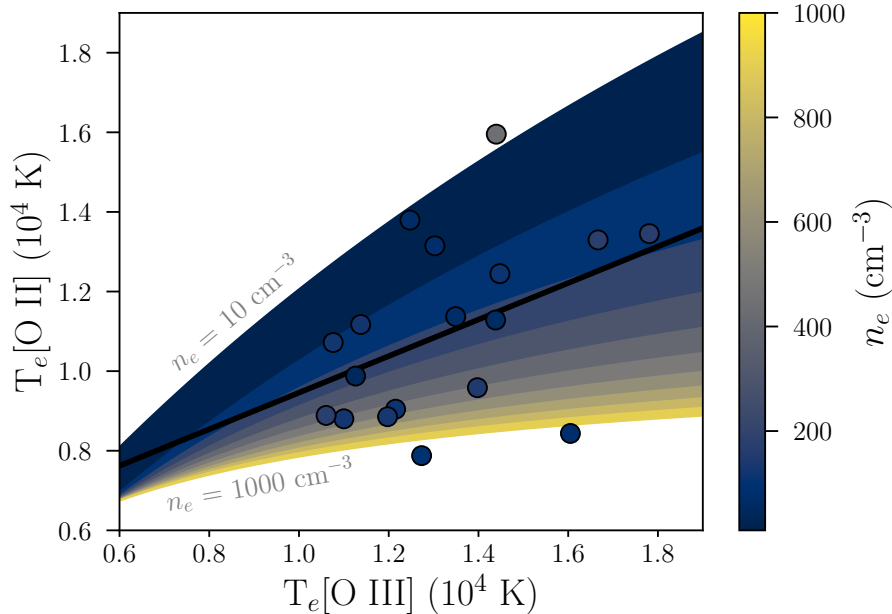
Figure 5.4: T_e[O II] as a function of T_e[O III] for our local analogs compared to predicted relations from density variations by (Pérez-Montero, 2017). Circles represent our measurements without errorbars and color-coded by the electron density. Colored regions follow the same color-code than our data points in intervals of 100 cm^{-3}. The first interval covers from 10 to 100 cm^{-3} since a value of 0 is not physical.

the PM17 relation should hold for galaxies with $n_e = 1000$ cm^{-3}. As the majority of our sample have values around $n_e = 100$ cm^{-3} a fraction of our data points agree well with the colored regions. The combination of these points plus the low density and low T_e[O II] results makes our predicted best-fit relation to drop down and be consistent with $n_e = 250$ cm^{-3} as shown in Figure 4.3. This imply that the role of the electron density in shaping temperature relations of high-z galaxies is little understood yet by the literature and our results do not constitute a helpful test due to the fact that our galaxies have an approximately uniform level of electron densities around $n_e = 100$ cm^{-3}. Even more, the galaxy in our sample with the highest electron density J0240-0828 exhibits the highest T_e[O II] measured, contrary to the predictions from PM17. Having discussed this, we now can go for the implications that our derived relation has for high-z studies.

Many studies of metallicities of galaxies at high-z do not have good detections of the [O II]$\lambda\lambda$7319,7331 doublet, and therefore, they cannot estimate directly T_e[O II] and the singly ionized oxygen abundance O$^+$/H$^+$ (Christensen et al., 2012; James et al., 2014; Sanders et al., 2016). Instead, they use the temperature relation between T_e[O II] and T_e[O III] based on photoionization models outlined by G92. We assess the quality of our derived temperature relation by using it to predict the oxygen abundance and compare it with G92 which is the most widely used relation in the literature. Figure 5.5 shows the predictions of these temperature relations. We observe that there is a very good agreement between the

two relations and the real values of metallicity for galaxies with $12 + \log(O/H) \lesssim 8.0$. For metallicities in the range between 8.0 and 8.4, the G92 relation shows systematically larger estimated metallicities while the predictions from our relation is in close agreement with the real values (Except for the point at 8.2 away from the trend). At higher metallicities the relations depart from each other with larger values from G92 and lower values from our relation compared to the real values of our galaxies. Again, an exception is the galaxy with the highest metallicity in our sample at $12 + \log(O/H) \sim 8.6$ where we see that our data departs from the 1:1 relation, supporting the idea of the questionable validity of T_e-based metallicities in the high metallicity regime, although it has been proposed to apply above the Solar abundance $12 + \log(O/H) = 8.69$ (Stasińska, 2005).
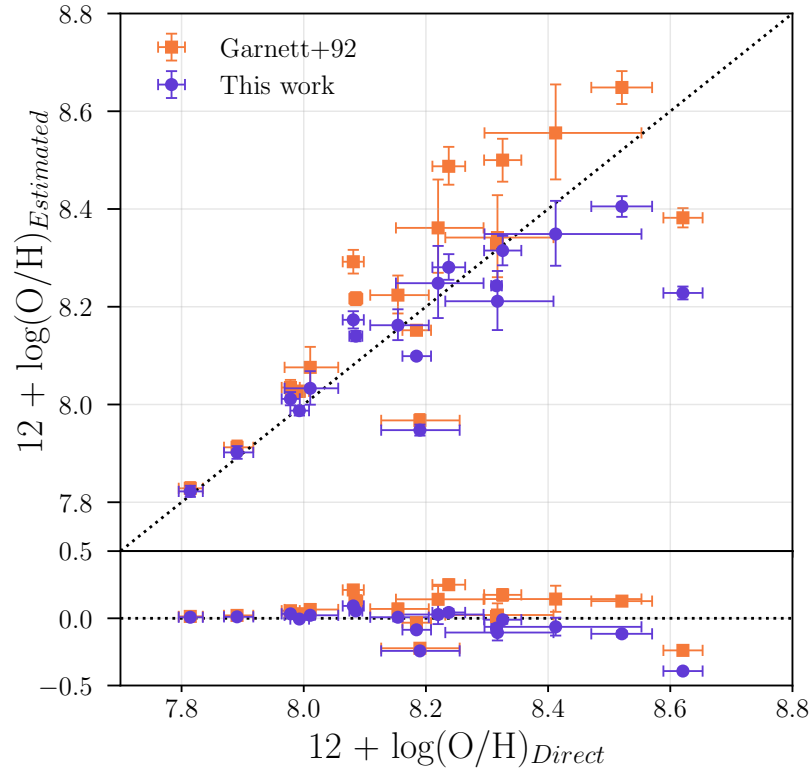
Figure 5.5: Comparison of metallicities calculated using $T_e[O\ II]$ estimated from the temperature relation derived in this work against the relation from Garnett (1992). The estimations are shown as dark-blue and orange circles with 2σ errorbars. The dotted line denotes the 1:1 relation between the estimated and measured abundances. A residual plot is included below taken from the difference between the estimated and the real values of abundances.

Compared to the real values of metallicity measured for our galaxies, ours and the G92 relation have a scatter of $\sigma = 0.11$ and $\sigma = 0.12$ respectively. The scatter gets affected easily by possible outliers in the sample such as the mentioned exceptions of Figure 5.5. If we do not consider those two distant points the scatter drops down to $\sigma = 0.059$ for our relation and to $\sigma = 0.078$ for Garnett (1992), almost 0.02 dex difference. This indicate that our relation is more accurate on predicting metallicities also supported by the mean difference of $\Delta \log(O/H)_{\text{This work}} = 0.078$ against $\Delta \log(O/H)_{\text{G92}} = 0.11$ which deviates from the real

values by 0.032 dex more compared to our relations. Assuming our relation is the closest scenario to the high-z Universe, using the G92 relation on galaxies at high-z would be over-estimating the metallicities by 0.03 dex in the range $7.8 - 8.6$.

Regarding the rest of the temperature relations, we found that there are mild differences with the G92 relations. The good agreement of $T_e[O\,III]$ and $T_e[S\,III]$ and the low scatter of the relation make its use preferable when estimating the $T_e[S\,III]$ temperature from $T_e[O\,III]$. This relation is of particular use when the [S III] lines above 9000Å in rest-frame are not detected. Even having an estimation of $T_e[S\,III]$ by using these relations and the flux of the [S III]$\lambda6312$ line, the sulfur abundance can be estimated which makes this relation a really powerful tool. The $T_e[N\,II]$ temperature, on the other hand, appears to be elusive even for our high-quality data leaving the study of its relation with other temperatures unexplored at high-z. Against expectation from photoionization models that states that $T_e[O\,II] \sim T_e[N\,II]$ due to the similarity of the ionization potentials (Pérez-Montero, 2017), the estimations of $T_e[N\,II]$ are considerably higher than $T_e[O\,II]$ in all cases. Such differences between these quantities can have place due to high density condensations or the presence of planetary nebula (Martins and Viegas, 2002). The contribution to the integrated ionized ISM properties from planetary nebula is negligible if there is any, and we are not able to state whether small scale variations in this case are able to drive such temperatures. The reason behind these values remains thus unknown, but our results constitute possible evidence against the $T_e[O\,II] \sim T_e[N\,II]$ assumption in high-z galaxies.

5.3   Metallicity predictions in High-z galaxies

In this section, we asses the validity of our newly derived calibrations of metallicity vs SELRs from Section 4.3. In this work we probe a total of 12 SELRs that require various sets of different emission lines such as Hα, Hβ, [N II]$\lambda6584$, [O III]$\lambda5007$, [O II]$\lambda\lambda3726,3729$, [Ne III]$\lambda3868$, and [S II]$\lambda\lambda6716,6730$. These sets of SELRs give a valuable insight into the expected relations for galaxies at high-z in the era of JWST which is able to cover a large range of these lines towards $z \sim 4$ and beyond (Sanders et al., 2023). Note that we do not include diagnostic ratios based on [S III]$\lambda9069$ and [S III]$\lambda9532$ since these are in the near-IR range in rest-frame spectra of star-forming galaxies making them to be even more shifted to larger wavelengths in spectra of high-z galaxies. Instead, the use of bluer lines such as [O II] and [Ne III] lines open the possibility of using O2 and Ne3-based calibrations up to extremely high-z.

Previously, Bian et al. (2018) provided calibrations from local analogs valid over the range $7.8 < 12 + \log(O/H) < 8.4$. In this work, we are able to cover metallicities up to $12 + \log(O/H) \sim 8.6$, giving a little glimpse of how the behavior of the calibrations should be at higher metallicities. It has been claimed that a higher metallicities the direct-T_e method underestimate the oxygen abundance, an effect that has been attributed to temperature

stratification in nebulae (Maiolino et al., 2008; Stasińska, 2005). This effect is more important above Solar metallicity ($12 + \log(\mathrm{O/H}) = 8.69$; Asplund et al. 2021) which sets the threshold above the ranges studied in this work. On the other hand, our sample consist on observations of only 18 galaxies which indeed sets a benchmark on the trends observed in this study, but there is still a lot of margin to increase statistical significance. Then, the use of the relations presented here must be taken with caution above Solar metallicity, considering the uncertainties associated to the extrapolation of these results for metal-rich sources where our relations are found to show the largest differences with local HII regions (Denicoló et al., 2002; Pettini and Pagel, 2004; Nagao et al., 2006; Maiolino et al., 2008; Marino et al., 2013; Curti et al., 2020; Sanders et al., 2021) (See Section 4.3.1).

Having said that, one of the first things to emphasize from the results of Section 4.3 is the utility that each relation provides as indicators of metallicity. The lack of correlation in the N2O2 and N2S2 ratios suggest that the quadratic fit for these sources is not entirely reliable, even more in the low and high limits of the metallicity range covered by our galaxies. This is also the case of the R23 ratio, where our galaxies sample exactly the region in metallicity where the ratio changes its growth and little variation is observed. These results turn disposable the use of the R23, N2O2, and N2S2 relations derived in this work. On the other hand, other polynomial relations such as R2, R3, and R3N2 show reasonable correlation with metallicities of our galaxies. However, the best-fit polynomial relation derived in this work also predicts a double-valued behavior inside the range of metallicities covered by our analogs. For instance, values of R3 = 0.8 and R2 = 0.0 have valid solutions in metallicity separated by about 0.4 and $\gtrsim 0.6$ dex. The use of extra ratios such as O3O2 has been proposed to break degeneracies in double-valued relations (Maiolino et al., 2008), so whatever use of the R2, R3 and R3N2 relations of this work should not be considered alone. It is also not clear whether these ratios host a double-valued relation in reality for the studied metallicity range, since it is a matter of debate whether the mean trends traced by the binned data imply linear relations instead. The truth is that we cannot confirm the prevalence of linearity over relations of a higher degree due to the high scatter of our data, opening the possibility of admitting both models. The linear relations studied in this work are the most reliable relations that we can use as indicators of metallicities in high-z galaxies. These include the use of the N2, O3N2, O3O2, Ne3O2, S2, and O3S2 ratios. Marino et al. (2013) found that calibrations involving ratios of lines that are not sensitive to the ionization parameter are found to have more scatter. We confirm this statement by the large scatter inspected both visually and numerically in N2 and S2 based lines. The tightest correlations found in this work correspond to the ratio O3O2 and Ne3O2 placing them in the podium of indicators of metallicities in high-z galaxies.

As expected, our relations show large deviations from calibrations based on $z = 0$ HII regions, but they also surprisingly depart from previous samples of local analogs (Jones et al., 2015; Bian et al., 2018; Pérez-Montero et al., 2021) (See Section 4.3.2). This encouraged us to test the differences that the use of our relation might introduce in constraining the oxygen

abundance. Bian et al. (2018) pointed that calibrations made with the selection criteria of Bian et al. (2016) may not resemble the conditions of mass-selected galaxies. Instead, UV-selected galaxies such as in Steidel et al. (2014) constitute an appropriate scenario to test the calibrations where the excitation mainly comes from the ionization field, which is stronger in these samples. Therefore, we test the differences in metallicity estimations between this work and the SDSS analogs relations from Bian et al. (2018) by using our relations in UV-selected galaxies at $z \sim 2.3$ (Steidel et al., 2014).
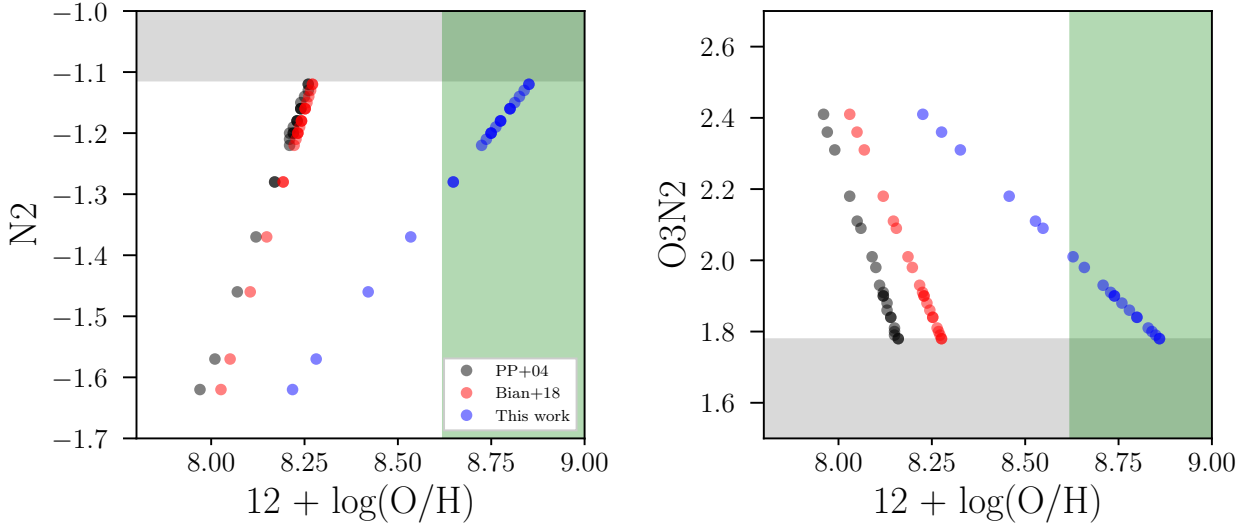
Figure 5.6: Comparison of metallcities of UV-selected galaxies at $z \sim 2.3$ (Steidel et al., 2014) estimated with previous N2 and O3N2 calibrations. Black, red, and blue circles indicate the estimations from SELRs calibration of Pettini and Pagel (2004), Bian et al. (2018) and this work. The shaded gray region denote the cut where our relations are valid in terms of the SELRs and the shaded green region is the range of metallicities where blue points are extrapolations using the relations presented in this work.. These regions are above the maximum value of $12 + \log(O/H) = 8.62$, and the maximum and minimum of N2 and O3N2 measured in this work.

Figure 5.6 shows the predictions of the N2 and O3N2 ratios compared to the re-evaluations of the Pettini and Pagel (2004) made by Steidel et al. (2014). The validity of our relation is restricted by the shaded regions shown in both panels. The gray region cut the values of SELRs that we do not cover in this work (Sets maximum N2 and minimum O3N2 values described below in this same paragraph), hence, no points are shown there. The green indicate the region where our data does not cover metallicities either, but galaxies with ratios above -1.3 observed in Steidel et al. (2014) are predicted to be thanks to extrapolations of the relations derived in this work. The galaxies in this piece of analysis have $12 + \log(O/H) \lesssim 8.6$, $N2 < -1.11$, and $O3N2 > 1.78$.

This ranges highly constrain the sample of galaxies at $z \sim 2.3$ leaving just a few sources of the tail of the values of N2 and O3N2 measured. We observe that the Bian et al. (2018) relations deviate very little with respect to the re-calibrations made by (Steidel et al., 2014). However, our relations predict drastic differences in metallicity. First, only 4 (6) galaxies

lie in the valid range of our N2 (O3N2) relation leaving little room of comparison. The mean difference between our estimations an the Pettini and Pagel (2004) predictions are of $\Delta(12 + \log(O/H)) = 0.32$ for N2 and $\Delta(12 + \log(O/H)) = 0.38$ for O3N2 which are enormous compared to changes of the order of 0.1 dex difference between (Pettini and Pagel, 2004) and Bian et al. (2018). Compared to Bian et al. (2018), our results show in average larger metallicities by $\Delta(12 + \log(O/H)) = 0.28$ for N2 and $\Delta(12 + \log(O/H)) = 0.30$ for O3N2. Our data systematically predicts very large oxygen abundances than previous relations in the context of $z \sim 2$ galaxies. Which ones are the correct calibrations? The answer is we do not know until we robustly determine metallicities of galaxies at $z \sim 2$ with similar ionization conditions and without relying on empirical calibrations. Then we could see which of these relations is closer and advance on unveiling the nature of galaxies at high-z.

We further explored the applicability of our relations to galaxies at higher z. Bian et al. (2018) proposed that if the ISM conditions of star-forming galaxies do not change from $z = 2$ to $z = 5$, their calibrations would hold until such epoch of the Universe. Our sample of analogs resemble the ionizing ISM conditions of galaxies at $z \sim 2$ as it has been shown in Sections 4.1 and 5.1. However, some of the calibrations derived in this work agree well with the predicted relations found from models at $z = 5$ rather than $z = 2$ (See the N2, R2, S2, O3S2 ratios in Figure 4.3.3). Although the rest of the relations do not show a clear agreement with neither of the relations between $z = 0$ to 5, the results call the attention to the validity of metallicity calibrations at higher z. To put this discussion into context, we compare the measurements and the best-fit relations of this work compared to the calibration of Sanders et al. (2023) comprising a sample of galaxies in $z = 2 - 9$ and three individual measurements of Curti et al. (2022), illustrating the power of the James Webb Space Telescope.

Figure 5.7 shows our calibrations of the R2, R3, R23, O3O2, and Ne3O2 ratios in the range $7.8 < 12 + \log(O/H) < 8.6$. We extend our relations down to $12 + \log(O/H) = 7.0$ by simple extrapolation as the dashed line indicates in Figure 5.7. By analyzing the differences, we first note that the relation between the R2 ratio and O/H is described as linear rather than polynomial for galaxies at $z = 2 - 9$ (Sanders et al., 2023), supporting our statement that the R2 ratio can also be described with a linear relation. Our polynomial relation largely deviates from the (Sanders et al., 2023) calibration in the high and low metallicity ends showing a good agreement only in the valid range of our calibration. The binned results, however, follow really well the decreasing N2 ratio forming almost a linear sequence along with measurements from Curti et al. (2022) in the R2 panel of Figure 5.7. The next big discrepancy is witnessed in the R23 ratio, but here little can be done due to the lack of correlation with metallicity aforementioned that leads to poor constraint on the shape of the function. Nevertheless, the value levels of the R23 ratio were not reached by any other relation than the models from Strom et al. (2018) and Papovich et al. (2022), and the very high-z relation of Sanders et al. (2023) which shows a remarkable agreement with our results, followed by a slightly more distant Bian et al. (2018) and Curti et al. (2020) relations from the side of analogs and
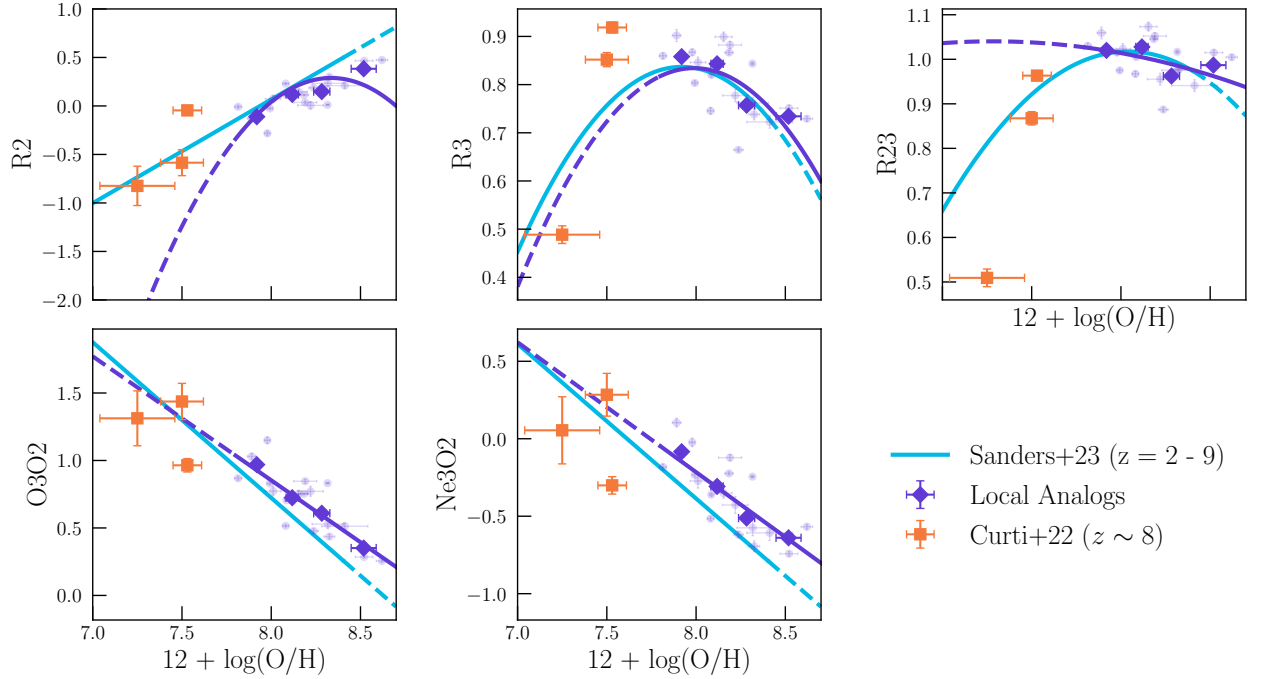
Figure 5.7: Metallicity calibrations for $z > 2$ galaxies (Sanders et al., 2023) for the R2, R3, R23, O3O2, and Ne3O2 ratios. We include individual measurements of our local analogs, binned data, and the best-fit relation with the same format than in Figure 4.4. The best-fit relations of this work and those of Sanders et al. (2023) are shown as solid lines in their corresponding valid metallicity range, while the dashed-line regime shows an extrapolation of the relations. Measurements of metallicity of $z \sim 8$ galaxies are shown as orange squares to probe the metal-poor regime of the relations (Curti et al., 2022).

local HII regions. For metallicities below 7.8, our relations of R2 and R23 fail at reproducing both the high-z calibration and the measurements from Curti et al. (2022). Aside from these ratios, we observe excellent agreement between the extrapolation of our relation with the high-z data at metallicities lower than 7.8 for the R3, O3O2, and Ne3O2 ratios. Between our recommendations on which relations to use to predict metallicities at high-z we kept an eye on the O3O2 and Ne3O2 relations that were really tight and show a clear correlation with metallicity. In the results of Sections 4.3.1, 4.3.2, and 4.3.3, we appreciated significant offsets between our results and literature relations for these two ratios while for a sample of galaxies at very high z (up to 9) our relations are able to predict most of the metallicity levels of metal poor galaxies at $7.0 < 12 + \log(O/H) < 7.8$, showing little offsets that increase at higher metallicities. In this sense, our results could help on constraining the shape of the Sanders et al. (2023) relation at the high metallicity end and it would be more ideal than using local galaxies in that range. It is worth to note that the metallicities derived in Curti et al. (2022) and Sanders et al. (2023) were estimated using temperature relations to derive the temperature of the low ionization zone $T_e[O~II]$ from the measured value of $T_e[O~III]$ that was indeed measured. From one side, this arises again the question of the validity of this relation at high-z galaxies, being our study one of the closer looks into this relation for

the distant Universe through our analogs. On the other hand remains the issue: Would these results change at $z > 2$ if the T_e[O II] was measured directly allowing robust estimations of $12 + \log(\mathrm{O/H})$? This is, again, something that will not be confirmed until we are able to measure metallicities such as it was done in this study with a full budget of the required emission lines in the spectra in galaxies in the early Universe. Even more it highlights the importance of exploring the temperature relations in the early Universe as we have done in this work. By now, we can only confirm that our analogs are consistent with the predicted values of metallicities at $z \geq 2$ by the R3, O3O2, and Ne3O2 ratios and along with our temperature relations they can be used to extract measurements of as a base of comparison for upcoming metallicity studies at high-z.

Chapter 6

Conclusions

We studied the relations between strong-emission line ratios and the oxygen abundance for a sample of 18 local analogs of star-forming galaxies at $z \sim 2$ selected by their position in the BPT diagram. We provide new calibrations of temperature relations and metallicity vs SELRs that consitute one of the most complete and closest insights into the picture of ionization and abundances studies in high-z galaxies. The conclusions of this work are listed as follows:

- BPT diagnosis and nebular properties of the gas in our sample of analogs suggest that star-formation is the main mechanism of excitation of the gas which is under extreme ionization supported by the high values of ionization parameters compared to galaxies in the local Universe (Bian et al., 2016). We further confirmed that the contribution of electron density and N/O ratio as drivers of the shifts on the BPT is minor and the ionization parameter is the main responsible of this effect. Our galaxies also comprise a sample of low-mass highly-active star-forming galaxies inferred from the SED modeling which showed systematically higher SFR and sSFR for the predicted median stellar mass of $10^{8.07}$ M$_\odot$. The N/O abundances and the ages predicted by the SED suggest that our galaxies are young systems on still undergoing primary stages of gas enrichment. The joint results of the global properties of the sample of galaxies along with the diagnostics of the nebular conditions justify the use of our sample to probe the abundances of the early Universe as one of the closest laboratories of galaxies at $z \sim 2$.

- We derived three new temperature relations between the high, intermediate, and low-ionization zones of the ISM for the first time for galaxies at high-z. The T$_e$[O II] vs T$_e$[O III] show a flatter slope of 0.46 compared to the 0.7 of one of the most widely used temperature relations to estimate metallicities at high-z (Garnett, 1992), leading to differences around 0.2 dex in the metal-rich regime. Our relation also gives better predictions with 0.01 dex lower scatter (0.02 dex excluding possible outliers) compared to the (Garnett, 1992) relation. Our T$_e$[S III] vs T$_e$[O III] relation agree very well with photoionization models (Garnett, 1992) and the use of these relations is preferable at

high-z over the derived from local HII regions (Rogers et al., 2021; Berg et al., 2020a). We found that changes in the temperature relation between T_e[O II] and T_e[O III] are independent of electron density in galaxies at high-z.

- We provide one of the most complete sets of calibrations of metallicity with 12 SELRs among which is N2, R2, R3, R23, O3N2, R3N2, N2O2, O3O2, Ne3O2, S2, O3S2, and N2S2, valid in the metallicity range $7.8 < 12 + \log(\text{O/H}) < 8.6$. We confirm that N2 based indicators show large scatter, i.e. N2 and O3N2, and some of them have negligible correlation with metallicity making their use disposable such as the case of N2O2 and N2S2. Polynomial relations derived in this work might be used with caution of the caveats they have and are not recommended to be used without the support of some linear relations. We found significant offsets with respect to local galaxies, analogs of high-z galaxies, and photoionization models in most of the ratios, leading to possible underestimation of metallicities up to 0.3 dex difference in the case of the N2 and O3N2 calibrations. We found good correlations in the ratios O3O2, Ne3O2, S2, O3S2, and R3N2, for which we recommend their use as metallicity estimators.

- Our relations remarkably agree with the abundances indicators at galaxies up to $z = 9$ (Derived with the aid of temperature relations based on models) by extrapolating the range of metallicities down to $12 + \log(\text{O/H}) = 7.0$. This open a window of applicability to earlier epochs of the Universe than those that the analogs were initially thought of and provide a benchmark in unveiling the abundance trends in the early Universe in the JWST era.

Our spectra is sensitive and rich enough to detect lines of more α elements in the gas. Further science can be done with our fully constrained electron density and temperatures. In particular, these analogs can be used to study the elemental abundances of Sulfur, Neon, Argon, and Iron, giving new insights into how the gas enrichment in galaxies at $z \sim 2$ and beyond.

References

Abazajian, K. N., Adelman-McCarthy, J. K., Agüeros, M. A., Allam, S. S., Allende Prieto, C., An, D., Anderson, K. S. J., Anderson, S. F., Annis, J., Bahcall, N. A., Bailer-Jones, C. A. L., Barentine, J. C., Bassett, B. A., Becker, A. C., Beers, T. C., and more authors., M. (2009). The Seventh Data Release of the Sloan Digital Sky Survey. *Astrophysical Journal Supplements*, 182(2):543–558.

Aller, L. H., Ufford, C. W., and van Vleck, J. H. (1949). Multiplet Intensities for the Nebular Lines $\hat{4}$S - $_{2}$D of o II. *The Astrophysical Journal*, 109:42.

Andrews, B. H. and Martini, P. (2013). The Mass-Metallicity Relation with the Direct Method on Stacked Spectra of SDSS Galaxies. *The Astrophysical Journal*, 765(2):140.

Arellano-Córdova, K. Z., Berg, D. A., Chisholm, J., Arrabal Haro, P., Dickinson, M., Finkelstein, S. L., Leclercq, F., Rogers, N. S. J., Simons, R. C., Skillman, E. D., Trump, J. R., and Kartaltepe, J. S. (2022). A First Look at the Abundance Pattern-O/H, C/O, and Ne/O-in z ¿ 7 Galaxies with JWST/NIRSpec. *The Astrophysical Journal Letters*, 940(1):L23.

Asplund, M., Amarsi, A. M., and Grevesse, N. (2021). The chemical make-up of the Sun: A 2020 vision. *Astronomy & Astrophysics*, 653:A141.

Baldwin, J. A., Phillips, M. M., and Terlevich, R. (1981). Classification parameters for the emission-line spectra of extragalactic objects. *Publications of the Astronomical Society of the Pacific*, 93:5–19.

Balmer, J. J. (1885). Notiz über die Spectrallinien des Wasserstoffs. *Annalen der Physik*, 261(5):80–87.

Berg, D. A., Chisholm, J., Erb, D. K., Skillman, E. D., Pogge, R. W., and Olivier, G. M. (2021). Characterizing extreme emission-line galaxies. i. a four-zone ionization model for very high-ionization emission*. *The Astrophysical Journal*, 922(2):170.

Berg, D. A., Pogge, R. W., Skillman, E. D., Croxall, K. V., Moustakas, J., and Mayker, N. (2020a). The CHAOS Survey. In *IAU General Assembly*, pages 246–248.

Berg, D. A., Pogge, R. W., Skillman, E. D., Croxall, K. V., Moustakas, J., Rogers, N. S. J., and Sun, J. (2020b). CHAOS IV: Gas-phase Abundance Trends from the First Four CHAOS Galaxies. *The Astrophysical Journal*, 893(2):96.

Bian, F., Kewley, L. J., and Dopita, M. A. (2018). "Direct" Gas-phase Metallicity in Local Analogs of High-redshift Galaxies: Empirical Metallicity Calibrations for High-redshift Star-forming Galaxies. *The Astrophysical Journal*, 859(2):175.

Bian, F., Kewley, L. J., Dopita, M. A., and Blanc, G. A. (2017). Mass-Metallicity Relation for Local Analogs of High-redshift galaxies: Implications for the Evolution of the Mass-Metallicity Relations. *The Astrophysical Journal*, 834(1):51.

Bian, F., Kewley, L. J., Dopita, M. A., and Juneau, S. (2016). Local Analogs for High-redshift Galaxies: Resembling the Physical Conditions of the Interstellar Medium in High-redshift Galaxies. *The Astrophysical Journal*, 822(2):62.

Bian, F., Kewley, L. J., Groves, B., and Dopita, M. A. (2020). What drives the redshift evolution of strong emission line ratios? *Monthly Notices of the Royal Astronomical Society*, 493(1):580–585.

Blanton, M. R. and Moustakas, J. (2009). Physical Properties and Environments of Nearby Galaxies. *Annual Reviews of Astronomy & Astrophysics*, 47(1):159–210.

Boquien, M., Burgarella, D., Roehlly, Y., Buat, V., Ciesla, L., Corre, D., Inoue, A. K., and Salas, H. (2019). CIGALE: a python Code Investigating GALaxy Emission. *Astronomy & Astrophysics*, 622:A103.

Bouwens, R. J., Illingworth, G. D., Franx, M., Chary, R. R., Meurer, G. R., Conselice, C. J., Ford, H., Giavalisco, M., and van Dokkum, P. (2009). UV Continuum Slope and Dust Obscuration from z ~6 to z ~2: The Star Formation Rate Density at High Redshift. *The Astrophysical Journal*, 705(1):936–961.

Bovino, S., Grassi, T., Schleicher, D. R. G., and Banerjee, R. (2016). The Formation of the Primitive Star SDSS J102915+172927: Effect of the Dust Mass and the Grain-size Distribution. *The Astrophysical Journal*, 832(2):154.

Bovino, S., Grassi, T., Schleicher, D. R. G., and Latif, M. A. (2014). Formation of Carbon-enhanced Metal-poor Stars in the Presence of Far-ultraviolet Radiation. *The Astrophysical Journal Letters*, 790(2):L35.

Brinchmann, J., Charlot, S., White, S. D. M., Tremonti, C., Kauffmann, G., Heckman, T., and Brinkmann, J. (2004). The physical properties of star-forming galaxies in the low-redshift Universe. *Monthly Notices of the Royal Astronomical Society*, 351(4):1151–1179.

Bruzual, G. and Charlot, S. (2003). Stellar population synthesis at the resolution of 2003. *Monthly Notices of the Royal Astronomical Society*, 344(4):1000–1028.

Calzetti, D., Armus, L., Bohlin, R. C., Kinney, A. L., Koornneef, J., and Storchi-Bergmann, T. (2000). The Dust Content and Opacity of Actively Star-forming Galaxies. *The Astrophysical Journal*, 533(2):682–695.

Campbell, A., Terlevich, R., and Melnick, J. (1986). The stellar populations and evolution of H II galaxies - I. High signal-to-noise optical spectroscopy. *Monthly Notices of the Royal Astronomical Society*, 223:811–825.

Cardamone, C., Schawinski, K., Sarzi, M., Bamford, S. P., Bennert, N., Urry, C. M., Lintott, C., Keel, W. C., Parejko, J., Nichol, R. C., Thomas, D., Andreescu, D., Murray, P., Raddick, M. J., Slosar, A., Szalay, A., and Vandenberg, J. (2009). Galaxy Zoo Green Peas: discovery of a class of compact extremely star-forming galaxies. *Monthly Notices of the Royal Astronomical Society*, 399(3):1191–1205.

Cardelli, J. A., Clayton, G. C., and Mathis, J. S. (1989). The Relationship between Infrared, Optical, and Ultraviolet Extinction. *The Astrophysical Journal*, 345:245.

Carroll, B. W. and Ostlie, D. A. (1996). *An Introduction to Modern Astrophysics*. Cambridge University Press.

Chabrier, G. (2003). Galactic Stellar and Substellar Initial Mass Function. *Publications of the Astronomical Society of the Pacific*, 115(809):763–795.

Chiappini, C., Romano, D., and Matteucci, F. (2003). Oxygen, carbon and nitrogen evolution in galaxies. *Monthly Notices of the Royal Astronomical Society*, 339(1):63–81.

Chisholm, J., Tremonti, C. A., Leitherer, C., Chen, Y., Wofford, A., and Lundgren, B. (2015). Scaling Relations Between Warm Galactic Outflows and Their Host Galaxies. *The Astrophysical Journal*, 811(2):149.

Christensen, L., Laursen, P., Richard, J., Hjorth, J., Milvang-Jensen, B., Dessauges-Zavadsky, M., Limousin, M., Grillo, C., and Ebeling, H. (2012). Gravitationally lensed galaxies at 2 ¡ z ¡ 3.5: direct abundance measurements of lyalpha emitters. *Monthly Notices of the Royal Astronomical Society*, 427(3):1973–1982.

Curti, M., D'Eugenio, F., Carniani, S., Maiolino, R., Sandles, L., Witstok, J., Baker, W. M., Bennett, J. S., Piotrowska, J. M., Tacchella, S., Charlot, S., Nakajima, K., Maheson, G., Mannucci, F., Arribas, S., Belfiore, F., Bonaventura, N. R., Bunker, A. J., Chevallard, J., Cresci, G., Curtis-Lake, E., Hayden-Pawson, C., Kumari, N., Laseter, I., Looser, T. J., Marconi, A., Maseda, M. V., Jones, G. C., Scholtz, J., Smit, R., Ubler, H., and Wallace, I. E. B. (2022). The chemical enrichment in the early Universe as probed by JWST via direct metallicity measurements at z~8. arXiv:2207.12375 [astro-ph].

Curti, M., Maiolino, R., Curtis-Lake, E., Chevallard, J., Carniani, S., D'Eugenio, F., Looser, T. J., Scholtz, J., Charlot, S., Cameron, A., Übler, H., Witstok, J., Boyett, K., Laseter, I., Sandles, L., Arribas, S., Bunker, A., Giardino, G., Maseda, M. V., Rawle, T., Rodríguez Del Pino, B., Smit, R., Willott, C. J., Eisenstein, D. J., Hausen, R., Johnson, B., Rieke, M., Robertson, B., Tacchella, S., Williams, C. C., Willmer, C., Baker, W. M., Bhatawdekar, R., Egami, E., Helton, J. M., Ji, Z., Kumari, N., Perna, M., Shivaei, I., and Sun, F. (2024). JADES: Insights into the low-mass end of the mass-metallicity-SFR relation at 3 ¡ z ¡ 10 from deep JWST/NIRSpec spectroscopy. *Astronomy & Astrophysics*, 684:A75.

Curti, M., Mannucci, F., Cresci, G., and Maiolino, R. (2020). The mass-metallicity and the fundamental metallicity relation revisited on a fully T_e-based abundance scale for galaxies. *Monthly Notices of the Royal Astronomical Society*, 491(1):944–964.

Denicoló, G., Terlevich, R., and Terlevich, E. (2002). New light on the search for low-metallicity galaxies - I. The N2 calibrator. *Monthly Notices of the Royal Astronomical Society*, 330(1):69–74.

Dopita, M. A., Kewley, L. J., Sutherland, R. S., and Nicholls, D. C. (2016). Chemical abundances in high-redshift galaxies: a powerful new emission line diagnostic. *Astrophysics & Space Science*, 361:61.

Downing, E. R. and Oman, K. A. (2023). The many reasons that the rotation curves of low-mass galaxies can fail as tracers of their matter distributions. *Monthly Notices of the Royal Astronomical Society*, 522(3):3318–3336.

Draine, B. T. (2009). Interstellar Dust Models and Evolutionary Implications. In Henning, T., Grün, E., and Steinacker, J., editors, *Cosmic Dust - Near and Far*, volume 414 of *Astronomical Society of the Pacific Conference Series*, page 453.

Edmunds, M. G. (1990). General Constraints on the Effect of Gas Flows in the Chemical Evolution of Galaxies. *Monthly Notices of the Royal Astronomical Society*, 246:678.

Ellison, S. L., Patton, D. R., Simard, L., and McConnachie, A. W. (2008). Clues to the Origin of the Mass-Metallicity Relation: Dependence on Star Formation Rate and Galaxy Size. *The Astrophysical Journal Letters*, 672(2):L107.

Erb, D. K., Pettini, M., Shapley, A. E., Steidel, C. C., Law, D. R., and Reddy, N. A. (2010). Physical Conditions in a Young, Unreddened, Low-metallicity Galaxy at High Redshift. *The Astrophysical Journal*, 719(2):1168–1190.

Erb, D. K., Shapley, A. E., Pettini, M., Steidel, C. C., Reddy, N. A., and Adelberger, K. L. (2006). The Mass-Metallicity Relation at z¿˜2. *The Astrophysical Journal*, 644(2):813–828.

Finlator, K. and Davé, R. (2008). The origin of the galaxy mass-metallicity relation and implications for galactic outflows. *Monthly Notices of the Royal Astronomical Society*, 385(4):2181–2204.

Foreman-Mackey, D., Hogg, D. W., Lang, D., and Goodman, J. (2013). emcee: The MCMC Hammer. *Publications of the Astronomical Society of the Pacific*, 125(925):306.

Fukugita, M., Ichikawa, T., Gunn, J. E., Doi, M., Shimasaku, K., and Schneider, D. P. (1996). The Sloan Digital Sky Survey Photometric System. *The Astronomical Journal*, 111:1748.

Garg, P., Narayanan, D., Byler, N., Sanders, R. L., Shapley, A. E., Strom, A. L., Davé, R., Hirschmann, M., Lovell, C. C., Otter, J., Popping, G., and Privon, G. C. (2022). The BPT Diagram in Cosmological Galaxy Formation Simulations: Understanding the Physics Driving Offsets at High Redshift. *The Astrophysical Journal*, 926(1):80.

Garg, P., Narayanan, D., Sanders, R. L., Davè, R., Popping, G., Shapley, A. E., Stark, D. P., and Trump, J. R. (2023). Theoretical strong line metallicity diagnostics for the JWST era. *arXiv e-prints*, page arXiv:2310.08622.

Garnett, D. R. (1992). Electron Temperature Variations and the Measurement of Nebular Abundances. *The Astronomical Journal*, 103:1330.

Hägele, G. F., Pérez-Montero, E., Díaz, Á. I., Terlevich, E., and Terlevich, R. (2006). The temperature and ionization structure of the emitting gas in HII galaxies: implications for the accuracy of abundance determinations. *Monthly Notices of the Royal Astronomical Society*, 372(1):293–312.

Henry, R. B. C., Edmunds, M. G., and Köppen, J. (2000). On the Cosmic Origins of Carbon and Nitrogen. *The Astrophysical Journal*, 541(2):660–674.

Höfner, S. and Olofsson, H. (2018). Mass loss of stars on the asymptotic giant branch. Mechanisms, models and measurements. *Astronomy & Astrophysics Reviews*, 26(1):1.

Hogarth, L., Amorín, R., Vílchez, J. M., Hägele, G. F., Cardaci, M., Pérez-Montero, E., Firpo, V., Jaskot, A., and Chávez, R. (2020). Chemodynamics of green pea galaxies - I. Outflows and turbulence driving the escape of ionizing photons and chemical enrichment. *Monthly Notices of the Royal Astronomical Society*, 494(3):3541–3561.

Hoyle, F. (1946). The synthesis of the elements from hydrogen. *Monthly Notices of the Royal Astronomical Society*, 106:343.

Izotov, Y. I., Stasińska, G., Meynet, G., Guseva, N. G., and Thuan, T. X. (2006). The chemical composition of metal-poor emission-line galaxies in the Data Release 3 of the Sloan Digital Sky Survey. *Astronomy & Astrophysics*, 448(3):955–970.

James, B. L., Pettini, M., Christensen, L., Auger, M. W., Becker, G. D., King, L. J., Quider, A. M., Shapley, A. E., and Steidel, C. C. (2014). Testing metallicity indicators at z ∼ 1.4 with the gravitationally lensed galaxy CASSOWARY20. *Monthly Notices of the Royal Astronomical Society*, 440(2):1794–1809.

Jones, T., Martin, C., and Cooper, M. C. (2015). Temperature-based Metallicity Measurements at z=0.8: Direct Calibration of Strong-line Diagnostics at Intermediate Redshift. *The Astrophysical Journal*, 813(2):126.

Kauffmann, G., Heckman, T. M., Tremonti, C., Brinchmann, J., Charlot, S., White, S. D. M., Ridgway, S. E., Brinkmann, J., Fukugita, M., Hall, P. B., Ivezić, Ž., Richards, G. T., and Schneider, D. P. (2003). The host galaxies of active galactic nuclei. *Monthly Notices of the Royal Astronomical Society*, 346(4):1055–1077.

Kawata, D. and Rauch, M. (2007). Galactic Wind Signatures around High-Redshift Galaxies. *The Astrophysical Journal*, 663(1):38–52.

Kelly, B. C. (2007). Some Aspects of Measurement Error in Linear Regression of Astronomical Data. *The Astrophysical Journal*, 665(2):1489–1506.

Kewley, L. J., Dopita, M. A., Leitherer, C., Davé, R., Yuan, T., Allen, M., Groves, B., and Sutherland, R. (2013a). Theoretical Evolution of Optical Strong Lines across Cosmic Time. *The Astrophysical Journal*, 774(2):100.

Kewley, L. J., Dopita, M. A., Sutherland, R. S., Heisler, C. A., and Trevena, J. (2001). Theoretical Modeling of Starburst Galaxies. *The Astrophysical Journal*, 556(1):121–140.

Kewley, L. J. and Ellison, S. L. (2008). Metallicity Calibrations and the Mass-Metallicity Relation for Star-forming Galaxies. *The Astrophysical Journal*, 681(2):1183–1204.

Kewley, L. J., Groves, B., Kauffmann, G., and Heckman, T. (2006). The host galaxies and classification of active galactic nuclei. *Monthly Notices of the Royal Astronomical Society*, 372(3):961–976.

Kewley, L. J., Maier, C., Yabe, K., Ohta, K., Akiyama, M., Dopita, M. A., and Yuan, T. (2013b). The Cosmic BPT Diagram: Confronting Theory with Observations. *The Astrophysical Journal Letters*, 774(1):L10.

Kewley, L. J., Nicholls, D. C., and Sutherland, R. S. (2019). Understanding Galaxy Evolution Through Emission Lines. *Annual Reviews of Astronomy & Astrophysics*, 57:511–570.

Kramida, A., Yu. Ralchenko, Reader, J., and and NIST ASD Team (2023). NIST Atomic Spectra Database (ver. 5.11), [Online]. Available: `https://physics.nist.gov/asd` [2024, May 7]. National Institute of Standards and Technology, Gaithersburg, MD.

Kriek, M., Shapley, A. E., Reddy, N. A., Siana, B., Coil, A. L., Mobasher, B., Freeman, W. R., de Groot, L., Price, S. H., Sanders, R., Shivaei, I., Brammer, G. B., Momcheva, I. G., Skelton, R. E., van Dokkum, P. G., Whitaker, K. E., Aird, J., Azadi, M., Kassis, M., Bullock, J. S., Conroy, C., Davé, R., Kereš, D., and Krumholz, M. (2015). The MOSFIRE Deep Evolution Field (MOSDEF) Survey: Rest-frame Optical Spectroscopy for ~1500 H-selected Galaxies at 1.37 ¡ z ¡ 3.8. *Astrophysical Journal Supplements*, 218(2):15.

Lequeux, J., Peimbert, M., Rayo, J. F., Serrano, A., and Torres-Peimbert, S. (1979). Chemical Composition and Evolution of Irregular and Blue Compact Galaxies. *Astronomy & Astrophysics*, 80:155.

Llerena, M., Amorín, R., Pentericci, L., Calabrò, A., Shapley, A. E., Boutsia, K., Pérez-Montero, E., Vílchez, J. M., and Nakajima, K. (2023). Ionized gas kinematics and chemical abundances of low-mass star-forming galaxies at z ∼ 3. *Astronomy & Astrophysics*, 676:A53.

Lupton, R. H., Gunn, J. E., and Szalay, A. S. (1999). A Modified Magnitude System that Produces Well-Behaved Magnitudes, Colors, and Errors Even for Low Signal-to-Noise Ratio Measurements. *The Astronomical Journal*, 118(3):1406–1410.

Luridiana, V., Morisset, C., and Shaw, R. A. (2015). PyNeb: a new tool for analyzing emission lines. I. Code description and validation of results. *Astronomy & Astrophysics*, 573:A42.

Madau, P. and Dickinson, M. (2014). Cosmic Star-Formation History. *Annual Reviews of Astronomy & Astrophysics*, 52:415–486.

Maiolino, R., Nagao, T., Grazian, A., Cocchia, F., Marconi, A., Mannucci, F., Cimatti, A., Pipino, A., Ballero, S., Calura, F., Chiappini, C., Fontana, A., Granato, G. L., Matteucci, F., Pastorini, G., Pentericci, L., Risaliti, G., Salvati, M., and Silva, L. (2008). AMAZE. I. The evolution of the mass-metallicity relation at z ¿ 3. *Astronomy & Astrophysics*, 488(2):463–479.

Marino, R. A., Rosales-Ortega, F. F., Sánchez, S. F., Gil de Paz, A., Vílchez, J., Miralles-Caballero, D., Kehrig, C., Pérez-Montero, E., Stanishev, V., Iglesias-Páramo, J., Díaz, A. I., Castillo-Morales, A., Kennicutt, R., López-Sánchez, A. R., Galbany, L., García-Benito, R., Mast, D., Mendez-Abreu, J., Monreal-Ibero, A., Husemann, B., Walcher, C. J., García-Lorenzo, B., Masegosa, J., Del Olmo Orozco, A., Mourão, A. M., Ziegler, B., Mollá, M., Papaderos, P., Sánchez-Blázquez, P., González Delgado, R. M., Falcón-Barroso, J., Roth, M. M., van de Ven, G., and CALIFA Team (2013). The O3N2 and N2 abundance indicators revisited: improved calibrations based on CALIFA and T_e-based literature data. *Astronomy & Astrophysics*, 559:A114.

Martins, L. P. and Viegas, S. M. (2002). Gas temperature and excitation classes in planetary nebulae. *Astronomy & Astrophysics*, 387:1074–1082.

Matsuura, M., Dwek, E., Barlow, M. J., Babler, B., Baes, M., Meixner, M., Cernicharo, J., Clayton, G. C., Dunne, L., Fransson, C., Fritz, J., Gear, W., Gomez, H. L., Groenewegen, M. A. T., Indebetouw, R., Ivison, R. J., Jerkstrand, A., Lebouteiller, V., Lim, T. L., Lundqvist, P., Pearson, C. P., Roman-Duval, J., Royer, P., Staveley-Smith, L., Swinyard, B. M., van Hoof, P. A. M., van Loon, J. T., Verstappen, J., Wesson, R., Zanardo, G., Blommaert, J. A. D. L., Decin, L., Reach, W. T., Sonneborn, G., Van de Steene, G. C., and Yates, J. A. (2015). A Stubbornly Large Mass of Cold Dust in the Ejecta of Supernova 1987A. *The Astrophysical Journal*, 800(1):50.

Medling, A. M., U, V., Rich, J. A., Kewley, L. J., Armus, L., Dopita, M. A., Max, C. E., Sanders, D., and Sutherland, R. (2015). Shocked gas in IRAS F17207-0014: ISM collisions and outflows. *Monthly Notices of the Royal Astronomical Society*, 448(3):2301–2311.

Méndez-Delgado, J. E. and García-Rojas, J. (2023). The abundance discrepancy in ionized nebulae: which are the correct abundances? *arXiv e-prints*, page arXiv:2311.10280.

Menzel, D. H., Aller, L. H., and Hebb, M. H. (1941). Physical Processes in Gaseous Nebulae. XIII. *The Astrophysical Journal*, 93:230.

Mesa-Delgado, A. and Esteban, C. (2010). Small-spatial-scale variations of nebular properties and the abundance discrepancy in three Galactic HII regions. *Monthly Notices of the Royal Astronomical Society*, 405(4):2651–2667.

Meurer, G. R., Heckman, T. M., and Calzetti, D. (1999). Dust Absorption and the Ultraviolet Luminosity Density at z ~3 as Calibrated by Local Starburst Galaxies. *The Astrophysical Journal*, 521(1):64–80.

Nagao, T., Maiolino, R., and Marconi, A. (2006). Gas metallicity diagnostics in star-forming galaxies. *Astronomy & Astrophysics*, 459(1):85–101.

Nakajima, K. and Ouchi, M. (2014). Ionization state of inter-stellar medium in galaxies: evolution, SFR-M_*-Z dependence, and ionizing photon escape. *Monthly Notices of the Royal Astronomical Society*, 442(1):900–916.

Newville, M., Stensitzki, T., Allen, D. B., and Ingargiola, A. (2015). LMFIT: Non-Linear Least-Square Minimization and Curve-Fitting for Python.

Nicholls, D. C., Kewley, L. J., and Sutherland, R. S. (2020). Estimating Electron Temperatures in Ionized Nebulae: The Direct Method and its Limitations. *Publications of the Astronomical Society of the Pacific*, 132(1009):033001.

Olive, K. A. and Skillman, E. D. (2004). A Realistic Determination of the Error on the Primordial Helium Abundance: Steps toward Nonparametric Nebular Helium Abundances. *The Astrophysical Journal*, 617(1):29–49.

Osterbrock, D. E. and Ferland, G. J. (2006). *Astrophysics of gaseous nebulae and active galactic nuclei*. University Science Books.

Papovich, C., Simons, R. C., Estrada-Carpenter, V., Matharu, J., Momcheva, I., Trump, J. R., Backhaus, B. E., Brammer, G., Cleri, N. J., Finkelstein, S. L., Giavalisco, M., Ji, Z., Jung, I., Kewley, L. J., Nicholls, D. C., Pirzkal, N., Rafelski, M., and Weiner, B. (2022). CLEAR: The Ionization and Chemical-enrichment Properties of Galaxies at 1.1 ¡ z ¡ 2.3. *The Astrophysical Journal*, 937(1):22.

Peimbert, M. (1967). Temperature Determinations of H II Regions. *The Astrophysical Journal*, 150:825.

Pérez-Montero, E. (2017). Ionized Gaseous Nebulae Abundance Determination from the Direct Method. *Publications of the Astronomical Society of the Pacific*, 129(974):043001.

Pérez-Montero, E., Amorín, R., Sánchez Almeida, J., Vílchez, J. M., García-Benito, R., and Kehrig, C. (2021). Extreme emission-line galaxies in SDSS - I. Empirical and model-based calibrations of chemical abundances. *Monthly Notices of the Royal Astronomical Society*, 504(1):1237–1252.

Pettini, M. and Pagel, B. E. J. (2004). [OIII]/[NII] as an abundance indicator at high redshift. *Monthly Notices of the Royal Astronomical Society*, 348(3):L59–L63.

Prochaska, J. X., Hennawi, J., Cooke, R., Westfall, K., Wang, F., EmAstro, Tiffanyhsyu, Wasserman, A., Villaume, A., Marijana777, Schindler, J., Young, D., Simha, S., Wilde, M., Tejos, N., Isbell, J., Flörs, A., Sandford, N., Vasović, Z., Betts, E., and Holden, B. (2020a). pypeit/PypeIt: Release 1.0.0.

Prochaska, J. X., Hennawi, J. F., Westfall, K. B., Cooke, R. J., Wang, F., Hsyu, T., Davies, F. B., and Farina, E. P. (2020b). PypeIt: The Python Spectroscopic Data Reduction Pipeline. *arXiv e-prints*, page arXiv:2005.06505.

Rodighiero, G., Daddi, E., Baronchelli, I., Cimatti, A., Renzini, A., Aussel, H., Popesso, P., Lutz, D., Andreani, P., Berta, S., Cava, A., Elbaz, D., Feltre, A., Fontana, A., Förster Schreiber, N. M., Franceschini, A., Genzel, R., Grazian, A., Gruppioni, C., Ilbert, O., Le Floch, E., Magdis, G., Magliocchetti, M., Magnelli, B., Maiolino, R., McCracken, H., Nordon, R., Poglitsch, A., Santini, P., Pozzi, F., Riguccini, L., Tacconi, L. J., Wuyts, S., and Zamorani, G. (2011). The Lesser Role of Starbursts in Star Formation at z = 2. *The Astrophysical Journal Letters*, 739(2):L40.

Rogers, N. S. J., Skillman, E. D., Pogge, R. W., Berg, D. A., Moustakas, J., Croxall, K. V., and Sun, J. (2021). CHAOS. VI. Direct Abundances in NGC 2403. *The Astrophysical Journal*, 915(1):21.

Sanders, R. L., Shapley, A. E., Clarke, L., Topping, M. W., Reddy, N. A., Kriek, M., Jones, T., Stark, D. P., and Tang, M. (2023). A Preview of JWST Metallicity Studies at Cosmic Noon: The First Detection of Auroral [O II] Emission at High Redshift. *The Astrophysical Journal*, 943(2):75.

Sanders, R. L., Shapley, A. E., Jones, T., Reddy, N. A., Kriek, M., Siana, B., Coil, A. L., Mobasher, B., Shivaei, I., Davé, R., Azadi, M., Price, S. H., Leung, G., Freeman, W. R., Fetherolf, T., de Groot, L., Zick, T., and Barro, G. (2021). The MOSDEF Survey: The Evolution of the Mass-Metallicity Relation from z = 0 to z 3.3. *The Astrophysical Journal*, 914(1):19.

Sanders, R. L., Shapley, A. E., Kriek, M., Reddy, N. A., Freeman, W. R., Coil, A. L., Siana, B., Mobasher, B., Shivaei, I., Price, S. H., and de Groot, L. (2016). The MOSDEF Survey: Detection of [OIII]λ4363 and the direct-method oxygen abundance of a star-forming galaxy at z=3.08. *The Astrophysical Journal*, 825(2):L23. arXiv: 1606.04107.

Sanders, R. L., Shapley, A. E., Kriek, M., Reddy, N. A., Freeman, W. R., Coil, A. L., Siana, B., Mobasher, B., Shivaei, I., Price, S. H., and de Groot, L. (2016). The MOSDEF Survey: Electron Density and Ionization Parameter at z ~2.3. *The Astrophysical Journal*, 816(1):23.

Sanders, R. L., Shapley, A. E., Reddy, N. A., Kriek, M., Siana, B., Coil, A. L., Mobasher, B., Shivaei, I., Freeman, W. R., Azadi, M., Price, S. H., Leung, G., Fetherolf, T., de Groot, L., Zick, T., Fornasini, F. M., and Barro, G. (2020). The MOSDEF survey: direct-method metallicities and ISM conditions at z $\sim$ 1.5-3.5. *Monthly Notices of the Royal Astronomical Society*, 491(1):1427–1455.

Sanders, R. L., Shapley, A. E., Topping, M. W., Reddy, N. A., and Brammer, G. B. (2023). Direct T_e-based Metallicities of z=2-9 Galaxies with JWST/NIRSpec: Empirical Metallicity Calibrations Applicable from Reionization to Cosmic Noon. ADS Bibcode: 2023arXiv230308149S.

Scarlata, C., Hayes, M., Panagia, N., Mehta, V., Haardt, F., and Bagley, M. (2024). On the universal validity of Case B recombination theory. *arXiv e-prints*, page arXiv:2404.09015.

Schaerer, D., Marques-Chaves, R., Barrufet, L., Oesch, P., Izotov, Y. I., Naidu, R., Guseva, N. G., and Brammer, G. (2022). First look with JWST spectroscopy: Resemblance among z $\sim$ 8 galaxies and local analogs. *Astronomy & Astrophysics*, 665:L4.

Schlafly, E. F. and Finkbeiner, D. P. (2011). Measuring Reddening with Sloan Digital Sky Survey Stellar Spectra and Recalibrating SFD. *The Astrophysical Journal*, 737(2):103.

Schreiber, C., Pannella, M., Elbaz, D., Béthermin, M., Inami, H., Dickinson, M., Magnelli, B., Wang, T., Aussel, H., Daddi, E., Juneau, S., Shu, X., Sargent, M. T., Buat, V., Faber, S. M., Ferguson, H. C., Giavalisco, M., Koekemoer, A. M., Magdis, G., Morrison, G. E., Papovich, C., Santini, P., and Scott, D. (2015). The Herschel view of the dominant mode of galaxy growth from z = 4 to the present day. *Astronomy & Astrophysics*, 575:A74.

Schwarz, G. (1978). Estimating the Dimension of a Model. *The Annals of Statistics*, 6(2):461 – 464.

Searle, L. (1971). Evidence for Composition Gradients across the Disks of Spiral Galaxies. *The Astrophysical Journal*, 168:327.

Shapley, A. E., Coil, A. L., Ma, C.-P., and Bundy, K. (2005). Chemical Abundances of DEEP2 Star-forming Galaxies at z~1.0-1.5. *The Astrophysical Journal*, 635(2):1006–1021.

Shapley, A. E., Reddy, N. A., Kriek, M., Freeman, W. R., Sanders, R. L., Siana, B., Coil, A. L., Mobasher, B., Shivaei, I., Price, S. H., and de Groot, L. (2015). The MOSDEF Survey: Excitation Properties of z $\sim$ 2.3 Star-forming Galaxies. *The Astrophysical Journal*, 801(2):88.

Shen, S., Mo, H. J., White, S. D. M., Blanton, M. R., Kauffmann, G., Voges, W., Brinkmann, J., and Csabai, I. (2003). The size distribution of galaxies in the Sloan Digital Sky Survey. *Monthly Notices of the Royal Astronomical Society*, 343(3):978–994.

Shivaei, I., Reddy, N. A., Shapley, A. E., Kriek, M., Siana, B., Mobasher, B., Coil, A. L., Freeman, W. R., Sanders, R., Price, S. H., de Groot, L., and Azadi, M. (2015). The MOSDEF Survey: Dissecting the Star Formation Rate versus Stellar Mass Relation Using Hα and Hβ Emission Lines at z $\sim$ 2. *The Astrophysical Journal*, 815(2):98.

Smith, J. A., Tucker, D. L., Kent, S., Richmond, M. W., Fukugita, M., Ichikawa, T., Ichikawa, S.-i., Jorgensen, A. M., Uomoto, A., Gunn, J. E., Hamabe, M., Watanabe, M., Tolea, A., Henden, A., Annis, J., Pier, J. R., McKay, T. A., Brinkmann, J., Chen, B., Holtzman, J., Shimasaku, K., and York, D. G. (2002). The u'g'r'i'z' Standard-Star System. *The Astronomical Journal*, 123(4):2121–2144.

Stasińska, G. (1990). A grid of model HII regions for extragalactic studies. *Astronomy & Astrophysics Supplementary Series*, 83:501.

Stasińska, G. (2005). Biases in abundance derivations for metal-rich nebulae. *Astronomy & Astrophysics*, 434(2):507–520.

Stasińska, G., Cid Fernandes, R., Mateus, A., Sodré, L., and Asari, N. V. (2006). Semi-empirical analysis of Sloan Digital Sky Survey galaxies - III. How to distinguish AGN hosts. *Monthly Notices of the Royal Astronomical Society*, 371(2):972–982.

Steidel, C. C., Rudie, G. C., Strom, A. L., Pettini, M., Reddy, N. A., Shapley, A. E., Trainor, R. F., Erb, D. K., Turner, M. L., Konidaris, N. P., Kulas, K. R., Mace, G., Matthews, K., and McLean, I. S. (2014). Strong Nebular Line Ratios in the Spectra of z ~2-3 Star Forming Galaxies: First Results from KBSS-MOSFIRE. *The Astrophysical Journal*, 795(2):165.

Storey, P. J. and Hummer, D. G. (1995). Recombination line intensities for hydrogenic ions-IV. Total recombination coefficients and machine-readable tables for Z=1 to 8. *Monthly Notices of the Royal Astronomical Society*, 272(1):41–48.

Strom, A., Steidel, C., Rudie, G., and Trainor, R. (2015). KBSS-MOSFIRE: Abundances, star-formation, and physical conditions in star-forming galaxies at z~2-3. In *IAU General Assembly*, volume 29, page 2240662.

Strom, A. L., Steidel, C. C., Rudie, G. C., Trainor, R. F., and Pettini, M. (2018). Measuring the Physical Conditions in High-redshift Star-forming Galaxies: Insights from KBSS-MOSFIRE. *The Astrophysical Journal*, 868(2):117.

Strömgren, B. (1939). The Physical State of Interstellar Hydrogen. *The Astrophysical Journal*, 89:526.

Talbot, Raymond J., J. and Arnett, W. D. (1971). The Evolution of Galaxies. I. Formulation and Mathematical Behavior of the One-Zone Model. *The Astrophysical Journal*, 170:409.

Taylor, A. J., Barger, A. J., and Cowie, L. L. (2022). Metallicities of Five z > 5 Emission-Line Galaxies in SMACS 0723 Revealed by JWST. arXiv:2208.06418 [astro-ph].

Thomas, A. D., Dopita, M. A., Kewley, L. J., Groves, B. A., Sutherland, R. S., Hopkins, A. M., and Blanc, G. A. (2018). Interrogating Seyferts with NebulaBayes: Spatially Probing the Narrow-line Region Radiation Fields and Chemical Abundances. *The Astrophysical Journal*, 856(2):89.

Tremonti, C. A., Heckman, T. M., Kauffmann, G., Brinchmann, J., Charlot, S., White, S. D. M., Seibert, M., Peng, E. W., Schlegel, D. J., Uomoto, A., Fukugita, M., and Brinkmann, J. (2004). The Origin of the Mass-Metallicity Relation: Insights from 53,000 Star-forming Galaxies in the Sloan Digital Sky Survey. *The Astrophysical Journal*, 613(2):898–913.

Veilleux, S. and Osterbrock, D. E. (1987). Spectral Classification of Emission-Line Galaxies. *Astrophysical Journal Supplements*, 63:295.

Xu, Y., Ouchi, M., Rauch, M., Nakajima, K., Harikane, Y., Sugahara, Y., Komiyama, Y., Kusakabe, H., Fujimoto, S., Isobe, Y., Kim, J. H., Ono, Y., and Zahedy, F. S. (2022). EMPRESS. VI. Outflows Investigated in Low-mass Galaxies with $M_* = 10^4\text{-}10^7\ M_\odot$: Weak Feedback in Low-mass Galaxies? *The Astrophysical Journal*, 929(2):134.

York, D. G., Adelman, J., Anderson, John E., J., Anderson, S. F., Annis, J., Bahcall, N. A., Bakken, J. A., Barkhouser, R., Bastian, S., Berman, E., Boroski, W. N., Bracker, S., Briegel, C., Briggs, J. W., Brinkmann, J., many more authors, and SDSS Collaboration (2000). The Sloan Digital Sky Survey: Technical Summary. *The Astronomical Journal*, 120(3):1579–1587.

Zou, H., Sui, J., Saintonge, A., Scholte, D., Moustakas, J., Siudek, M., Dey, A., Juneau, S., Guo, W., Canning, R., Aguilar, J., Ahlen, S., Brooks, D., Claybaugh, T., Dawson, K., de la Macorra, A., Doel, P., Forero-Romero, J. E., Gontcho A Gontcho, S., Honscheid, K., Landriau, M., Le Guillou, L., Manera, M., Meisner, A., Miquel, R., Nie, J., Poppett, C., Rezaie, M., Rossi, G., Sanchez, E., Schubnell, M., Seo, H., Tarlé, G., Zhou, Z., and Zou, S. (2024). A Large Sample of Extremely Metal-poor Galaxies at z ¡ 1 Identified from the DESI Early Data. *The Astrophysical Journal*, 961(2):173.

ANNEXES

Annex A

SED Fitting

This Appendix shows the results of the SED fitting described in Section 3.2. Table A.1 shows the best-fit parameters of the SED of our local analogs modeled as an old stellar population with a late burst of star-formation. Figure A.1 present the plots of the SED of the galaxies highlighting the stellar component showing the Balmer absorption features that were measured to correct the Balmer emission line fluxes as described in Section 3.2.

Table A.1: Physical properties of local analogs estimated from modeling their SED as the SFH of an old stellar population model with a late burst of star-formation.

ID	Age (Gyr)	$\log(M^*/M_\odot)$	$\log(\mathrm{SFR}/M_\odot\mathrm{yr}^{-1})$	A_V (mag)	n_e (cm^{-3})	χ^2_ν
J0021+0052	6.0±3.0	9.06±0.29	1.49±0.07	0.89±0.15	320.82±428.04	0.007
J0023−0948	3.1±2.1	8.49±0.06	0.67±0.04	0.930±0.004	507.99±472.35	3.527
J0136−0037	4.8±3.0	7.79±0.13	0.03±0.05	0.929±0.019	539.32±472.65	1.960
J0240−0828	6.4±3.0	7.87±0.22	0.62±0.11	0.78±0.29	478.82±467.72	0.910
J0252+0114	2.8±1.9	7.27±0.05	-0.55±0.04	0.930±0.002	480.21±470.70	2.775
J0305+0040	2.9±2.0	8.09±0.04	0.27±0.04	0.930±0.001	406.37±457.19	2.813
J0950+0042	6.1±3.0	8.51±0.31	0.99±0.08	0.87±0.19	331.40±432.39	0.019
J1146+0053	5.1±3.0	7.65±0.15	-0.09±0.05	0.93±0.04	495.52±472.08	2.892
J1226+0415	6.3±3.0	8.15±0.31	0.68±0.11	0.79±0.28	348.67±438.91	0.063
J1444+0409	6.1±3.1	6.83±0.30	-0.66±0.16	0.29±0.26	435.93±463.81	2.644
J1448−0110	6.0±3.1	7.89±0.30	0.44±0.09	0.84±0.24	422.99±461.72	0.326
J1624−0022	5.7±3.1	8.27±0.23	0.69±0.09	0.85±0.22	422.85±461.95	0.478
J2101−0555	4.9±3.0	8.99±0.16	1.27±0.04	0.929±0.025	504.23±471.44	0.252
J2119+0052	2.6±1.6	7.76±0.02	-0.07±0.02	0.93000±0.00015	452.39±461.77	10.465
J2212+0006	6.0±3.1	8.34±0.29	0.83±0.06	0.90±0.14	488.93±470.53	0.111
J2215+0002	6.0±3.0	8.06±0.26	0.49±0.04	0.93±0.05	462.52±467.18	0.249
J2225−0011	6.3±3.0	8.18±0.27	0.60±0.06	0.91±0.10	616.55±460.72	0.614
J2337−0010	6.0±3.0	7.86±0.26	0.29±0.04	0.93±0.05	483.75±467.29	0.702
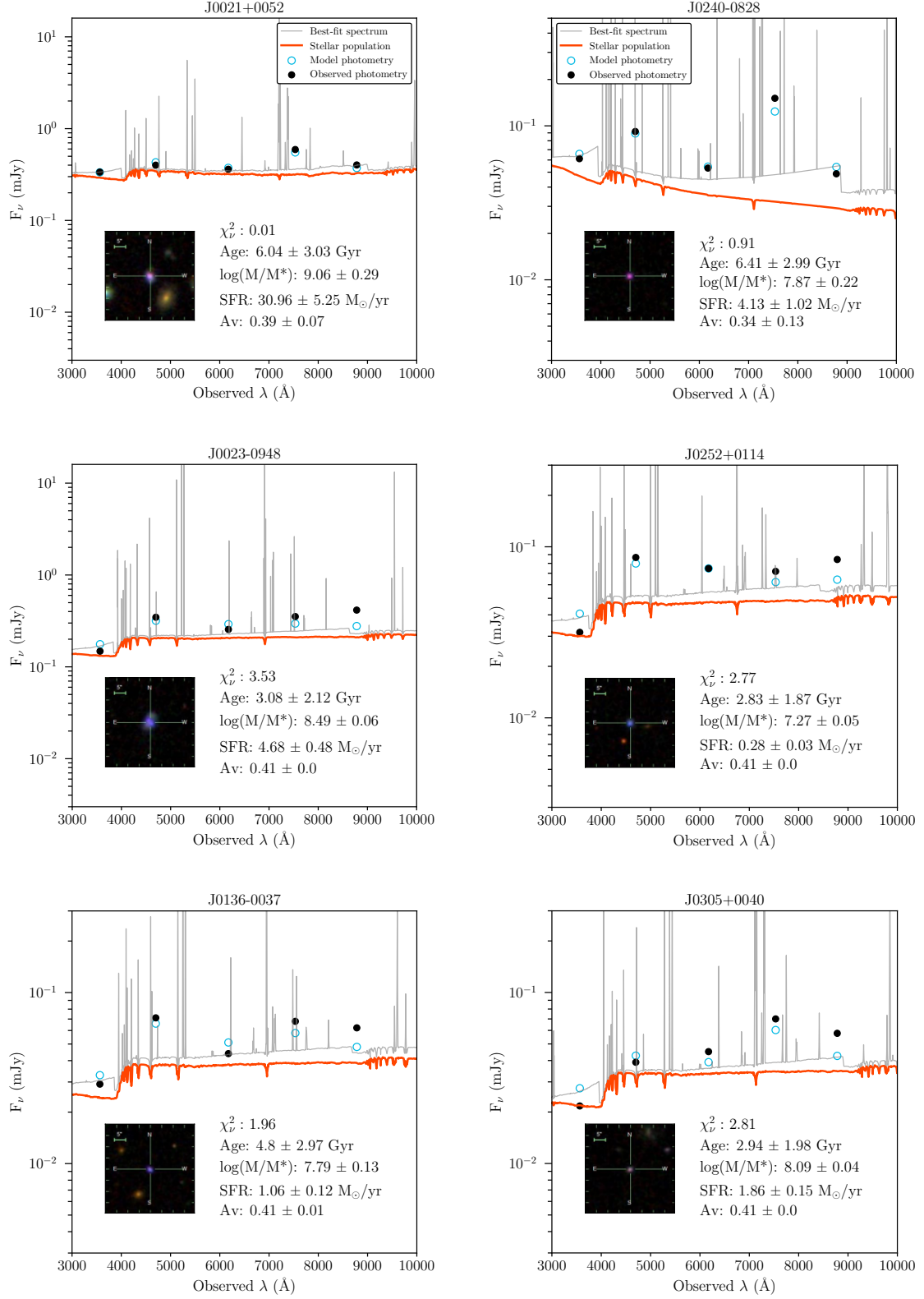
Figure A.1: Best-fit SED of local analogs. Black dots and empty blue circles represent the photometric measurements and models, respectively. The orange line shows the stellar continuum emission, while the gray line is the total spectrum. Each plot contains an SDSS stamp of the source and their estimated SED physical properties.
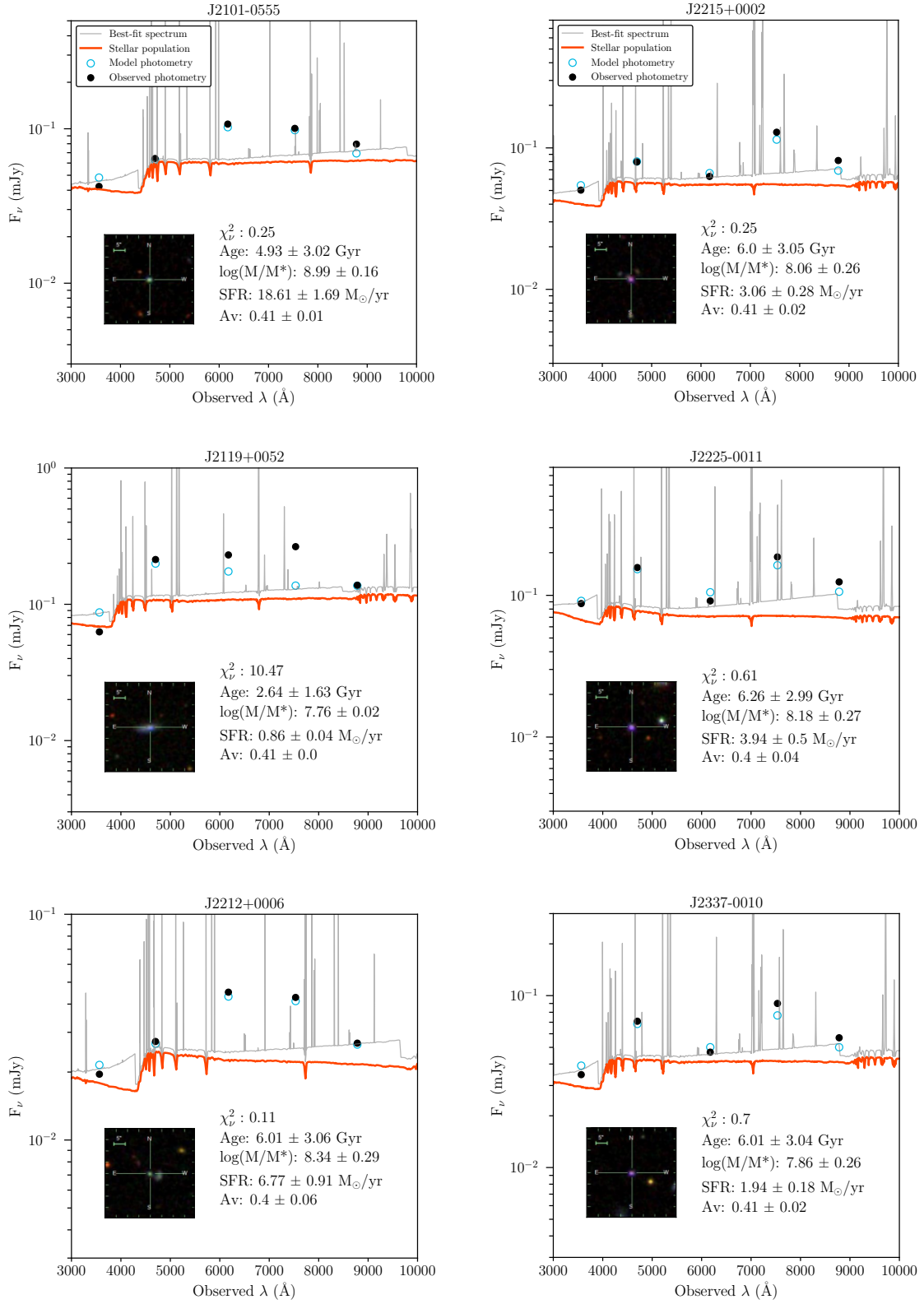
Figure A.1: (*Continued*).

Annex B

Model Testing

Here are the results of the model testing described in Section 3.3. Table B.1 shows the results of the component test with the ΔBIC, the redshift of each galaxy traced by the narrow component, the velocity shift between the components, and their FWHM. Galaxies J0136-0037, J0252+0114, and J1146+0053 have an unresolved narrow component as they give lower widths of the narrow component than the intrinsic broadening.

Table B.1: Model testing parameters and kinematic properties of the local analogs.

ID	ΔBIC$_{1-2}$	ΔBIC$_{2-3}$	z_N	Δv (km/s)	FWHM$_N$ (km/s)	FWHM$_B$ (km/s)
J0021+0052	417.800	30.712	0.099	3.4±1.1	161.3±0.7	421.8±2.5
J0023−0948	61.035	22.557	0.053	-32±7	88.2±0.4	268±14
J0136−0037	248.019	3.756	0.060	7.4±1.4	105.0±0.8*	217±5
J0240−0828	324.039	92.921	0.083	-18.1±1.4	81.4±0.7	274.6±1.5
J0252+0114	282.032	24.843	0.028	4.7±1.1	104.0±0.8*	208±4
J0305+0040	168.026	14.482	0.086	-4.1±1.7	74±4	231±8
J0950+0042	154.733	120.633	0.098	-20.9±1.9	108.3±0.7	273.4±2.1
J1146+0053	195.897	-17.371	0.057	21.1±1.1	63.6±0.9*	77.1±1.2
J1226+0415	210.089	42.792	0.095	2.6±1.9	96.0±0.4	259±6
J1444+0409	125.348	-113.620	0.039	5.2±2.1	44.2±1.7	154±9
J1448−0110	73.346	159.534	0.028	30.6±3.1	94.43±0.26	227.8±1.6
J1624−0022	165.867	9.315	0.032	-13.0±1.9	79.6±1.0	224±7
J2101−0555	133.097	107.401	0.197	-13.1±1.4	12±6	174.2±0.7
J2119+0052	206.156	50.455	0.034	15.6±1.5	65.6±0.9	190±4
J2212+0006	157.852	33.296	0.177	-9.5±2.0	74.1±2.8	219±5
J2215+0002	210.022	110.254	0.078	-7.2±0.9	65.3±0.6	180.5±1.7
J2225−0011	200.965	84.265	0.067	0.2±1.0	80.3±0.9	175.7±1.9
J2337−0010	299.407	64.448	0.072	-10.9±1.1	33.9±1.9	224.1±2.3

* Uncorrected narrow component.

Annex C

Balmer Decrements

Here we present the results of the dust attenuation analysis explained in Section 3.5. The values of the Balmer decrements are shown in Table C.1, including the theoretical ratios of the Case B recombination scheme. Figure C.1 shows the fits to the Balmer decrements for all sources and the results for the color-excess $E(B - V)$.

Table C.1: Balmer decrements for the local analogs under Case B recombination.

ID	Hα/Hβ	Hγ/Hβ	Hδ/Hβ
Case B	2.86	0.468	0.259
J0021+0052	3.313±0.011	0.4481±0.0029	0.2306±0.0027
J0023−0948	3.669±0.014	0.4448±0.0026	0.2347±0.0020
J0136−0037	3.110±0.028	0.470±0.009	0.232±0.008
J0240−0828	3.266±0.017	0.418±0.004	0.2309±0.0032
J0252+0114	2.820±0.029	0.511±0.011	0.267±0.011
J0305+0040	3.49±0.04	0.430±0.013	0.225±0.012
J0950+0042	4.237±0.018	0.4278±0.0030	0.2603±0.0033
J1146+0053	3.55±0.05	0.425±0.008	0.223±0.005
J1226+0415	2.654±0.008	0.4800±0.0017	0.2989±0.0014
J1444+0409	2.834±0.031	0.497±0.006	0.301±0.005
J1448−0110	2.091±0.006	0.4063±0.0016	0.2431±0.0014
J1624−0022	3.066±0.034	0.429±0.012	0.199±0.011
J2101−0555	3.284±0.017	0.533±0.004	0.2631±0.0032
J2119+0052	2.997±0.025	0.332±0.005	0.2039±0.0032
J2212+0006	3.31±0.04	0.438±0.010	0.209±0.010
J2215+0002	3.148±0.013	0.462±0.004	0.2407±0.0029
J2225−0011	3.090±0.016	0.466±0.004	0.2610±0.0035
J2337−0010	3.329±0.017	0.475±0.005	0.235±0.004
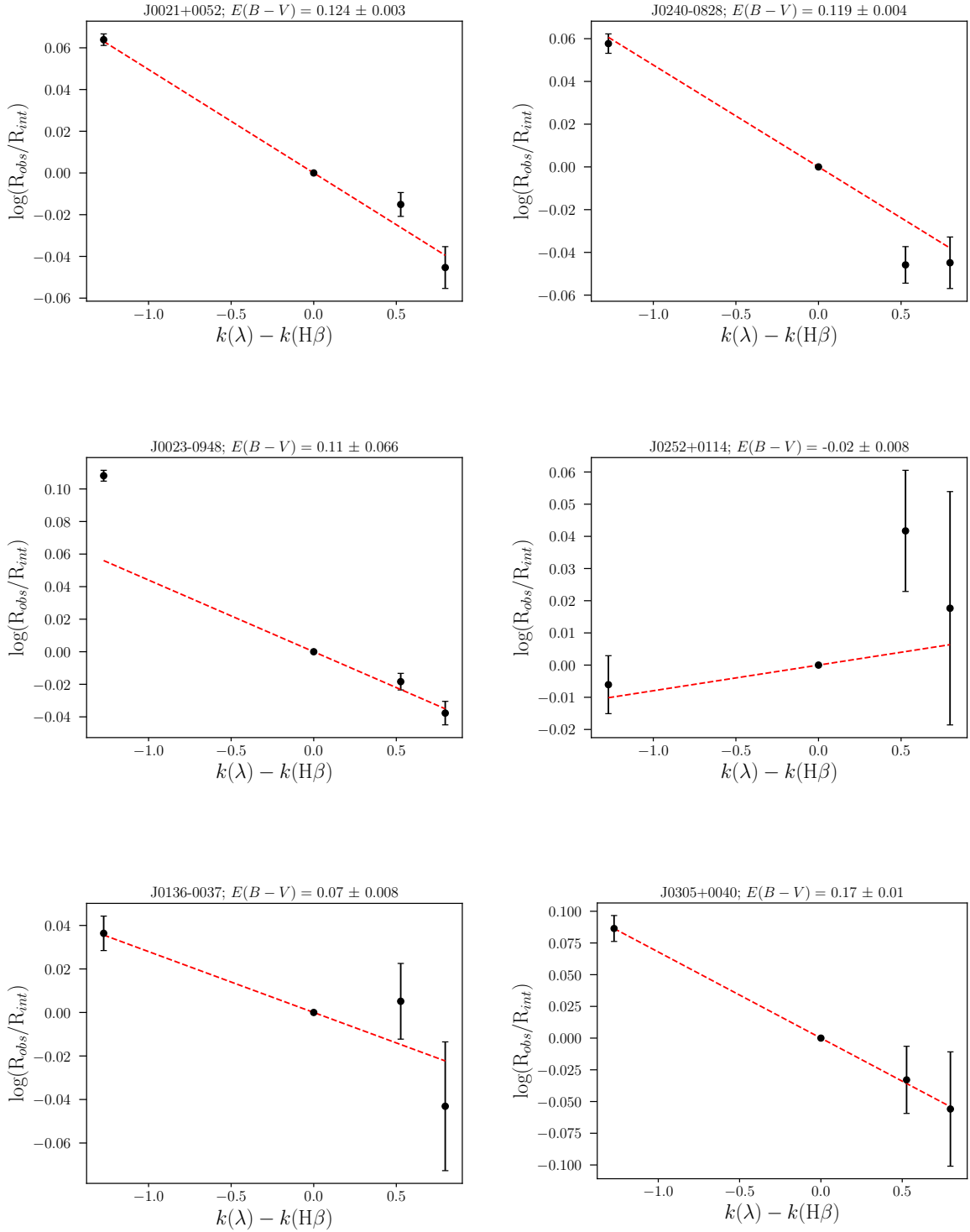
Figure C.1: Fitting to the Balmer decrements. Black dots represent the Balmer decrements with 2σ errorbars. The red-dashed line is the best-fit linear function from which the value of the color-excess is drawn and shown above each panel.
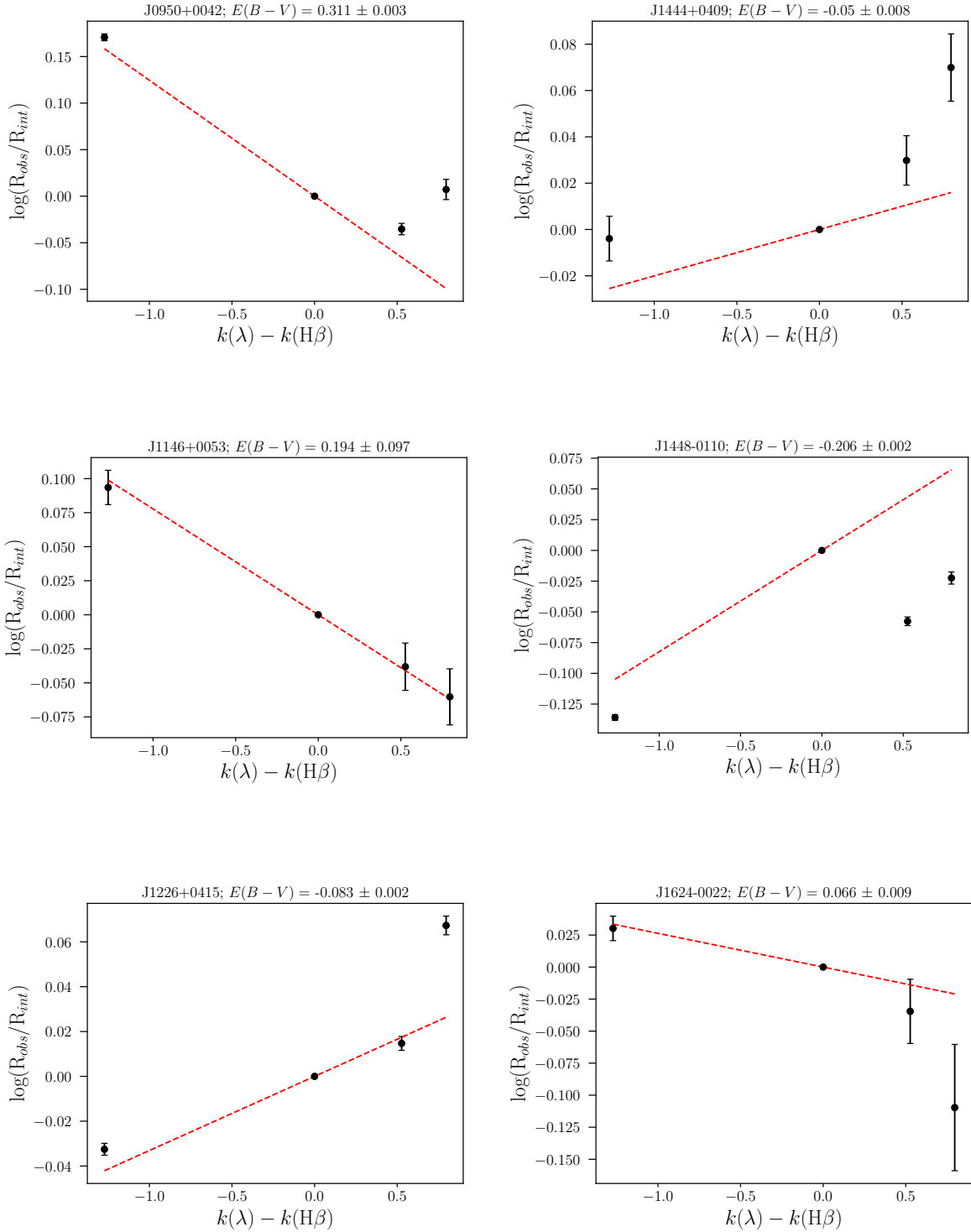
Figure C.1: (*Continued*).
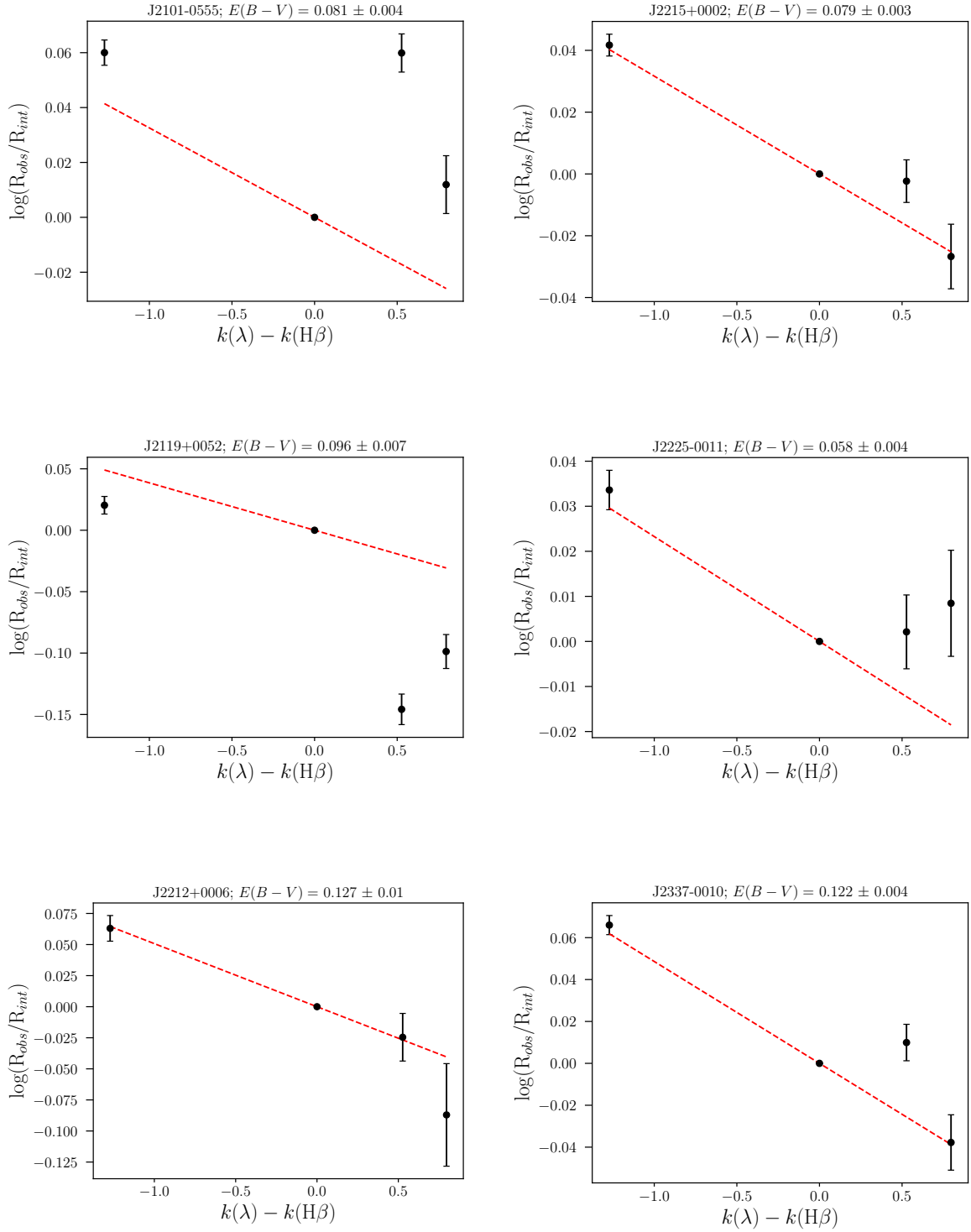
Figure C.1: (*Continued*).

Annex D

Emission Line Measurements

In this appendix we present Table D.1 with the emission line fluxes measured in this study. Each column contains values of $I(\lambda)I(H\beta)$, i.e., the flux of each emission line normalized by the flux of Hβ. The first row has the values of the flux of Hβ in units of 10^{-17} ergs/s/cm^2. Empty spaces are for lines with no detections ($< 3\sigma$) and are not considered.

Table D.1: Measurements of the total flux of the emission lines fitted in this study.

Line	λ_{air} (Å)	J0021+0052	J0023-0948	J0136-0037	J0240-0828	J0252+0114	J0305+0040
Hβ	4861.3500	6291±11	1372.3±3.3	1032±4	3919±11	873±4	1249±6
[O II]λ3726	3726.0320	0.608±0.009	0.716±0.004	0.596±0.010	0.270±0.004	0.470±0.013	0.750±0.018
[O II]λ3729	3728.8150	0.931±0.008	0.983±0.005	0.802±0.012	0.252±0.004	0.714±0.014	0.963±0.020
[Ne III]λ3868	3868.7600	0.3703±0.0022	0.5180±0.0030	0.623±0.007	0.4946±0.0035	0.633±0.010	0.456±0.008
Hδ	4101.7103	0.2526±0.0016	0.2545±0.0020	0.244±0.005	0.2520±0.0022	0.267±0.006	0.255±0.006
Hγ	4340.4720	0.4759±0.0018	0.4692±0.0024	0.486±0.005	0.4424±0.0028	0.511±0.006	0.467±0.006
[O III]λ4363	4363.2090	0.0399±0.0013	0.0746±0.0014	0.124±0.004	0.1351±0.0018	0.130±0.004	0.071±0.005
He Iλ4471	4471.4802	0.0376±0.0011	0.0376±0.0013		0.0383±0.0012		
[Fe III]λ4658	4658.0500	0.0116±0.0007	0.0068±0.0013		0.0059±0.0008		
He IIλ4686	4685.7100	0.0104±0.0007	0.0082±0.0013		0.0257±0.0009		
[Ar IV]λ4740	4740.2000	0.0023±0.0005	0.0073±0.0009		0.4946±0.0035		
[O III]λ4959	4958.9110	1.5523±0.0033	2.006±0.006	2.514±0.013	2.471±0.009	2.358±0.013	1.954±0.011
[O III]λ5007	5006.8430	4.620±0.009	5.567±0.017	7.93±0.04	7.363±0.023	7.02±0.04	5.782±0.029
[N II]λ5755	5754.5900	0.0090±0.0006					
He Iλ5875	5875.6210	0.1203±0.0007	0.1253±0.0009		0.1175±0.0010		
[O I]λ6300	6300.3040	0.0406±0.0005	0.0499±0.0008	0.0253±0.0014	0.0197±0.0005	0.0214±0.0016	0.0324±0.0015
[S III]λ6312	6312.0600	0.0111±0.0004	0.0181±0.0007	0.0142±0.0012	0.0098±0.0006	0.0181±0.0017	0.0149±0.0013
[N II]λ6548	6548.0500	0.0799±0.0006	0.0263±0.0005	0.0094±0.0010	0.0163±0.0006	0.0066±0.0010	0.0305±0.0015
Hα	6562.7900	2.865±0.005	3.225±0.009	2.865±0.014	2.841±0.010	2.820±0.015	2.860±0.015
[N II]λ6584	6583.4500	0.2205±0.0008	0.0828±0.0008	0.0381±0.0012	0.0579±0.0008	0.0353±0.0012	0.1143±0.0022
He Iλ6678	6678.1510	0.0313±0.0005	0.0370±0.0007		0.0300±0.0007		
[S II]λ6716	6716.4400	0.1502±0.0008	0.1763±0.0011	0.1034±0.0020	0.0377±0.0007	0.0915±0.0018	0.1330±0.0024
[S II]λ6730	6730.8150	0.1166±0.0007	0.1307±0.0010	0.0769±0.0019	0.0356±0.0008	0.0704±0.0017	0.1024±0.0025
He Iλ7065	7065.1900	0.0272±0.0004	0.0305±0.0009		0.0534±0.0009		
[Ar III]λ7135	7135.8000	0.0678±0.0006	0.0816±0.0008	0.0629±0.0017	0.0369±0.0007	0.0828±0.0023	0.0790±0.0021
[O II]λ7319	7319.9200	0.0195±0.0006	0.0284±0.0007	0.0191±0.0019	0.0146±0.0008	0.0204±0.0021	0.0158±0.0015
[O II]λ7330	7330.1900	0.0172±0.0006	0.0265±0.0011	0.0159±0.0015	0.0128±0.0008	0.0143±0.0014	0.0146±0.0016
[S III]λ9069	9068.6000	0.1518±0.0023	0.1562±0.0024	0.154±0.008	0.0682±0.0025	0.186±0.011	0.130±0.006
[S III]λ9532	9531.1000	0.411±0.013	0.392±0.004	0.286±0.013	0.177±0.011	0.412±0.009	0.442±0.032

Table D.1: (*Continued*)

Line	λ_{air} (Å)	J0950+0042	J1146+0053	J1226+0415	J1444+0409	J1448-0110	J1624-0022
Hβ	4861.3500	1064.5±2.1	179.7±0.6	1925.7±3.3	800±4	10942±16	213.5±1.2
[O II]λ3726	3726.0320	1.362±0.010	0.442±0.005	0.5838±0.0029	0.324±0.006	0.4367±0.0016	0.458±0.011
[O II]λ3729	3728.8150	1.614±0.010	0.644±0.006	0.7144±0.0030	0.421±0.006	0.5900±0.0019	0.556±0.014
[Ne III]λ3868	3868.7600	0.804±0.004	0.821±0.006	0.7754±0.0032	0.946±0.009	0.5845±0.0017	0.379±0.007
Hδ	4101.7103	0.3271±0.0021	0.2570±0.0022	0.2989±0.0013	0.3007±0.0033	0.2431±0.0009	0.209±0.006
Hγ	4340.4720	0.4975±0.0019	0.4670±0.0030	0.4800±0.0014	0.497±0.004	0.4063±0.0010	0.442±0.007
[O III]λ4363	4363.2090	0.0740±0.0011	0.1743±0.0019	0.1263±0.0007	0.1969±0.0024	0.0829±0.0005	0.061±0.005
He Iλ4471	4471.4802	0.0391±0.0009	0.0344±0.0010	0.0367±0.0004	0.0418±0.0011	0.0306±0.0004	
[Fe III]λ4658	4658.0500	0.0084±0.0007		0.0078±0.0005		0.00542±0.00026	
He IIλ4686	4685.7100	0.0113±0.0007	0.0098±0.0008	0.0125±0.0005	0.0044±0.0006	0.00980±0.00028	
[Ar IV]λ4740	4740.2000	0.0063±0.0006	0.0171±0.0008	0.01281±0.00035	0.0227±0.0008	0.00738±0.00027	
[O III]λ4959	4958.9110	1.774±0.005	2.562±0.011	2.451±0.006	2.739±0.028	2.390±0.004	2.019±0.013
[O III]λ5007	5006.8430	5.359±0.013	7.626±0.026	7.353±0.015	7.98±0.05	6.975±0.011	5.989±0.035
[N II]λ5755	5754.5900			0.00127±0.00027		0.00097±0.00016	
He Iλ5875	5875.6210	0.1190±0.0007	0.1055±0.0011	0.1023±0.0005	0.1250±0.0014	0.08738±0.00031	0.0209±0.0017
[O I]λ6300	6300.3040	0.0318±0.0005	0.0131±0.0005	0.0216±0.0003	0.0139±0.0007	0.01546±0.00016	0.0154±0.0016
[S III]λ6312	6312.0600	0.0129±0.0004	0.0095±0.0005	0.01451±0.00030	0.0106±0.0006	0.01131±0.00015	0.0179±0.0010
[N II]λ6548	6548.0500	0.0361±0.0005	0.0056±0.0005	0.02205±0.00032	0.0084±0.0004	0.01166±0.00012	
Hα	6562.7900	2.942±0.007	2.825±0.011	2.654±0.005	2.834±0.025	2.091±0.004	2.839±0.017
[N II]λ6584	6583.4500	0.1071±0.0008	0.0171±0.0006	0.0617±0.0005	0.0266±0.0006	0.03648±0.00018	0.0642±0.0014
He Iλ6678	6678.1510	0.0286±0.0006	0.0336±0.0008	0.0270±0.0004	0.0312±0.0007	0.02290±0.00017	
[S II]λ6716	6716.4400	0.1044±0.0007	0.0580±0.0009	0.0664±0.0005	0.0407±0.0007	0.06400±0.00024	0.1000±0.0017
[S II]λ6730	6730.8150	0.0791±0.0006	0.0435±0.0009	0.0525±0.0005	0.0328±0.0006	0.04983±0.00021	0.0774±0.0015
He Iλ7065	7065.1900	0.0354±0.0005	0.0266±0.0008	0.0353±0.0004	0.0568±0.0011	0.02082±0.00017	
[Ar III]λ7135	7135.8000	0.0638±0.0006	0.0375±0.0007	0.0553±0.0005	0.0400±0.0009	0.04599±0.00021	0.0751±0.0021
[O II]λ7319	7319.9200	0.0205±0.0006	0.0082±0.0006	0.0142±0.0004	0.0136±0.0016	0.01011±0.00013	0.0142±0.0011
[O II]λ7330	7330.1900	0.0164±0.0006	0.0082±0.0006	0.0123±0.0004	0.0115±0.0009	0.00829±0.00013	0.0121±0.0012
[S III]λ9069	9068.6000			0.0964±0.0015	0.0646±0.0034	0.0908±0.0006	0.115±0.005
[S III]λ9532	9531.1000			0.399±0.016	0.193±0.005	0.2555±0.0011	0.329±0.007

113

Table D.1: (*Continued*)

Line	λ_{air} (Å)	J2101-0555	J2119+0052	J2212+0006	J2215+0002	J2225-0011	J2337-0010
Hβ	4861.3500	1392.1±3.4	1548±7	357.9±2.0	234.2±0.4	354.2±0.7	2105±5
[O II]λ3726	3726.0320	1.267±0.007	0.854±0.009	0.707±0.013	0.5898±0.0034	0.4086±0.0032	0.397±0.005
[O II]λ3729	3728.8150	1.657±0.008	1.150±0.012	0.914±0.014	0.714±0.004	0.5335±0.0035	0.583±0.005
[Ne III]λ3868	3868.7600	0.5293±0.0032	0.405±0.006	0.400±0.008	0.5684±0.0025	0.5514±0.0025	0.6441±0.0035
Hδ	4101.7103	0.2793±0.0021	0.2189±0.0031	0.230±0.006	0.2551±0.0016	0.2724±0.0016	0.2566±0.0022
Hγ	4340.4720	0.5541±0.0027	0.348±0.004	0.466±0.005	0.4796±0.0020	0.4796±0.0020	0.5036±0.0028
[O III]λ4363	4363.2090	0.0515±0.0014	0.0558±0.0020	0.044±0.004	0.0967±0.0010	0.1165±0.0011	0.2018±0.0022
He Iλ4471	4471.4802	0.0383±0.0012	0.0331±0.0014		0.0381±0.0007	0.0360±0.0007	0.0411±0.0012
[Fe III]λ4658	4658.0500	0.0107±0.0009	0.0060±0.0010	0.0143±0.0034	0.0106±0.0006	0.0079±0.0006	0.0074±0.0010
He IIλ4686	4685.7100	0.0089±0.0009	0.0099±0.0011		0.0072±0.0006	0.0121±0.0006	0.0062±0.0010
[Ar IV]λ4740	4740.2000				0.0084±0.0005	0.0105±0.0005	0.0131±0.0009
[O III]λ4959	4958.9110	1.792±0.006	2.021±0.011	1.830±0.013	2.211±0.005	2.138±0.005	2.502±0.007
[O III]λ5007	5006.8430	5.637±0.016	5.472±0.028	5.278±0.031	6.605±0.014	6.360±0.013	7.241±0.019
[N II]λ5755	5754.5900	0.0019±0.0005			0.00285±0.00026		
He Iλ5875	5875.6210	0.1185±0.0010	0.1138±0.0013		0.1157±0.0007	0.1062±0.0006	0.1127±0.0011
[O I]λ6300	6300.3040	0.0595±0.0008	0.0364±0.0006	0.0241±0.0020	0.0328±0.0004	0.02029±0.00035	0.0216±0.0005
[S III]λ6312	6312.0600	0.0121±0.0006	0.0157±0.0007	0.0107±0.0021	0.01641±0.00031	0.01544±0.00033	0.0130±0.0005
[N II]λ6548	6548.0500	0.0343±0.0008	0.0276±0.0006	0.0389±0.0018	0.0393±0.0004	0.01198±0.00030	0.0074±0.0004
Hα	6562.7900	2.985±0.009	2.677±0.013	2.850±0.017	2.869±0.006	2.886±0.007	2.887±0.008
[N II]λ6584	6583.4500	0.1201±0.0011	0.0874±0.0009	0.1424±0.0031	0.1216±0.0006	0.0434±0.0004	0.0318±0.0006
He Iλ6678	6678.1510	0.0336±0.0009	0.0296±0.0007		0.0307±0.0004	0.0275±0.0004	0.0293±0.0007
[S II]λ6716	6716.4400	0.1842±0.0015	0.1773±0.0013	0.1470±0.0029	0.1012±0.0006	0.0845±0.0006	0.0654±0.0009
[S II]λ6730	6730.8150	0.1434±0.0015	0.1281±0.0011	0.119±0.004	0.0756±0.0006	0.0624±0.0005	0.0525±0.0008
He Iλ7065	7065.1900	0.0265±0.0012	0.0221±0.0009		0.0403±0.0006	0.0299±0.0004	0.0477±0.0008
[Ar III]λ7135	7135.8000	0.0662±0.0009	0.0704±0.0010	0.084±0.006	0.0681±0.0005	0.0618±0.0008	0.0523±0.0008
[O II]λ7319	7319.9200	0.0238±0.0007	0.0215±0.0007	0.0186±0.0028	0.0219±0.0005	0.0131±0.0004	0.0178±0.0008
[O II]λ7330	7330.1900	0.0254±0.0019	0.0177±0.0006	0.0109±0.0031	0.0182±0.0004	0.0101±0.0004	0.0152±0.0010
[S III]λ9069	9068.6000		0.203±0.006		0.1315±0.0015	0.1093±0.0013	0.0807±0.0030
[S III]λ9532	9531.1000		0.372±0.004		0.333±0.006	0.269±0.004	0.143±0.006

114

Annex E

Chemical abundances and SELRs

In this appendix we include the tables containing the computed values of metallicity, nitrogen abundance, N/O ratio, helium abundance, and the twelve SELRs listed in Section 3.8.

Table E.1: Measured oxygen, nitrogen, helium abundance, and N/O ratio for individual and metallicity-binned analogs.

ID	$12 + \log(\text{O/H})$	$12 + \log(\text{N/H})$	$\log(\text{N/O})$	He/H
J0021+0052	$8.237_{8.224}^{8.251}$	$7.228_{7.217}^{7.240}$	$-1.014_{-1.025}^{-1.003}$	$0.087_{0.087}^{0.087}$
J0023−0948	$8.081_{8.072}^{8.090}$	$6.748_{6.736}^{6.759}$	$-1.329_{-1.341}^{-1.318}$	$0.096_{0.096}^{0.096}$
J0136−0037	$8.154_{8.132}^{8.179}$	$6.430_{6.404}^{6.457}$	$-1.696_{-1.737}^{-1.658}$	
J0240−0828	$7.978_{7.971}^{7.986}$	$7.020_{6.991}^{7.048}$	$-0.900_{-0.927}^{-0.874}$	$0.083_{0.083}^{0.083}$
J0252+0114	$8.011_{7.990}^{8.034}$	$6.354_{6.324}^{6.386}$	$-1.601_{-1.642}^{-1.562}$	
J0305+0040	$8.317_{8.274}^{8.363}$	$6.820_{6.800}^{6.841}$	$-1.472_{-1.508}^{-1.436}$	
J0950+0042	$8.621_{8.605}^{8.637}$	$6.759_{6.751}^{6.767}$	$-1.860_{-1.868}^{-1.851}$	$0.091_{0.091}^{0.091}$
J1146+0053	$8.190_{8.158}^{8.223}$	$6.030_{6.013}^{6.046}$	$-2.159_{-2.186}^{-2.130}$	$0.083_{0.083}^{0.083}$
J1226+0415	$8.185_{8.173}^{8.196}$	$6.611_{6.607}^{6.615}$	$-1.574_{-1.587}^{-1.561}$	$0.085_{0.085}^{0.085}$
J1444+0409	$7.891_{7.880}^{7.904}$	$6.390_{6.362}^{6.417}$	$-1.484_{-1.522}^{-1.451}$	$0.105_{0.105}^{0.105}$
J1448−0110	$8.316_{8.311}^{8.320}$	$6.542_{6.539}^{6.545}$	$-1.763_{-1.769}^{-1.757}$	$0.066_{0.066}^{0.066}$
J1624−0022	$8.220_{8.185}^{8.257}$	$6.856_{6.817}^{6.897}$	$-1.341_{-1.376}^{-1.307}$	
J2101−0555	$8.521_{8.496}^{8.546}$	$6.795_{6.785}^{6.804}$	$-1.705_{-1.722}^{-1.687}$	$0.088_{0.088}^{0.088}$
J2119+0052	$8.326_{8.310}^{8.341}$	$6.735_{6.723}^{6.747}$	$-1.589_{-1.602}^{-1.576}$	$0.080_{0.080}^{0.080}$
J2212+0006	$8.412_{8.354}^{8.483}$	$7.017_{6.993}^{7.044}$	$-1.367_{-1.432}^{-1.304}$	
J2215+0002	$8.085_{8.080}^{8.091}$	$7.009_{7.001}^{7.017}$	$-1.073_{-1.082}^{-1.065}$	$0.098_{0.098}^{0.098}$
J2225−0011	$7.993_{7.985}^{8.001}$	$6.504_{6.495}^{6.513}$	$-1.472_{-1.486}^{-1.459}$	$0.085_{0.085}^{0.085}$
J2337−0010	$7.814_{7.805}^{7.825}$	$6.251_{6.236}^{6.266}$	$-1.519_{-1.540}^{-1.500}$	$0.092_{0.092}^{0.092}$

Bin	$12 + \log(\text{O/H})$	N$_{sources}$
7.8 - 8.0	$7.919_{7.910}^{7.929}$	4
8.0 - 8.2	$8.118_{8.101}^{8.135}$	6
8.2 - 8.4	$8.283_{8.261}^{8.306}$	3
8.4 - 8.6	$8.518_{8.485}^{8.555}$	5

Table E.2: Estimated SELRs for individual and metallicity-binned analogs.

ID	N2	R2	R3	R23	O3N2	R3N2	N2O2	O3O2	Ne3O2	S2	O3S2	N2S2
J0021+0052	-1.1138±0.0015	0.1872±0.0034	0.6646±0.0008	0.8871±0.0010	1.7784±0.0017	1.3212±0.0015	-0.440±0.006	0.4774±0.0033	-0.619±0.004	-1.0310±0.0016	1.6956±0.0018	-0.0723±0.0021
J0023−0948	-1.591±0.004	0.2303±0.0018	0.7456±0.0013	0.9672±0.0012	2.336±0.004	1.828±0.004	-0.937±0.004	0.5153±0.0016	-0.5160±0.0026	-1.0213±0.0020	1.7669±0.0024	-0.559±0.004
J0136−0037	-1.877±0.013	0.145±0.005	0.8991±0.0020	1.0733±0.0020	2.776±0.014	2.318±0.013	-1.194±0.015	0.754±0.005	-0.351±0.007	-1.201±0.006	2.100±0.007	-0.668±0.015
J0240−0828	-1.691±0.006	-0.282±0.005	0.8671±0.0014	1.0152±0.0013	2.558±0.006	2.104±0.006	-0.668±0.009	1.149±0.005	-0.023±0.006	-1.588±0.007	2.455±0.007	-0.100±0.009
J0252+0114	-1.903±0.014	0.074±0.007	0.8460±0.0023	1.0236±0.0023	2.749±0.014	2.298±0.014	-1.125±0.018	0.773±0.007	-0.272±0.009	-1.241±0.007	2.087±0.007	-0.655±0.015
J0305+0040	-1.398±0.008	0.234±0.007	0.7621±0.0022	0.9754±0.0025	2.160±0.008	1.704±0.008	-0.817±0.013	0.528±0.007	-0.575±0.010	-1.085±0.006	1.847±0.007	-0.304±0.010
J0950+0042	-1.4389±0.0030	0.4737±0.0021	0.7291±0.0010	1.0047±0.0011	2.1680±0.0031	1.6693±0.0030	-1.104±0.004	0.2554±0.0020	-0.5682±0.0029	-1.2048±0.0023	1.9339±0.0025	-0.227±0.004
J1146+0053	-2.219±0.015	0.0361±0.0032	0.8823±0.0015	1.0521±0.0015	3.101±0.015	2.650±0.015	-1.414±0.015	0.8462±0.0030	-0.122±0.004	-1.445±0.005	2.327±0.006	-0.770±0.015
J1226+0415	-1.6337±0.0032	0.1133±0.0015	0.8665±0.0009	1.0454±0.0008	2.5001±0.0033	2.0763±0.0032	-0.976±0.004	0.7531±0.0014	-0.2238±0.0021	-1.3488±0.0024	2.2153±0.0025	-0.280±0.004
J1444+0409	-2.028±0.011	-0.128±0.005	0.9019±0.0025	1.0593±0.0026	2.930±0.011	2.477±0.010	-1.086±0.012	1.030±0.004	0.104±0.006	-1.586±0.006	2.488±0.006	-0.439±0.011
J1448−0110	-1.7583±0.0021	0.0114±0.0012	0.8436±0.0007	1.0167±0.0007	2.6019±0.0022	2.2815±0.0021	-1.0780±0.0026	0.8321±0.0010	-0.2447±0.0015	-1.2642±0.0012	2.1077±0.0014	-0.4880±0.0023
J1624−0022	-1.646±0.009	0.006±0.008	0.7773±0.0026	0.9553±0.0026	2.423±0.010	1.970±0.009	-0.853±0.014	0.771±0.007	-0.428±0.011	-1.204±0.005	1.982±0.006	-0.434±0.010
J2101−0555	-1.395±0.004	0.4659±0.0018	0.7510±0.0012	1.0150±0.0012	2.146±0.004	1.671±0.004	-1.023±0.005	0.2851±0.0016	-0.7422±0.0028	-0.9596±0.0028	1.7107±0.0030	-0.423±0.005
J2119+0052	-1.486±0.004	0.3020±0.0035	0.7381±0.0023	0.9776±0.0021	2.224±0.005	1.797±0.004	-0.990±0.006	0.4361±0.0032	-0.694±0.007	-0.9428±0.0022	1.6809±0.0032	-0.531±0.004
J2212+0006	-1.301±0.009	0.210±0.005	0.7225±0.0026	0.9410±0.0026	2.024±0.009	1.569±0.009	-0.696±0.012	0.513±0.005	-0.608±0.010	-1.030±0.008	1.753±0.008	-0.260±0.012
J2215+0002	-1.3730±0.0022	0.1151±0.0017	0.8198±0.0009	1.0051±0.0009	2.1928±0.0024	1.7350±0.0022	-0.6859±0.0032	0.7048±0.0016	-0.3604±0.0023	-1.2103±0.0021	2.0301±0.0023	-0.1557±0.0029
J2225−0011	-1.823±0.004	-0.0259±0.0023	0.8035±0.0009	0.9750±0.0009	2.627±0.004	2.166±0.004	-0.974±0.005	0.8294±0.0022	-0.2326±0.0028	-1.2934±0.0022	2.0969±0.0024	-0.524±0.005
J2337−0010	-1.958±0.008	-0.0086±0.0031	0.8598±0.0011	1.0303±0.0011	2.818±0.008	2.357±0.008	-1.096±0.010	0.8683±0.0030	-0.182±0.004	-1.389±0.004	2.249±0.005	-0.564±0.009
Bin	N2	R2	R3	R23	O3N2	R3N2	N2O2	O3O2	Ne3O2	S2	O3S2	N2S2
7.8 - 8.0	-1.875±0.004	-0.1112±0.0020	0.8581±0.0008	1.0199±0.0008	2.733±0.004	2.276±0.004	-0.956±0.005	0.9693±0.0019	-0.0836±0.0023	-1.4643±0.0025	2.3224±0.0026	-0.407±0.004
8.0 - 8.2	-1.766±0.004	0.1190±0.0016	0.8432±0.0006	1.0278±0.0006	2.609±0.004	2.151±0.004	-1.055±0.005	0.7243±0.0015	-0.3076±0.0021	-1.2445±0.0019	2.0878±0.0020	-0.515±0.004
8.2 - 8.4	-1.4805±0.0027	0.1480±0.0023	0.7571±0.0008	0.9624±0.0009	2.2376±0.0028	1.8147±0.0027	-0.836±0.004	0.6091±0.0022	-0.5120±0.0034	-1.1054±0.0018	1.8625±0.0020	-0.3659±0.0031
8.4 - 8.6	-1.3785±0.0035	0.3831±0.0020	0.7342±0.0010	0.9869±0.0010	2.113±0.004	1.6466±0.0035	-0.941±0.004	0.3511±0.0018	-0.6393±0.0035	-1.0650±0.0029	1.7992±0.0030	-0.304±0.004